Characterization and Visualization of Reflective Properties of Surfaces

Inauguraldissertation
zur
Erlangung der Würde eines Doktors der Philosophie
vorgelegt der
Philosophisch-Naturwissenschaftlichen Fakultät
der Universität Basel
von

Andrea Bianco
aus Italien

Basel, 2017

Genehmigt von der Philosophisch-Naturwissenschaftlichen Fakultät
auf Antrag von

Prof. Dr. E. Meyer, Dr. Ing. P. Fornaro, and Prof. Dr. M. Poggio.

Basel, den 19.09.2017

Prof. Dr. M. Spiess
The Dean of Faculty

Contents

A Serena e Milo

Chapter 1

Introduction

Images play a vital role in several fields of natural science research, including biology, physics, astrophysics, and computer science. In the natural sciences, images are commonly used in measurements or documentation; such applications include images made with telescopes, optical microscopes, or electron microscopes. In the humanities, images also play an important role in research. In art history, for example, many different types of images, from photos of small objects to three-dimensional reconstructions of buildings, help art historians to develop theories, to discuss them with other scholars, and to document the current state of artworks, e.g. in the process of restoration. This is particularly useful if the object is not easily accessible, in which case a common solution is to work with photographs. These can be a precise tool for capturing the state of an original, e.g. before and after restoration.

Digital photography has simplified the process of visual representation, because digital images can be easily shared and made accessible. Furthermore, digital images are an important part of cultural heritage, and account for a major part of contemporary multimedia output in social, scientific, and economic fields [1].

However, when it comes to more complex kinds of artworks like mosaics, these static and two-dimensional images are not able to reproduce the actual visual impression of the object. Therefore, new technologies and methods are needed to transfer characteristic features of an original into the digital domain. The challenge in the digitization of mosaics, for example, lies in their complex surface properties and reflection behavior. Their specific materiality is a result of countless tesserae that are composed in a setting bed to form the mosaic. Each of these small parts reflects light in a particular way, causing a sparkling effect that cannot be adequately reproduced using normal photographic images. Moreover, ancient or medieval mosaics are usually placed on walls

inside a building, and are meant to interact with aspects of their physical surroundings, including the shape of the walls and the interior lighting.

Similar considerations apply to a variety of other artifacts, such as early prints, books, parchments, and textiles. The visual impression that these objects convey can hardly be reproduced by photographs. Metallic elements and the interplay of different materials give the object a dynamic appearance caused by the localized change of reflectance behavior.

A promising way to solve those limitations is the use of Reflectance Transformation Imaging [2]. RTI is a set of computational photographic methods that capture a subjects surface shape and color, making it possible to interactively re-light the subject from any direction by means of a mathematical model. RTI technique is exhaustively described in chapter 2. First, the reflection of light is captured by multiple photographs illuminated from different positions. Second, a simple mathematical term, typically a second order polynomial, is fitted to the measured reflection for each pixel position. This approach is convenient from several points of view:

- Little hardware is needed to acquire an RTI.
- Stability and reproducibility are easy to guarantee, thanks to a reliable fitting procedure.
- Relatively little knowledge is required to operate the tools.

The major drawback of RTI is the limitation of the applied mathematical model. Within the limitations of the second order polynomial, it is not possible to adequately reproduce many artworks such as mosaics. Other drawbacks are the RTI imaging workflow and the fact that display of RTI requires a particular stand-alone application.

The most promising way to work with RTI renderings is certainly a web-based application, based on standard technologies, without plug-ins or other add-ons. Some basic attempts have been made to integrate an RTI viewer in web applications. Most of those implementations are still in the prototype phase and, most importantly, none of them can properly reproduce objects composed of diffuse and glossy materials.

1.1 Contribution of the author

The author of this thesis contributed with novel outcomes in three different areas:

- Developing a data-driven scientific approach to reproduce surfaces composed of lambertian and glossy materials using the RTI technique with as few parameters as possible. This new approach has been called eRTI (enhanced Reflection transformation imaging).
- Improving the hardware needed to acquire RTI and eRTI, by collaborating with a local Swiss firm to develop a novel solution for image acquisition.
- Using three.js [3], a JavaScript WebGL [4] library, a subset of the common and well-known graphics library OpenGL [5], to render eRTI images in any standard web browser, even on most mobile devices.

The data-driven scientific approach takes into account two different processes:

- Acquiring data and using RTI methodologies to distinguish between glossy and lambertian materials in an arbitrary object.
- Modeling gloss reflectance behavior by referring to art historians' impressions; thus the model must have adjustable parameters to allow the customization according to the needs of the experts.

1.2 Thesis outline

Chapter 2 presents an introduction to the theoretical concepts that have been studied during the course of this work. In this context, special attention has been given to the physical aspects and their linkage with other disciplines, such as color science and computational imaging. The last part of the chapter gives an overview of the state of the art in the field of RTI.

Chapter 3 illustrates the improvements that have been made in the course of this work on the hardware needed to acquire RTIs and eRTIs. It also describes attempts to acquire such images without the use of additional hardware, using only a light source and a camera. This is particularly useful when dealing with objects of considerable size, such as wall paintings or mosaics. Furthermore, the necessary calibration procedures are described as well as the software workflow used.

Chapter 4 describes in detail the eRTI technique and the gloss detection algorithm. Moreover, the rendering algorithm is illustrated and discussed. The effectiveness of the proposed solution is tested on different objects, including the large wall mosaic of the

San Zeno chapel in the Basilica of Saint Praxedes in Rome. Some possible fields of application of the eRTI technology are briefly described Section 4.7.

Chapter 5 presents and discusses the results obtained, starting with a discussion of the results with art-historians. A workflow for the collaboration between scientists and humanities academics is suggested. The outcomes of this discussion are then compared with a numerical analysis.

The thesis ends with chapter 6, where the conclusion and the potential of this work are discussed.

1.3 Publications and presentations

The author of this thesis presented parts of its content at the following conferences:

- Science and Engineering in Arts, Heritage and Archaeology (SEAHA): 2015 (poster), 2016 (presentation)
- IS&T Archiving Conference 2016, (presentation)
- IS&T International Symposium on Electronic Imaging 2017, Material appearance (presentation)
- Digital Humanities 2016, (presentation)

The following articles have been published:

[1] Peter Fornaro, Andrea Bianco, Heidrun Feldmann, Barbara Schellewald, Lothar Schmitt; Neue computerbasierte Verfahren zur Wiedergabe von Kunstwerken; Rundbrief fotografie; 23, 1, 14-23; 2016; Deutsches Dokumentationszentrum fr Kunstgeschichte - Bildarchiv Foto Marburg;

[2] Peter Fornaro, Andrea Bianco; Lukas Rosenthaler; Digital Materiality with Enhanced Reflectance Transformation Imaging; Proceedings of IS&T Archiving Conference (ARCHIVING 2016); 2016; Society for Imaging Science and Technology;

[3] Peter Fornaro, Andrea Bianco, Aeneas Kaiser, Lukas Rosenthaler; Enhanced RTI for gloss reproduction; Electronic Imaging 2017; 8, 66-72; 2017; Society for Imaging Science and Technology;

Furthermore, a patent request for the algorithms described has been issued with the support of Unitectra, the technology transfer organization of the Universities of Basel, Bern and Zurich.

[1] Andrea Bianco, Peter Fornaro; Computer System and Method for Improved Gloss Representation in Digital Images; PCT/EP2016/067045; 18. Juli 2016;

Chapter 2

Theoretical Concepts

2.1 Introduction

In this chapter are introduced some of the more relevant theoretical aspects, that will be used in the following chapters.
It was written with the aim of including all relevant aspects, maintaining some consistency and not excluding important parts, but since the subjects are wide and multidisciplinary, therefore this theoretical introduction is inevitably not complete.
The first part, section 2.2 introduces the subject of color. The reader that should be interested in exploring more in details the concepts here exposed, could have a look at the books in references [6], [7] and [8].
Following, the concept of materiality is introduced in section 2.3. This part introduces the reflection of light with surfaces at a macroscopic level. The techniques used in computer graphics to render surfaces are introduced in section 2.4. To explore more in details the concepts there exposed, the books in reference [9] and [10] are suggested.
The last part, section 2.5 provides an introduction of the research done in the field of Reflectance Transformation Imaging.

2.2 Color

Color is omnipresent in our daily life. Human beings refers to colors for a wide range of daily tasks, for example: deciding if a fruit is unripe, ripe or rotten, or in recognizing edible food only looking at its appearance, avoiding to accidentally eat a slice of soap and preferring instead a slice of *patè*, or deciding what clothes to wear, and many other more.
Color is also part of our language, e.g. in German language the verb *schwarzmalen*

that means “to give a pessimist outlook”, but could be literally translated as “to paint black”; the German expressions *rot sehen* that means “to be angry” but can be literally translated as “to see red” or *Blaues Blut*, a common expression in many languages to identify an outdated social status commonly called nobility.

Despite color is ubiquitous in our world, some confusion about the definition of color is present, because the same term is used in different contexts: optics, colorimetry, psychology, etc. It is useful therefore to give a short historical introduction on how the notion of color was developed.

Color theory principles appeared in the western world literature in the writings of Leone Battista Alberti (c.1435) and the notebooks of Leonardo da Vinci (c.1490). Nevertheless Sir Isaac Newton’s “New Theory about Light and Colors” [11] (1671) can be considered the first attempt to describe the characteristics and proprieties of light and color from a scientific point of view, based on experiments. The famous book by Johann Wolfgang von Goethe, Theory of Colours [12] (German: *Zur Farbenlehre*) (1810) and the debate with Newton’s argument supporters that followed, can be seen as a corroboration of the complexity of color as a topic. Whereas Newton sought to develop a mathematical model to describe light and color, Goethe focused on exploring how color is perceived by the human eye and mind.

The intersection between those worlds, that seemed too far apart, was provided by the Young−Helmholtz theory, developed by Thomas Young [13] (1802) and further expanded by Hermann von Helmholtz [14] (1850). In their work the two physicians and physicists postulates the existence of three types of photoreceptors, which provide humans and primates the vision of color. Physiological evidence of their assumptions was provided only one hundred years later, in 1956 [15].

The current consensus among color scientist is that, in the simplest case, we think of color perception as the interaction of a light source, an object and an observer[16]. There are several physical inputs that stimulate the visual system that results in color. To simplify, they can be divided in two categories: unrelated colors, when light interacts with the observer visual system directly, and related colors, when light is scattered from a surface and then interacts with the observer visual system. More precisely, according to the definition of the International Commission of Illumination (CIE), unrelated color is defined as “colour perceived to belong to an area seen in isolation from other colours”, (CIE 17-1376) [17], while related color is defined as “colour perceived to belong to an area seen in relation to other colour” (CIE 17-1080) [17].

A list of the physical phenomenas that causes color was compiled by Nassau [18], and includes: incandescence, gas excitations, vibrations and rotations, transition metal compounds, transition metal impurities, organic compounds, charge transfer, metals, pure semiconductors, doped or activated semiconductors, color centers, scattering, dispersive refraction, diffraction. In this work was considered manly unrelated colors coming from:

scattering, dispersive refraction, diffraction, and more in general color generated by the passage of light between two material with different refractive index.

2.2.1 Light

Light is the portion of electromagnetic spectrum that is visible by the eye, generally considered in the range of wavelength between 380-780 nm [16] According to the CIE [17] definition, light (CIE 17-659) is "radiation that is considered from the point of view of its ability to excite the human visual system". A quantitative depiction of the colors and the names associated with various wavelengths of light is shown in figure 2.1, although it should be noticed that this is not a precise colorimetry graph. A common practice

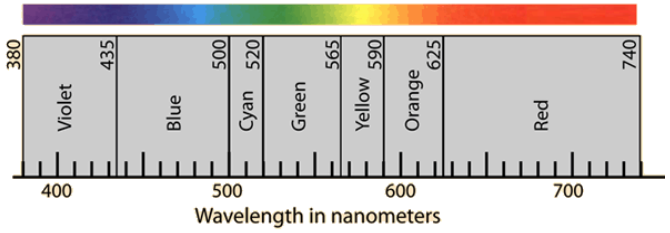

FIGURE 2.1: A qualitative depiction of the colors associated with different wavelengths of light. Source in reference [19]

consists in defining pure colors in terms of the corresponding wavelength of light. This may seem the most obvious (and physically exact) methodology, but it immediately exposes two problems:

- some color are missing: for example purple, brown, pink, and magenta just to mention the most evidently not present;
- combining two different wavelength may result in the same perceived color: this phenomena is called metamerism, and occurs when two different light spectral distribution are confused to be the same color. The cause lies in the process of color detection, that is performed by the eye of the observer, an human being, see section 2.2.2 for a more detailed exposition.

Most of the light sources we encounter, for example the sun, fluorescent lamps, LEDs or hot metals, like the filaments of light bulbs, are not single wavelength sources, but radiates light according to a spectral power distribution (SPD). One very important group of light sources is called white lights. The term "white" refers to the fact that there is no prominent color, or in term of spectral emission, the spectral distribution span over all wavelength. Sunlight is arguably the most famous example. To distinguish between

different sources it is common to use a quantity called correlated color temperature, T_C, measured in Kelvin K. This is the color temperature of the blackbody that they most nearly resemble visually, it is calculated numerically according to the method described in reference [20] that has been later expanded and systematized, see for example references [21] or [22].

A black body is a theoretical idealized object, described as something that absorbs all incident radiation. It is commonly pictured as a cavity or empty box in which electromagnetic radiation is bouncing back and forth between walls. The cavity has a little hole that emit according to Planck's law[23]:

$$B_\lambda(\lambda, T) = \frac{2hc^2}{\lambda^5} \frac{1}{e^{\frac{hc}{\lambda k_B T}} - 1}. \tag{2.1}$$

where k_B the Boltzmann constant, h the Planck constant, and c the speed of light in the medium. B_λ describes the spectral radiance unit wavelength λ at a given temperature T. The SI units of B_λ are $W \cdot sr^{-1} \cdot m^{-3}$. The SPD of a black body depends only on its temperature.

The SPD of a ideal black body is presented in figure 2.2, different curves represent the SPD at different temperatures. As a comparison, the interval of visible light is superimposed.

CIE [17] defines two light sources for use in colorimetry, called illuminants. CIE stan-

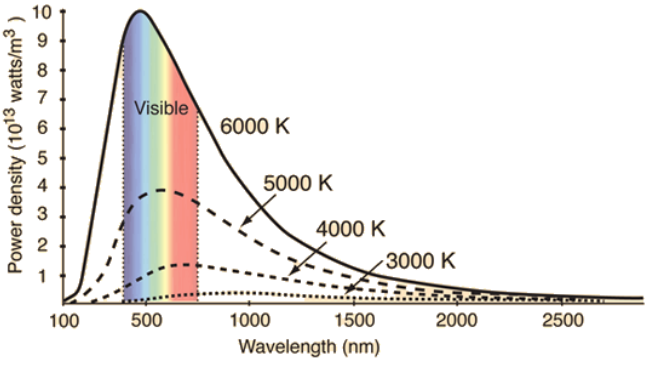

FIGURE 2.2: Intensity of the black body emission as a function of temperature and wavelength, the interval of visible light is shown as a comparison. Source in reference [19]

dard illuminants are used in colorimetry to compute colours under specified conditions of illumination. These light sources are:

- CIE standard illuminant A (CIE A): represent typical, domestic, tungsten-filament lighting. The CIE recommends its use as a reference in all the situation involving the use of incandescent lighting [17].

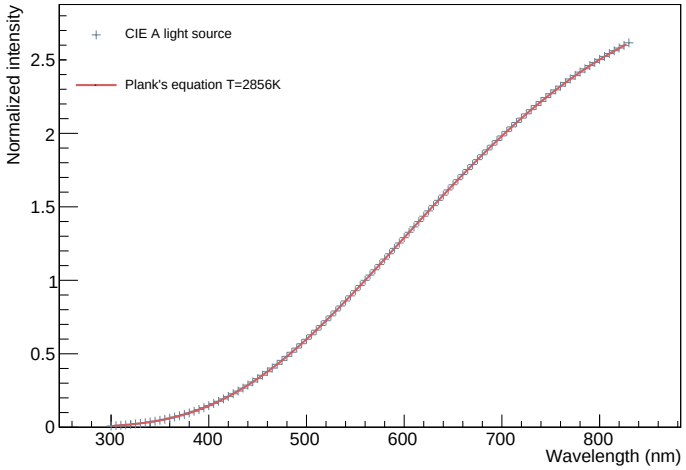

(A) Comparison between black body radiation curve (2856K) and CIE Illuminant A.

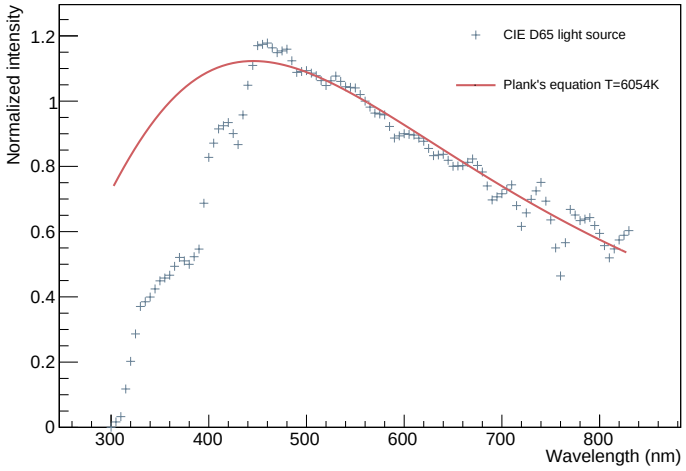

(B) Comparison between black body radiation curve (6504K) and CIE Illuminant D65.

FIGURE 2.3

- CIE standard illuminant D65 (CIE D65): represent average daylight. Variations in the relative spectral power distribution of daylight occur as a function of season, time of day, and geographic location, particularly in the ultraviolet spectral region. However, CIE standard illuminant D65 represent an averaged information to be used as a standard [17].

Figure 2.3a shows a comparison between the SPD of the CIE A and the equation 2.1 for T = 2856K, both normalized at 530nm. Figure 2.3b shows a comparison between the SPD of the CIE D65 and the equation 2.1 for T = 6504K, both normalized at 530nm. It is visually clear why it is convenient to use Plank's law to characterize different white light sources.

Other light sources could have a different and more complex SPD, for example with prominent spikes in some region. In this case the concept of color temperature as exposed is not holding anymore but it is anyway used for practical reason. Commonly LEDs light come with a color temperature specified. In this case, the SPD has prominent spikes, but the T_C refers to SPD of the closest blackbody radiator.

2.2.2 Human perception and physical measurements

A deeper understanding of color cannot be achieved without some knowledge about the detector system. In the human body the eye serves this purpose and detects electromagnetic radiation in the range between 380-780 nm [16]. Although it has been reported that in particular conditions humans are able to see also at a lower limit of 310 nm [24] and at an upper limit of 1050 nm [25]. The information acquired by eyes is then processed by our brain. It goes well beyond the scope of this thesis to provide a complete description of this complex and not yet completely understood process. For a first understanding, it is not crucial to know in detail how the visual system works: it will be sufficient the description of few basic principles.
Figure 2.4 shows a schematic representation of the human eye and its main components. It can be divided in three main parts [26]:

- the external layer, formed by the sclera and cornea;
- the intermediate layer, divided into two parts: anterior (iris and ciliary body) and posterior (choroid).
- the internal layer, or the sensory part of the eye, the retina, the center of the retina has a small indentation known as the fovea

Light enters our eyes through the pupil, and it is projected on the back of the eyeball, the retina. Here the light is absorbed by light receptors. The quality of the retinal image depends on the absorption, scattering and focusing proprieties of the cornea, lens and fluids filling the eyeball [16] [26]. In the retina there are two class of receptors, rods and cones. The rods are more numerous and are more sensitive than the cones. Source in reference [26]. However, they are not sensitive to color. There exist three different types of cones, characterized by their spectral sensitivity, providing the eye's color sensitivity. Cones are much more concentrated in a region around the fovea, called macula. The fovea is a 0.3 mm diameter area with very thin, densely packed cones and no rods. While the visual acuity or visual resolution is much better with the cones, the rods are better motion sensors [27].
Cones can be divided into long-, middle- and short-wavelength-sensitive (L, M and S),

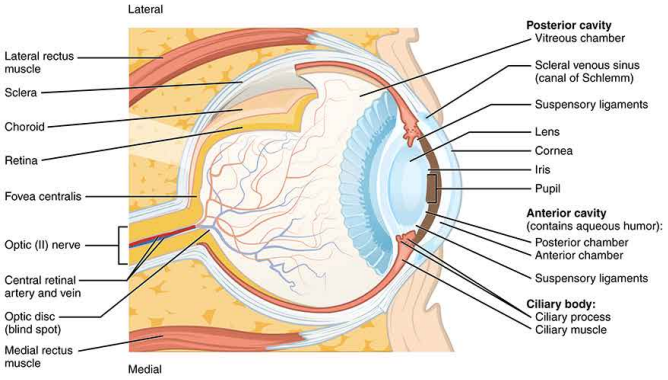

FIGURE 2.4: Schematic representation of an human eye [26].

according to the relative spectral positions of their peak sensitivities or "red" cones, approximately 64% of the total, "green" cones, approximately 32%, and "blue" cones, approximately 2%, the actual ratio is current topic of debate [27]. Figure 2.5 shows the spectral sensitivity of rods and cones. These sensitivities are measured in front of the eye, instead of isolated photo-receptors. Cone isolation can be simplified by the use of special observers, who lack one or more of the three cone types. A traditional method to estimate the M- and L-cone spectral sensitivities consists in using redgreen dichromats: protanopes, who are missing L-cone function, and deuteranopes, who are missing M-cone function [28].

When two stimuli produce the same cone signal, our brain interpret this information

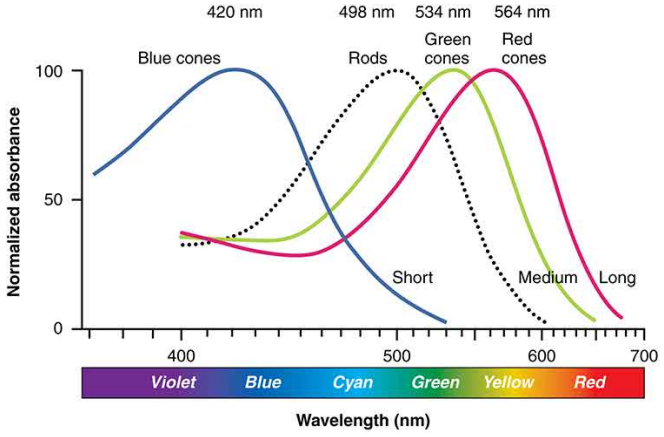

FIGURE 2.5: Spectral sensitivity of human eye light receptors. Source in reference [26]

as matching colors. Color matching can be calculated knowing the cones's spectral sensitivities and the two incoming spectra. The cones integrate the incident light at all wavelengths. Each "acquisition" leads to three values, one for each kind of cones, resulting in what is called trichromacy. This information is then processed by our brain, although there is no consensus on how the brain interpret trichromacy informations. Opponent color theory [6] is a theory on how the human visual system interprets information about color by processing signals from cones and rods in an antagonistic manner.

The basic assumption relies on the idea that is more efficient for the visual system to record differences between the responses of cones, rather than each type of cone's individual response. It follows that there are three opponent channels: red versus green, blue versus yellow, and black versus white (the last type is achromatic and detects light-dark variation, or luminance) [6]. A further attempt to describe how brain process thricomacy information is zones color theory [6]. Starting from opponent colory theory principles, it assumes that our brain process zones or blobs of cones and rods together.
Trichromacy leads to an important features of visual systems: metamerism [29]. It is possible to have different stimuli to produce the same color impression, this fundamental propriety is widely used in our world: cathode-ray tube (CRT) displays produce a wide range of color even if they are made of leds of only three colors.
Taking into account all the considerations explained above, it can be understood why recognizing and specifying a color is a complex task. To overcome those difficulties, the International Commission on Illumination (usually abbreviated CIE) developed a series of experiments: the color matching experiments [8]. Their roots can be found in early Newton's experiments, but the first standardized tests can be considered the one carried out by CIE in 1931 [30] [31]. A schematic representation of the basic principle behind

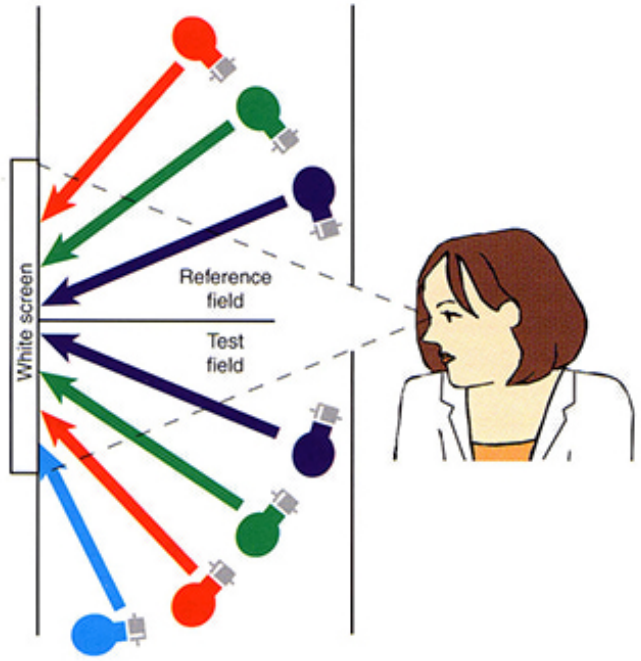

FIGURE 2.6: Schematic representational of the color matching experiment. On the test field the reference light is projected. On the reference field, the sum of three primary lights is projected. A certain amount of the primary lights can be also added to the test field. Source in reference [7]

this class of experiments is presented in Figure 2.6. On a white screen are displayed the outcome of two light projection. On the test field the reference light is projected,

displaying the color that is intended to be matched. On the reference field, the sum of three primary lights is projected. The intensity of the primary lights is adjustable. Furthermore there is the possibility to add certain amount of the primary lights to the test field. Those added values will then count as negative values. The test lights have the same spectra of the primary lights in the test field, but their intensity can be independently changed. The test field and the reference field are separated, so no overlapping is possible. The observer is asked to observe at the same time the two fields and to adjust the primary lights in the test field and in the reference field, until the colors perceived in the two fields match. For the experiment to be as accurate as possible, it is important to select the primary lights to be monochromatic. In addition it is important to maximize the independent stimulation of the eye's cone responses. Primaries of 400 nm (blue) and 700 nm (red) are selected for this reason. Concerning the middle wavelength, it is impossible to select a completely independent wavelength - see Figure 2.5 - since M and S cones have a huge overlap in wavelength response. A compromise is found in selecting 520 nm as a green light. Given the distribution of cones in the eye, previously explained, the perceived color depend also on the observer's field of view. To eliminate this variable, the CIE defined a color-mapping function called the standard observer, to represent an average human's chromatic response. The angle is chosen within a 2 deg arc of the fovea. Thus the CIE 1931 Standard Observer function is also known as the CIE 1931 2 deg Standard Observer [17]. A more modern but less-used alternative is the CIE 1964 10 deg Standard Observer [17] that takes into account a 10 deg observer's field of view.

The numeric response - the intensity of each primary light - of the observer to the color matching experiment is described by the Color Matching Functions (CMF). Figure 2.7

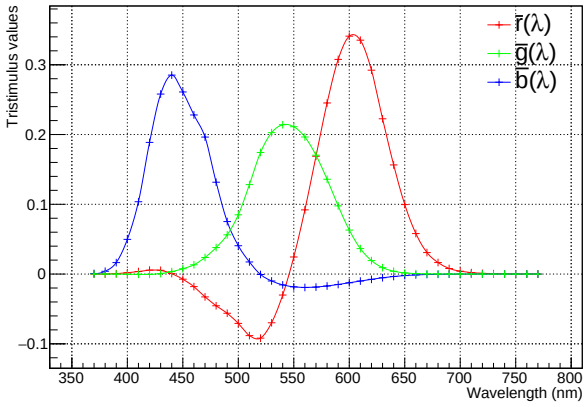

FIGURE 2.7: Color matching functions for the CIE standard observer (1931) modified in 1951 [32]

shows the CMF for the CIE 1931 standard observer, a sum of the results independently

obtained in the 1920s, W. David Wright [31] and John Guild [30] from a series of experiments on human sight, Wright carried out experiments with ten observers. Guild conducted his experiments with seven observers. Their results were later corrected and expanded [32], [6], [16]. The curves are normalized to have constant area beneath them. This area is fixed by specifying that:

$$\int_0^\infty \overline{r}(\lambda)\, d\lambda = \int_0^\infty \overline{g}(\lambda)\, d\lambda = \int_0^\infty \overline{b}(\lambda)\, d\lambda \tag{2.2}$$

Given those normalized CMF, the RGB values for a generic spectrum $S(\lambda)$ are given by:

$$R = \int_0^\infty S(\lambda)\, \overline{r}(\lambda)\, d\lambda, \tag{2.3}$$

$$G = \int_0^\infty S(\lambda)\, \overline{g}(\lambda)\, d\lambda, \tag{2.4}$$

$$B = \int_0^\infty S(\lambda)\, \overline{b}(\lambda)\, d\lambda. \tag{2.5}$$

2.2.3 Color spaces

The color space defined by the coordinates RGB resulting from equations 2.2 has the inconvenience of having negative color coordinates. To solve this problem, in 1931, CIE proposed a set of coordinates with the following important proprieties:

- the CMF should be everywhere greater than or equal to zero. This was important at the time, since all the computation where performed by hand, and having only positive values was a great simplification.
- It was required for the constant energy white point to meet the condition $x = y = z = 1/3$.
- From the first two condition, the gamut (the complete subset) of all colors will lie inside the triangle $[1, 0], [0, 0], [0, 1]$. It was required that the space defined in the triangle was filled completely, with no empty spaces.

From this conditions, the XYZ 1931 CIE color space was defined as [6]:

$$\begin{bmatrix} X \\ Y \\ Z \end{bmatrix} = \frac{1}{0.176(97)} \begin{bmatrix} 0.490(00) & 0.310(00) & 0.200(00) \\ 0.176(97) & 0.812(40) & 0.010(630) \\ 0.000(0) & 0.010(00) & 0.990(00) \end{bmatrix} \begin{bmatrix} R \\ G \\ B \end{bmatrix} \tag{2.6}$$

Figure 2.8 shows the color matching functions $\bar{x}, \bar{y}, \bar{z}$ as a function of the wavelength. A

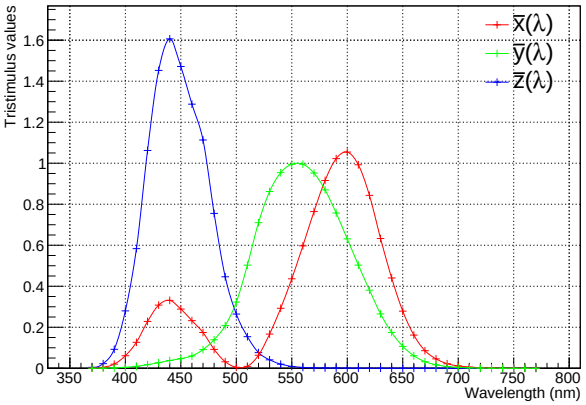

FIGURE 2.8: Color matching functions for the CIE standard observer (1931) modified in 1951 [32]

comparison with Figure 2.7 shows the have no negative values are not present anymore. Using the color matching function is possible to calculate the XYZ coordinates for a generic spectrum $S(\lambda)$, similarly to Equations 2.5:

$$X = \int_{380}^{780} S(\lambda)\,\overline{x}(\lambda)\,d\lambda, \tag{2.7}$$

$$Y = \int_{380}^{780} S(\lambda)\,\overline{y}(\lambda)\,d\lambda, \tag{2.8}$$

$$Z = \int_{380}^{780} S(\lambda)\,\overline{z}(\lambda)\,d\lambda. \tag{2.9}$$

The CIE XYZ coordinates were designed so that the Y parameter is a measure of the luminance of a color. The chromaticity of a color can be specified by two derived parameters - x and y - calculated as:

$$x = \frac{X}{X+Y+Z} \tag{2.10}$$

$$y = \frac{Y}{X+Y+Z} \tag{2.11}$$

$$z = \frac{Z}{X+Y+Z} = 1-x-y. \tag{2.12}$$

Therefore to obtain the chromaticity coordinates for a given colored object the following steps are required:

- Measuring, sampling, the SPD as a function of the wavelength.
- Convolving the SPD with each of the three color matching function.
- Integrate over the visible spectrum to get the three tristimulus values X,Y,Z.

The CIE XYZ color space has its disadvantages that have been pointed out by the MacAdam experiment [33]. He proposed a color matching experiment with 25 points and it was found that the matches by a single observer fell into an ellipse on the CIE 1931 chromaticity diagram. The match was not expected to be perfect, since the human eye has limited accuracy but the irregularity of the orientation of the ellipsis and their size was not convenient. A number of attempts have been made to define a color space which is not as distorted, in terms of color difference, as the CIE XYZ space. For practical purposes, a wide variety of other color spaces has been created, each with different proprieties and features. Probably the most notable are CIELAB, CIELUV, sRGB, AdobeRGB, although ECI RGB and many other are used.
CIE L*a*b* (CIELAB) and CIELUV are color spaces specified by the CIE [17]. CIELAB was created from the opposite color theory as a device-independet model to be used as a reference. It describes all the colors visible to the human eye [8]. The CIE 1976 (L*, u*, v*) color space, commonly known by its abbreviation CIELUV, is a simple-to-compute transformation of the 1931 CIE XYZ color space which attempts to achieve perceptual uniformity [8].
sRGB and AdobeRGB are color spaces developed by private companies: sRGB was proposed by Hewlett-Packard and Microsoft and it is a International Standard [34], while AdobeRGB, as the name suggests, by Adobe Systems, Inc [35]. Both these color spaces uses a technique called Gamma correction. Gamma correction is a non linear operation used to convert tristimulus values. In its simplest form, it is defined by a power-law with expression of the form:

$$V_{\text{out}} = A{V_{\text{in}}}^{\gamma} \tag{2.13}$$

where V_{out} and V_{in} are the output and input values, such as R,G or B, or X,Y,or Z. A and γ are constants.
The transformation from CIEXYZ to sRGB can be divided in two steps. The first step is a linear transformation, described by 2.14:

$$\begin{bmatrix} R_{\text{l}} \\ G_{\text{l}} \\ B_{\text{l}} \end{bmatrix} = \begin{bmatrix} 3.2406 & -1.5372 & -0.4986 \\ -0.9689 & 1.8758 & 0.0415 \\ 0.0557 & -0.2040 & 1.0570 \end{bmatrix} \begin{bmatrix} X \\ Y \\ Z \end{bmatrix} \tag{2.14}$$

where X, Y, Z are the CIE XYZ coordinates and $R_{\text{l}}, G_{\text{l}}, B_{\text{l}}$ are the linear RGB coordinates. The second step involves a gamma correction, described by equation 2.15. The result is a non-linear but reversible transformation.

$$R_{\text{l}}, G_{\text{l}}, B_{\text{l}} = \begin{cases} 12.92C_{\text{linear}}, & R_{\text{l}}, G_{\text{l}}, B_{\text{l}} \leq 0.0031308 \\ (1+a)(R_{\text{l}}, G_{\text{l}}, B_{\text{l}})^{1/2.4} - a, & R_{\text{l}}, G_{\text{l}}, B_{\text{l}} > 0.0031308 \end{cases} \tag{2.15}$$

where $a = 0.055$. After trying different possibilities, sRGB was choosen as the color space used in this work, since it is the most widely adopted color profile for output devices, and the de-facto standard on the web. sRGB does not define primaries wavelengths in its specifications, but the XYZ coordinates of the Red, Green and Blue, see reference [34].

$$\text{Red} : X = 0.64, Y = 0.33, Z = 0.03; \tag{2.16}$$

$$\text{Green} : X = 0.30, Y = 0.60, Z = 0.10; \tag{2.17}$$

$$\text{Blue} : X = 0.15, Y = 0.06, Z = 0.79. \tag{2.18}$$

$$\tag{2.19}$$

2.3 Materiality

Researchers, engineers and computer scientist have long pursued techniques for modeling material appearance or materiality. Similarly, creating the most realistic replica of an object has been the scope of several artistic forms, such as painting and sculptures, and more recently photography and computer graphics. This process has been an interplay between arts and sciences, since materiality is the combination of several different factors: the shape of an object, its geometry, the reflection proprieties, the light under witch it is illuminated, just to mention some of them. A deep understanding of how color works is fundamental, but it is not enough to create a realistic visual impression of an object. Thanks to physicist and computer scientists, in the last 30 years, we assisted to an increasing interest of data-driven methods and models, see reference [10] and [9] as examples. As the name indicates, data-driven methods relay on measurements. A theoretical model is needed to interpret significant measurements as well as a measuring instrument. Radiance and the reflectance distribution function are the two minimal quantity needed to describe how light is reflected by an object.
The radiance, usually noted with the letter L, in a particular direction identified by the solid angle Θ is defined as [36]:

$$L(\Theta) = \frac{\partial^2 \phi(\Theta)}{cos(\theta)\partial A \partial \Theta} \tag{2.20}$$

where $\phi(\Theta)$ is the radiant energy reflected, transmitted or received, per unit time (the SI unit W), in the solid angle Θ, $A\cos(\theta)$ is the projected area. The flux per unit surface area can be calculated as $E = \partial\phi/\partial A$
In the common case where the radiance depends on the wavelength, and on the point on a surface, described by two dimensional spatial coordinates $\mathbf{x} = (x, y)$, equation 2.20 becomes [36]:

$$L(\lambda, \mathbf{x}, \Theta) = \frac{\partial^3 \phi(\lambda, \mathbf{x}, \Theta)}{cos(\theta)\partial A \partial \Theta \partial \lambda} \tag{2.21}$$

In most practical cases it is useful to distinguish between the radiance of incident or leaving light on a surface. Following the prescriptions of the Global Illumination Compendium [37] the following notation is introduced:

- $L(\lambda, \mathbf{x} \leftarrow \Theta)$ is arriving at point $\mathbf{x}$ from direction Θ;
- $L(\lambda, \mathbf{x} \rightarrow \Theta)$ is leaving point $\mathbf{x}$ in direction Θ.

In this work only the reflected light is taken into account, but in a more generic model, light could also be transmitted in the material. In that case, to avoid confusion L_r represent the reflected component and a further function, usually called L_t, is used.

2.3.1 Reflection

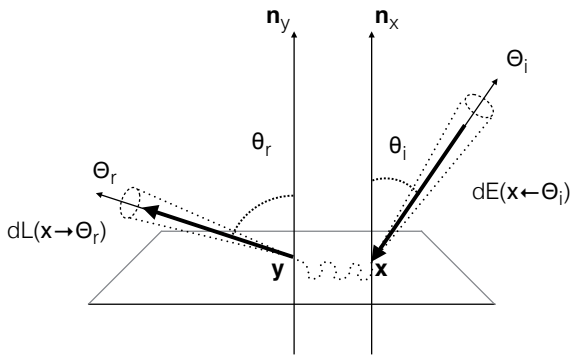

FIGURE 2.9: Schematic representation of a generic case of reflection. The light is coming from a direction Θ_i on the surface at the point $\mathbf{x}$ and leaving the surface at a point $\mathbf{y}$ with direction Θ_r.

Figure 2.9 schematically represents a generic case for reflection. The light is coming from a direction Θ_i on the surface at the point $\mathbf{x}$ and it is leaving the surface at a point $\mathbf{y}$ with direction Θ_r. Therefore a model that describes this generic situation should take into account, if we consider also time, 12 coordinates: $(\mathbf{x}, \lambda, \Theta_i, t)_{in} \rightarrow (\mathbf{y}, \lambda, \Theta_o, t)_{out}$. However, a 12D function is highly unpractical to measure, store and process. For this reason, a wide taxonomy of reflectance functions, derived as reduction of the 12D general case, as been in use since 1965 [38] [39], [9]. The most commonly used terms are organized in figure 2.10. To lower the number of dimensions the first assumption is exclude the dependecy on for wavelength and time dependency. This assumption excludes all materials that change color under different viewing or illuminating condition and fluorescent material. This remark is important when considering infrared (IR) and ultraviolet (UV) photography, see section 2.6. The function obtained is then called Bidirectional Scattering-Surface Distribution Function (BSSRDF) and is a 8D function. It is general enough to describe material with sub-surface scattering proprieties.

The second assumption is that the light exits from the same point it enters, see figure 2.11 referring to the case where $\mathbf{x} = \mathbf{Y}$. This constrain describes a wide class of materials, called opaque materials, where no sub-surface scattering happens. The function describing this class of materials is called Bidirectional Texture Function (BTF) or Spatially Varying Bidirectional Reflectance Distribution Function (SVBRTF) and it is a 6D function. Another possibility, is to ask for dependence only on the relative surface position of incoming light. Such a condition, described by the Bidirectional Subsurface Scattering Distribution Function (BSSDF), is used to describe materials where light transport within plays a significant role. Notable examples are milk or human skin [9].

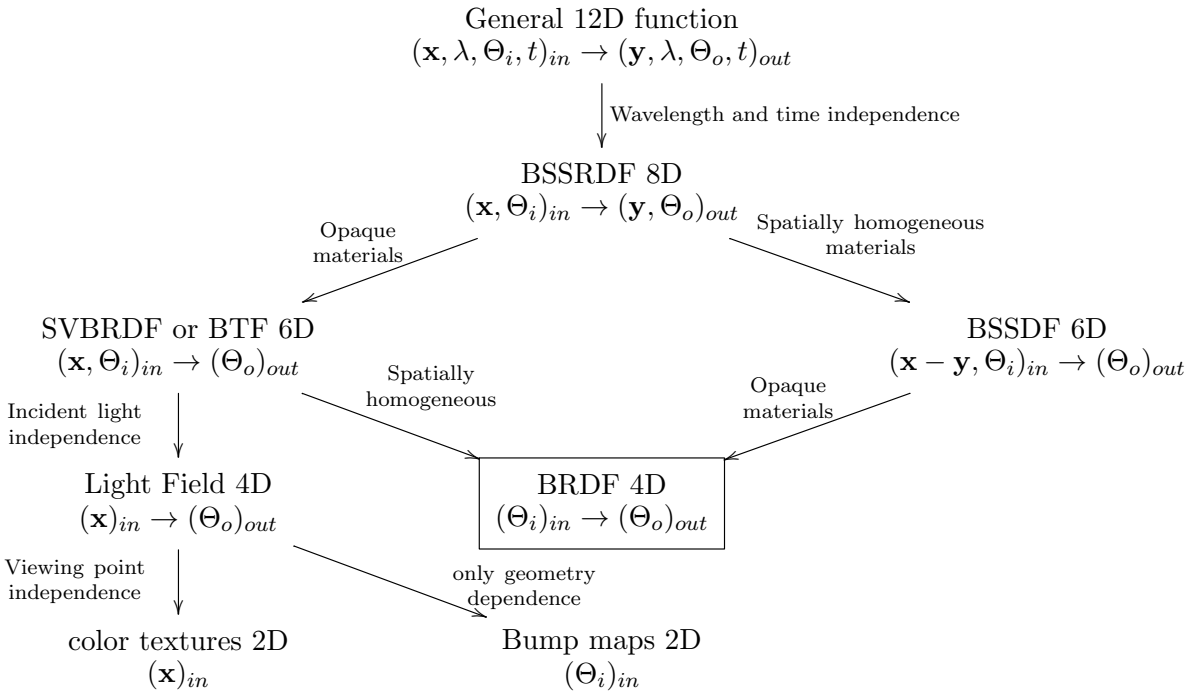

(2.22)

FIGURE 2.10: Taxonomy of reflectance distribution functions

Further assumptions consist in asking for spacial uniformity on the material or indepen-

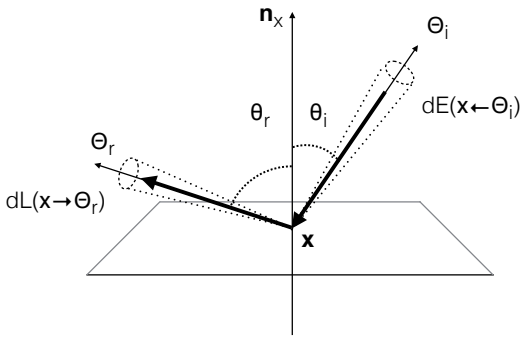

FIGURE 2.11: Schematic representation of a case of reflection where the the incoming light point on the surface and reflection point are coincident

dence on the incident light direction. The former condition leads to the Bidirectional Reflectance Distribution Function. This 4-dimensional function is the most common form encountered in computer graphics. Notable examples of BRDF are the Phong reflection model [40], the Ward model [41], the Blinn model [42], the Cook-Torrance model [43], the Lafortune model [44]. The simplest case is probably the Lambertian

reflection model [45].
The last simplification can be the viewing direction independence, that leads to the color texture, a 2d function or the bump maps, where only the geometry of the surface is important and no other characteristic of the surface.
In mathematical terms the BRDF is defined as [39]:

$$f_{\mathrm{r}}(\Theta_{\mathrm{i}},\, \Theta_{\mathrm{r}}) \;=\; \frac{\mathrm{d}\, L_{\mathrm{r}}(\omega_{\mathrm{r}})}{\mathrm{d}\, E_{\mathrm{i}}(\Theta_{\mathrm{i}})} \;=\; \frac{\mathrm{d}\, L_{\mathrm{r}}(\Theta_{\mathrm{r}})}{L_{\mathrm{i}}(\Theta_{\mathrm{i}}) \cos\theta_{\mathrm{i}}\; \mathrm{d}\, \Theta_{\mathrm{i}}} \tag{2.23}$$

referring to Figure 2.11. To be physical plausible, BRDFs must obey a set of three conditions [46]:

- positivity: $f_{\mathrm{r}}(\Theta_{\mathrm{i}},\, \Theta_{\mathrm{r}}) \geq 0$;
- Helmholtz reciprocity: $f_{\mathrm{r}}(\Theta_{\mathrm{i}},\, \Theta_{\mathrm{r}}) = f_{\mathrm{r}}(\Theta_{\mathrm{r}},\, \Theta_{\mathrm{i}})$;
- energy conservation: $\forall \Theta_{\mathrm{r}},\, \int_{\Theta} f_{\mathrm{r}}(\Theta_{\mathrm{i}},\, \Theta_{\mathrm{r}})\, \cos\theta_{\mathrm{i}} d\Theta_{\mathrm{i}} \leq 1$.

the Helmholtz reciprocity does not apply to moving, non-linear, or magnetic media. It states that light paths are reversible and generally holds because of the quantum-mechanical principle of time-reversal invariance [47] [48].

2.3.2 Glossy and matte surfaces

To understand how the BRDF can be used to describe different types of material, it is useful to consider two particular case: when the BRDF is a constant and when the BRDF is a δ function, such that for a generic continuous function $\phi(x)$ such that the condition $\int_{-\infty}^{+\infty} \delta(x)\, \phi(x)\; \mathrm{d}\, x = \phi(0)$ holds.
In the former case, the surface appears equally bright from all viewing directions and the BRDF is constant:

$$f_{\mathrm{lamb}}(\Theta_{\mathrm{i}},\, \Theta_{\mathrm{lamb}}) = f_{\mathrm{lamb}}(\theta_{\mathrm{i}}, \phi_{\mathrm{i}}, \theta_{\mathrm{r}}, \phi_{\mathrm{r}}) = \frac{1}{\pi}\rho_d \tag{2.24}$$

where ρ_d is a constant and it is called albedo. This ideal diffuse surface is also called Lambertian. It is, in a sense, the opposite of specular reflection: instead of reflecting only in one direction, it uniformly reflects in all directions. Even if real matte materials deviate from Lambertian behavior, usually for angles greater than 60 degrees [10], equation 2.24 is used for its computational simplicity.
Assuming a point light source at an angle $(\theta_{\mathrm{s}}, \phi_{\mathrm{s}})$, we can write that:

$$L(\lambda, \mathbf{x} \rightarrow \Theta_i) = \frac{E\delta(\theta_i - \theta_s)\delta(\phi_i - \phi_s)}{\sin(\theta_s)} \tag{2.25}$$

Substituting equation 2.25 and 2.24 in equation 2.23 leads to:

$$L(\lambda, \mathbf{x} \leftarrow \Theta_r) = \frac{1}{\pi}\rho_d E \cos(\theta_i) \tag{2.26}$$

that is the reason why the lambertian surfaces are said to obey a cosine law, or cosine behavior.
Another interesting example is the case of the ideal mirror: in this case the BRDF of the surface is proportional to the product of two δs:

$$f_{\text{spec}}(\theta_\text{i}, \phi_\text{i}, \theta_\text{r}, \phi_\text{r}) = k\delta(\theta_i - \theta_s)\delta(\phi_i + \pi - \phi_s) \tag{2.27}$$

where

$$h = \frac{1}{\sin\theta_i \cos\theta_i} \tag{2.28}$$

Substituting equation 2.27 in equation 2.23, it is possible to derive the complete equation for radiance, as:

$$L(\lambda, \mathbf{x} \leftarrow \Theta_r) = \int_{2\pi} \frac{k\delta(\theta_i - \theta_s)\delta(\phi_i + \pi - \phi_s)}{\sin\theta_i \cos\theta_i} E(\theta_i, \phi_i)\cos(\theta_i) d\Theta_i \tag{2.29}$$

A wide category of materials shows a behavior that is a combination of diffuse part and specular part. Those materials can be categorized with different degrees of gloss or glossiness. While an official measurement for gloss has been defined by ISO2813:2014 [49], there still is an ongoing debate on how to relate this measurement to the human perception of gloss [50] and how to improve it [51], [52], [53] [54]. Figure 2.12 exemplifies

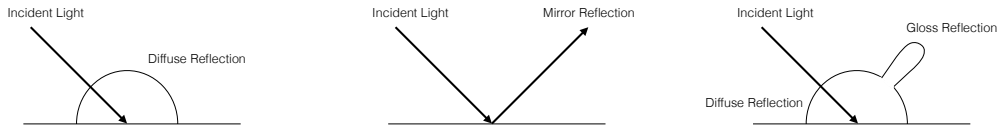

(A) Diffuse reflection. (B) Mirror reflection. (C) Mixed reflection.

FIGURE 2.12: Schematic representation of the reflection pattern for diffuse (matte), mirror and mixed materials.

what has been derived mathematically in the previous paragraphs. Figure 2.12a shows a schematic representation of the diffuse reflection, uniform from every viewing direction, depending only on the incoming light angle; in figure 2.12b the case of ideal mirror reflection is illustrated, all the light is reflected at the complementary angle, finally, in figure 2.12c the combination of the two extremes situation is represented, the gloss lobe

is the result of the mirror reflection component, and is strongly directional, related to the incoming light angle.

2.4 Computer graphics

Computer Graphics (or CGI, computer generated imagery) is a branch of computer science that aims to address the problem of displaying images on a screen. Those images can be acquired from a dedicated device, e.g. a photographic camera, or created by an appropriate software. The first steps of computer graphics took place from the invention of the first cathode ray tube, the Braun tube, in 1897 [55]. This starting point allows to display on a screen information previously encoded, from then on the technological advantages have been impressive. In the mid 1950s the first interactive computer graphics games were on the market, Pong by the company Atari is arguably the most famous example. In 1974, the Association for Computing Machinery initiated the Association of Computing Machinery's Special Interest Group on Computer Graphics and Interactive Techniques (SIGGRAPH) [56], which is the reference organization for conferences and publications in the world of computer graphics. The first three dimensional object rendered on a two dimensional screen was a Teapot, developed by Dr. Martin Newell at the University of Utah, and is therefore known as Utah Teapot [57]. The Utah Teapot is considered a keystone in computer graphics development because it showed the possibility to recreate a complex three dimensional object with a collection of polygons and the combination of a shader and a reflection model.

2.4.1 Shader and reflection model

The rendering process in computer graphics is a complex sequence of steps, occasionally depending on the specific technology, graphic card or drivers used. From the immense realm of computer graphics and its extensive taxonomy, only few concepts are going to be cited in this thesis. Further reading can be found in the following reference [58]
The term shading model refers to an interpolation technique used to give a more smooth and realistic 3d look to objects rendered from a mesh (collection of triangles or polygons in 3d space). Shading alters the color and appearance of specific parts of a 3d model, depending on the light direction in the scene, the type of light source, the material of the object and the position of the object in the scene. No modification of the geometry of the 3d model is performed at this stage, but it can occur earlier in the rendering pipeline, and it is usually called ray tracing or ray casting. Different shading techniques exist, the simplest example is flat shading. In this case the color for each polygon or triangle is based on the angle between the direction of the light source and the polygon's

surface normal, combined with the intrinsic color of the polygon, if any, and the kind of light source. Figure 2.13 shows an example of comparison between the flat shading

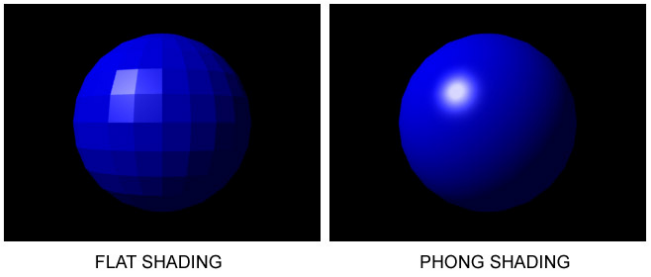

FIGURE 2.13: Different effect on the same mesh rendered with two different shading models: flat and Phong. Source in reference: [59]

model of a sphere, described by polygons, and a more smooth looking shading model, the Phong shading model. In the Phong shading model the normals are interpolated over each polygon, so to give the impression of a smooth surface.
The term reflection model refers to a local propriety of a material and has nothing to do with its geometry. There exists some confusion in the nomenclature, since there exists a Phong reflection model and a Phong shading model, and are commonly used in combination, where the Phong reflection model is used to describe the reflection proprieties of the surface. For example in Figure 2.13 both spheres use the Phong reflection model but only the right one uses the Phong shading model.
The reflection model is a function that models the reflection of a surface. Using the terms described in Figure 2.9 it is a SVBRDF. It can be eventually divided in two independent parts: a BRDF and a color texture. Furthermore the combination of BRDF, color texture and bump maps is used to describe irregular geometry, without the need of using a complex mesh. The Phong model is used, often in combination with a color texture, to render materials made of diffuse and specular parts. A list of common used reflection model includes:

- Phong reflection model [40], the oldest model, still widely used for its computational simplicity. Even if it gives satisfying results when rendering objects, its lack of physical plausibleness means that it cannot be fitted on real world data. To overcome this problem physical consistent Phong models have been developed by several groups of researchers, see section 2.4.2. The Phong model is the first model used in this work.

- Cook Torrance model [43], a more physically correct model, that includes a Fresnell term and a roughness term. It principal downside is its high computational cost. This is the reason why it was not chosen for this thesis work.

- Ward isotropic and anisotropic model [41], an attempt to create a physically plausible and computational efficient model. The Ward model could be an interesting following step for this work.

2.4.2 Phong model

The Phong model (PM) was presented in a classic paper by Bui Tuong Phong [40] and later improved see references [46] [60] to consider the physical constraint for BRDF. Figure 2.14 shows a schematic representation of the several components of the PM. The PM divides the reflection of incoming light into three components: ambient component, diffuse reflection and specular reflection. The model is usually described by equation:

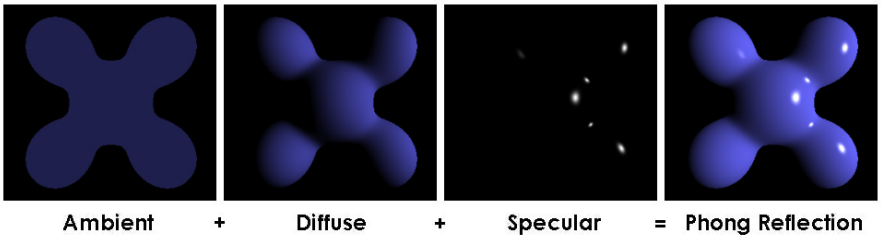

FIGURE 2.14: schematic representation of the several components of the Phong model. Source in reference: [61]

$$L_r = k_\mathrm{a} L_\mathrm{a} + \left[k_\mathrm{d}(\mathbf{N}\cdot\mathbf{S}) + k_\mathrm{s} F_s(\mathbf{S},\mathbf{V})\right] L_\mathrm{i} \tag{2.30}$$

where k_a is the ambient reflection coefficient, k_d is the diffuse reflection coefficient, k_s is the specular reflection coefficient, L_a is the ambient radiance, that represents the sum of all the contribution to the object reflection that are coming from the surroundings (back scattering, secondary scattering, etc...), L_i is the incoming radiance, L_r is the reflected radiance and $\mathbf{N}$ is the vector normal to the surface, $\mathbf{V}$ is the normal vector pointing in the viewer direction and $\mathbf{S}$ is the normal vector pointing in the light source direction. $F_s(\mathbf{S},\mathbf{V})$ is the specular shading function, and in its original version [40] was

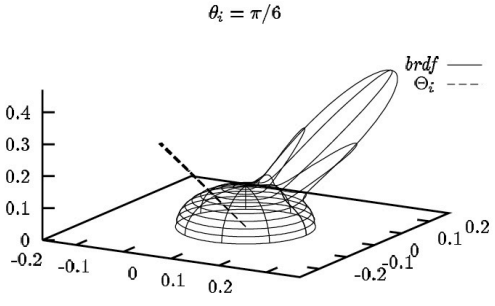

FIGURE 2.15: Polar diagram of a Phong BRDF for a fixed incident incoming light [60]

expressed as:

$$F_s^P(\mathbf{S},\mathbf{V}) = \begin{cases} [(2\mathbf{N}(\mathbf{N}\cdot\mathbf{S})-\mathbf{S})\cdot V]^{n_p} & [...] \leq 0 \\ 0 & otherwise \end{cases} \tag{2.31}$$

where n_p is the Phong specular reflection exponent. Another choice, that lead the Phong model to be physically plausible comes from reference [42]:

$$F_s^B(\mathbf{S},\mathbf{V}) = \left[\mathbf{N}\cdot\left(\frac{\mathbf{S}+\mathbf{V}}{|\mathbf{S}+\mathbf{V}|}\right)\right]^{n_B} \tag{2.32}$$

where n_B is the Blinn specular reflection exponent. Figure 2.15 shows the polar diagram of a Phong BRDF with $K_d = 0.4$, $k_a = 0.05$, $k_s = 0.6$ and $n_B = 50$ for an incident light with an incoming angle of $\frac{\pi}{6}$. It is clearly visible the specular lobe and the diffuse lobe, as described in Figure 2.12c

2.5 RTI

In section 2.4 the focus has been on how to reproduce a realistic appearance of an object using computer graphics and reflectance models. In principle it could be possible to acquire reflectance data with a dedicated device, a goniophotometer. Such an acquisition device allows to measure the light reflected by a surface at different incident angles and it is used to detect the BRDF of a single point on a surface [62]. Ideally it is possible to use the data obtained by this device, fit a mathematical model on those data, and then use them in software frameworks that render scenes and objects based on information about the geometry, the light set-up and the BRDF of each material. Examples of those softwares are Blender [63] or Radiance [64]. Since the start of this PhD project, those possibilities were explored, but several issues indicate that this was not a convenient approach for the objectives of this work. Firstly the acquisition process with a goniophotometer takes several hours and provides information of the BRDF of a single point, it would be impractical to use it to acquire a SVBRDF. For example, let's consider a 20cm$\times$20cm surface, scanned over 7360×4912 points (the number of pixel of a Nikon D800 camera), that requires to measure the BRDF for order of $3\cdot10^7$ points, definitely an unpractical measurement. Secondly the data provided by the goniophotometer can be described only by a function with 2-dimensional domain and 2-dimensional codomain, making it a complex function to model, although in the last 10 years several works focused on this topic, see references [65], [66], [67]. Lastly, rendering a scene with softwares like Blender or Radiance can take a time between some seconds and a few days, depending on the complexity of the scene and the computer power, in any case too much for an interactive tool, where the requirements are to be able to recalculate the scene in approximately $\frac{1}{30}\approx0.033$s. This value was chosen as the minimum frame rate to perceive motion fluidness, although this limit depends strongly on the subject rendered, see reference [68] .

A promising method to solve those limitations is Reflectance Transformation Imaging [69] [1]. According to the definition given by the Cultural Heritage Imaging group (CHI): "RTI is a set of computational photographic methods that capture a subjects surface shape and color and enables the interactive re-lighting of the subject from any direction based on a mathematical model [70]". CHI has been the most active nonprofit organization in developing RTI, to advance the state of the art of digital capture and documentation of the worlds cultural, historic, and artistic treasures.

2.5.1 Status of the art

The first computational RTI method was originally developed in 2001 by HP-Labs [2] under the name Polynomial Texture Mapping (PTM). The reflection of light is in a first step captured by multiple photographs illuminated from different positions. Figure 2.16 shows the structure (dome) developed by researchers in HP-labs for acquiring pictures from several light directions. For every single capture the camera is mounted in the same, fixed position. This simple idea allowed to limit the number of parameters, from a 6 dimensional SVBRDF function to a 4 dimensional function. For clarity let's rename: $\text{SVBRDF}(\mathbf{x}, \mathbf{\Theta_i} \rightarrow \mathbf{\Theta_r},) = \text{SVBRDF}(\theta_i, \phi_i, \theta_r, \phi_r, x, y)$, where $\mathbf{x} = (x, y)$ is a point on the surface, $\mathbf{\Theta_i} = (\theta_i, \phi_i)$ is the incoming light solid angle and $\mathbf{\Theta_r} = (\theta_r, \phi_r)$ is the reflected light solid angle. The reflectance function resulting depend on $I(\theta_i, \phi_i, x, y)$, two spatial coordinates and two angles, representing the direction of the incident illumination.

The second step, involves a further assumption, using a RGB non-linear color space (for example sRGB), the reflectance function is computed for each color channel, resulting in a system of equation:

$$\begin{cases} \mathrm{R_c}(x, y) = L(x, y)\mathrm{R}(x, y) \\ \mathrm{G_c}(x, y) = L(x, y)\mathrm{G}(x, y) \\ \mathrm{B_c}(x, y) = L(x, y)\mathrm{B}(x, y) \end{cases} \tag{2.33}$$

where $(\mathrm{R_c}, \mathrm{G_c}, \mathrm{B_c})$ are the RGB values depending on the light direction, $L(x, y)$ is the luminance model and $(\mathrm{R}, \mathrm{G}, \mathrm{B})$ are the unscaled RGB values, that do not depend on the incoming light.

FIGURE 2.16: The first Dome developed in 2001 for acquiring PTMs. Source in reference [2]

In a third step a simple mathematical term, typically a polynomial of second order is fitted to the luminance model:

$$L_{\text{PTM}}(l_u, l_v, x, y) = p_0^{(x,y)} l_u^2 + p_1^{(x,y)} l_v^2 + p_2^{(x,y)} l_u l_v + p_3^{(x,y)} l_u + p_4^{(x,y)} l_v + p_5^{(x,y)} \tag{2.34}$$

defined by 6 parameters $p_i^{(x,y)}, i : 0, ..., 5$, where the pair of coordinates (x,y) represent a single pixel on the picture, and l_u, l_u are the coordinates of the normalized vector describing the light direction. Given $N+1$ images, it is possible to fit the coefficients $p_i^{(x,y)}$ for each pair of coordinates (x, y). The fit method suggested in the original paper [2]

relies on the classic singular value decomposition algorithm (SVD) [71] to solve the following overdetermined system:

$$\begin{bmatrix} l_{u0}^2 & l_{v0}^2 & l_{u0}l_{v0} & l_{u0} & l_{v0} & 1 \\ l_{u1}^2 & l_{v1}^2 & l_{u1}l_{v1} & l_{u1} & l_{v1} & 1 \\ \vdots & \vdots & \vdots & \vdots & \vdots & \vdots \\ l_{uN}^2 & l_{vN}^2 & l_{uN}l_{vN} & l_{uN} & l_{vN} & 1 \end{bmatrix} \times \begin{bmatrix} p_0 \\ p_1 \\ \vdots \\ p_5 \end{bmatrix} = \begin{bmatrix} L_0 \\ L_1 \\ \vdots \\ L_N \end{bmatrix} \tag{2.35}$$

This approach is convenient from several points of view: only little amount of hardware and software is needed to acquire a PTM, stability and reproducibility are easy to guarantee because of a reliable fitting procedure and only relatively little knowledge to operate the tools is required. The major drawback of PTM is the limitation of the applied mathematical model. A second order polynomial is able to reproduce reflection of diffuse surfaces, also called a lambertian surface, while the realistic reproduction of gloss is not possible. The limitation of the second order polynomial is crucial for the reproduction of many objects and artworks like, for example, mosaics. A mosaic is constructed to interact with light and in most cases diffuse and glossy materials are placed on purpose to constitute the artwork in a specific manner.
In the case of a lambertian surface, further informations about the surface can be extracted from a PTM [2]. Setting

$$\frac{\partial L}{\partial x} = \frac{\partial L}{\partial y} = 0 \tag{2.36}$$

it is possible to derive

$$\begin{cases} l_{uO} = \frac{p_2 p_4 - 2p_1 p_3}{4p_0 p_1 - p_2^2} \\ l_{vO} = \frac{p_2 p_3 - 2p_0 p_4}{4p_0 p_1 - p_2^2} \end{cases} \tag{2.37}$$

Using this values that maximizes the function 2.34, it is possible to estimate the surface normal as:

$$\mathbf{N} = (l_{uO}, l_{vO}, \sqrt{1 - l_{uO}^2 - l_{vO}^2}) \tag{2.38}$$

The accuracy of the normals extracted using this method has been studied and compared with other techniques such as photometric stereo and laser scanning, with test objects [72] [73]. It has been shown that the accuracy is of lower quality, compared with other techniques. However the other methods rely on additional equipment, compromising one of the main advantages of RTI/PTM, its simplicity of use and absence of need for multiple devices. In reference [74] an other technique is suggested, that relies on pre-processing the data coming from the dome, using photometric stereo techniques. This techniques is quite interesting in term of accuracy of detected normals, and does not require additional hardware, it must be noticed that requires more computing power

and pre-processing than the original technique in reference [2]
In the original article [2] the researchers suggested another useful feature of PTMs: using the result from evaluating the PTM function, it is possible to simulate the specular component of standard lighting equation, allowing to modify the appearance of a PTM, introducing a specular component. Equation 2.30 can be integrated with the luminance model in equation 2.34, for example:

$$L_r = k_\mathrm{a} L_\mathrm{a} + \left[k_\mathrm{d}(\mathbf{N} \cdot \mathbf{S}) + k_\mathrm{s} F_s(\mathbf{S}, \mathbf{V})\right] L_\mathrm{PTM} \tag{2.39}$$

Furthermore an other function to describe the luminance model $L_\mathrm{PTM}(l_u, l_v, x, y)$ have been proposed [66], that has been developed in 2007-2008 by a team at UC Santa Cruz. The solution presented uses a different base for the decomposition. Instead of a polynomial base as in the original technique [2], a Spherical Harmonics over the upper Hemisphere base is used. In this case the number of coefficients depend on the order of Spherical Harmonics function is selected. It has been shown that HSH is significantly performing better than PTM when the order of the Spherical Harmonics is greater than 9 [75]. Unfortunately this limits the convenience of using HSH, since significantly more parameters than the PTM models are required to get sensibly better results. Meaning that more memory to store data is needed and more computational power is required to compute the fit and more date is necessary to gain reasonable results.
During the 16 years since the first article [2] about PTM was published, several improvements were done. Some of them were aiming at extracting information about the surface characteristics: in reference [76] the authors used the normal extracted from equation 2.38 to obtain a indicator of roughness of the surface and a 2D normal filter called “unasharp Masking Normals”, that filters out low frequency components, for example paper undulations. Furthermore, a team of researcher under the lead of Prof. M. Drew, at Simon Fraser University, presented an upgrade of the PTM luminance model described in equation 2.34, for reference see [77], [78], [79], [75]. In their work the authors suggest to change the fitting algorithm, using a Robust regression [80], combined with a small change in the PMT luminance model, using as a basis for the polynomial $(u, v, w, u^2, uv, 1)$, instead of the previously used $(u^2, v^2, uv, u, v, 1)$, where $w = \sqrt{1 - u^2 - v^2}$. Consequently it is possible to model highlights and matte separately and avoid problems caused by shadows and specularity components. Using a robust regression technique improves the stability of the color and normals measurement resulting form the fit, but it comes at the cost of significantly increasing the time needed to compute the luminance model for all pixels. The solution proposed has been tested with an implementation written by the author of this thesis (it was not possible to obtain the source code form the authors) and the results obtained on a Intel core i7-6700K machine (Ubuntu 16.04), using gcc version 5.4, and ROOT TLinearFit library [81], showed a

time increase of over approximately 500 times for the robust regression over the singular value decomposition. This is a negative trade-off, because one of the crucial advantages of PTM over other methods is the high speed of computation and little time required. Using a robust regression would not allow the fitting process to be done on-the-flight on a laptop, but would require a dedicated machine running for few dozen of minutes.
A group of Italian researchers at CNR in Pisa, under the lead of Prof. Roberto Scopigno, started to implement software to view RTI both PTM and RTI in 2010 [82], [83]. They developed two versions of viewers for RTIs, a desktop application for Windows/Mac written using QT libraries [84], and for a browser, using a version of the OpenGL libraries for the web (webGL [4]) and a JavaScript library developed by their group, SpiderGL [85] [86] [87].
In the same year Dr L. W. MacDonald at Universiy College of London published his first results of a new model for rendering metal using RTI techniques [88]. His idea is to use a Lorentzian peak and a linear flank to model the luminance:

$$f(\omega) = \frac{p_a}{1 + (\omega/p_s)^2} + (f_a\omega + f_s) \tag{2.40}$$

where ω is the arcosine between the lighting direction and the vector identifying the specular reflection lobe, p_a, p_s and f_a, f_s are parameters for amplitude and scaling. Although this model gives arguably the best visual results, it suffers for the same problems of Prof Drew approach: more computing time is needed to perform the fitting and there is no immediate way to render the result in real time, using commonly available technologies.
Recently, a group of researcher from French universities developed a novel approach that competes with PTM and HSH. It is called Discrete Modal Decomposition and is based on a particular Eigen basis derived from structural dynamic problem [89]. The proposed approach seems to be a direct competitor of the HSH method, although it suffers from the same criticalness: no way to integrate it in a real time rendering engine has been proposed. In the last 5 year there has been a shift on interest of researchers. Rather than focusing on the fitting model, improving the lighting part has been a priority, for example:

- RTI assumes that lights are "infinitely far away" and that there homogeneity on the illumination on the surface. This is of course possible only in theory, in practice it is required to have a dome of adequate size, to make those effects negligible. A group of researchers proposed a solution for near light correction [90].
- The size of the object is limited to the size of the dome, in standard RTI. Two groups of researchers proposed a method to acquire large scale objects by merging together different RTIs [91], [92].

- RTI assumes that the coordinates of the lights are known a priori. This is usually the case in a dome, but it is unlikely the case when taking free-hand images. A group of researchers explored the possibility of extracting the information about the light direction from the photos itself [93].
- It is possible to generate a RTI of a big object - for example a painting - by stiching togheter several smaller RTIs. A group of researchers at University of the West of England proposed a workflow [94] for this purpose.

2.5.2 Applications of RTI technologies

RTI's have been used in a wide range of application, although the main field of application has been, since its beginning, archeology. The first artifact presented as a RTI/PTM is a 4000 year old neo-Sumerian tablet [2]. In figure 2.17a is presented an original photo of the tablet, while in figure 2.17b a PTM rendering, with specular enhancement is shown as a comparison. In 2006 the PTM technique was used to decode an ancient

(A) Normal photograph (B) Specular enhanced

FIGURE 2.17: Normal photograph and specular enhanced PTM representation of neo-Sumerian tablet [2].

Greek astronomical calculator [95], known as Antikythera Mechanism, a complex clockwork mechanism, generally referred as the first known analogue computer [96]. The PTMs images helped decoding unreadable parts, covered in rust. In 2010 a review of possible uses in Archeology was presented on Journal of Archaeological Science [97] and it was presented a review on principles and best practices for RTI acquisition in GLAM (Galleries, Libraries, Archives and Museums) institutions [98]. RTIs have been used on a variety of artifacts: from ancient Greek red-figure vases [99], to ancient Egyptian artifacts [100], from parchments, such as the Dead Sea Scrolls [101] to bones, analyzing their surface modifications [102]. RTIs have been used extensively to acquire collections of Coins [103], [104], [83] and ancient wall graffiti [105]. Recently RTIs have been used to acquire underwater cultural heritage objects [106], using a special waterproof dome.

RTIs have been evaluated as a possible technique of interest for forensic analysis [107]. Furthermore application in the field of anomaly detection for surface quality inspection has been proved to give interesting results, see reference [89]
During the years of use of RTIs technology, relatively little effort has been spent to build a easy to use and practical RTI viewer. The only two examples, publicly available so far, are software developed by CNR in Pisa [82] and a more generic tool, RTI compatible, for Shared Analysis in Cultural Heritage [108].

2.6 Non Visible range photography and RTI

Photography, and consequently the development of camera sensor, has always been focused on accurate color reproduction. This started to change when special films were developed that were more sensible to infrared light [109] respect to normal color and black and white films. Non-visible photography began to be a widely explored field when silicon detectors started to take place [110]. Silicon imaging sensors can be quantum or temperature detectors, that convert radiative energy into an electrical signal. Quantum detectors convert photons of a range of wavelength into electrons, while thermal detectors detect the absorbed energy by secondary effects associated with changes in temperature [111].
An ample assortment of imaging sensor is available nowadays, covering a range of wavelength from gamma rays to infrared. The two most successful architectures are Charge couplet devices (CCD) and active-pixel sensor complementary metal-oxide semiconductor (APS CMOS, or only CMOS) [111]. In CCDs pixels are represented by p-doped metal-oxide-semiconductors (MOS) capacitors. When the sensor has been exposed, each capacitor transfers its charge to its neighbor. The last capacitor is connected to an amplifier, that transform the charge in voltage. In APS CMOS each pixel contains at the same time a photodetector and an amplifier. CCD are the better performing sensors, and are mostly used in applications where a high level of sensitivity is required. CMOS have always been used on photographic cameras, mainly because they are cheaper. In the last 15 years CMOS sensors have been improving significantly and are now reaching the quality of CCD sensors [112] [113] [114].
To quantify the efficiency of a silicon image sensor, a quantity called quantum efficiency is usually defined. A photon with frequency ν carries an energy $h\nu$, where h is Plancks constant, the quantum efficiency η, depending on the frequency, can be defined as:

$$\eta = \frac{N_e}{N_\nu} \tag{2.41}$$

where the N_e is the number of induced elementary charges e, and N_ν is the number of photons with frequency ν. Figure 2.18 shows the quantum efficiency for a 128x128 pixels CMOS APS sensor in 1995 [115]. While the quantum efficiency has increased in modern sensors, the figure shows an interesting features of CMOS that is also present in modern sensors: their sensitivity range goes well above and below the visible spectrum. This characteristic is a problem in normal cameras, since the extra wavelengths don't provide useful information for standard photography. For this reason each modern camera has at least three kind of filters: a Bayer filter [116], infrared (IR) blocking and ultraviolet (UV) blocking filters [110]. Bayer filter (or Bayer filter matrix) is a color filter array (CFA), a matrix of color filters placed over each pixel sensors. Each minimal sub-matrix is composed of a blue, a red, and two green passband filters. The IR and the UV blocking filters are needed to exclude all the light coming from outside the visible spectrum. Although the passband filter on the Bayer filter should be enough in principle, their efficiency is limited to the visible range, and some wavelength can pass outside that range.

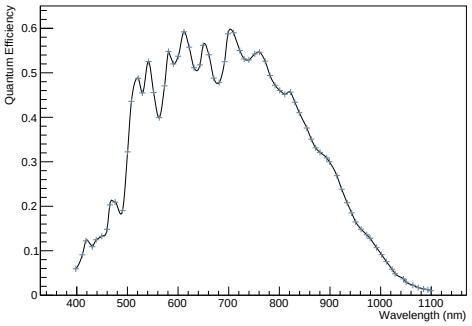

FIGURE 2.18: Typical quantum efficiency for a CMOS sensor [115]

UV and IR photography usually uses specific sensors and no filters. Although, since on some models of commercially available cameras it is quite easy to remove the IR and UV blocking filters, this possibility has been explored by researchers [109]. The classical set-up includes an UV or a IR light source illuminating a surface. Under this light condition a photo is taken, that records reflection and fluorescent effects of the surface, possibly revealing hidden features. In general, emitted fluorescent light has a longer wavelength and lower energy than the absorbed light [117]. This means that also limiting the acquisition to the visible range, it is possible to reveal interesting features illuminating with UV light.

These techniques have been used, for example, to identify pigments on a painting [118], to inspect the authenticity of a work of art [119] or to discover archaeological features no more visible [120]. RTI algorithms are not adapt to be used with UV and IR illumination, since those ranges of wavelength excites fluorescence in materials, and this would violate the basic assumption of SVBRDF (see section 2.3.1, that there is no sub surface scattering and no significant delay in the reflection. Anyhow UV/IR photography can be used as a complementary technique of RTI, to highlight features that are invisible in the visible range.

Chapter 3

Experimental Set-up(s)

3.1 Introduction

The following section is dedicated to the detailed description of the various experimental set-ups that were build and used during the project. In the current literature there is no standard procedure for building a dome for RTI/PTM acquisition. So far, each researcher or group of researchers developed their own dome, resulting in a wide variance of materials, shapes and sizes. Furthermore the number of light sources that should be used is not uniquely defined, although the minimum number of lights is determined by the model used. To exemplify: using the PTM model (see equation 2.34), the number of light sources should be bigger than 6, to extract the parameters with the algorithm described by the system of equation 2.35. Although a substantial increase in the number of light sources gives more stability and consistency to the results.
The first prototype of a dome structure used to acquire RTI/PTMs was developed in 2001 at HPLabs, as described in reference [2]; although the size of the structure is not reported, the number of light used is 50. Another example is the acrylic hemispherical dome developed by Dr. MacDonald, that has a diameter of 1030 mm and is equipped with 64 flash lights [72].
During this research project, the author of this thesis and Dr. Peter Fornaro have been developing several devices, always following a quality driven approach. This meant that the development of the newer dome started always from the analysis of the problems encountered using the older one. Therefore experiences made with each device is of fundamental importance to build the next one. Several aspects have been considered when comparing the performances of different devices, for example:

- quality of each image acquired, in term of sharpness, stability, color and exposition;

- portability of the device and easiness of use on the field (libraries, old churches, museums, etc.);
- consistence of results;
- quality of the resulting RTI/PTMs.

The domes are presented in the text in chronological order starting for the first dome made of polystyrene (see section 3.2), following with the big dome (see section 3.3), ending with the last prototype developed in collaboration with a Bron Electronic AG (see section 3.4). Furthermore, to acquire some RTI/PTM of bigger size a free hand technique has been used (see section 3.5), that uses only one light source that is moved by one man (usually the author of this thesis).

3.2 First dome made of polystyrene

The first prototype of dome has been a polystyrene hemisphere, painted with black paint to minimize inter-reflections. The First Polystirene Dome (FPD) is shown in figure 3.1, while been used for the acquisition of objects in the Stiftskirche St. Michael in the village of Beromuenster. The sizes of the FPD are: 750 mm in diameter and 375 mm in height. It is equipped with 58 Seoul Z-Power LED P4 cold white light LEDs [121], with declared light temperature between 4700 K and 5000 K. On top of the hemisphere a Nikon D810, a 36.3 megapixel full-frame camera is mounted. The LEDs are synchronized with the camera by standard TTL flash-trigger signals, and are powered by a custom made electronic driver. In Figure 3.2 is shown the typical SPD as declared from the constructor (black line) compared with the standard human eye response [121]. This graph shows a typical characteristic of white light leds. Since there exist no white light emitting diode, usually they consist of a Blue/UV diode covered with a yellow-orange phosphor, a substance that exhibits the phenomenon of luminescence and emits light to cover the missing wavelength. Advances in building technology made it possible to have a continuous distribution of light over the visible spectrum, without significant gaps. Anyhow, the contribution of the various components is easily noticeable: a high blue peak and a secondary flat component for the phosphor. Using a spectrometer (in this work the Sekonik Spectromaster C7000 [122] has been used) it is possible to measure the SPD for various exposition times. The exposition time represent the time the sensor is exposed to the light, and is usually expressed as a fraction of unity, for example, typical exposition times are: 1s, 1/30s, 1/60s 1/125s, 1/250s, etc. The exposition time for a photo is selected in combination with the opening of the lens diaphragm through

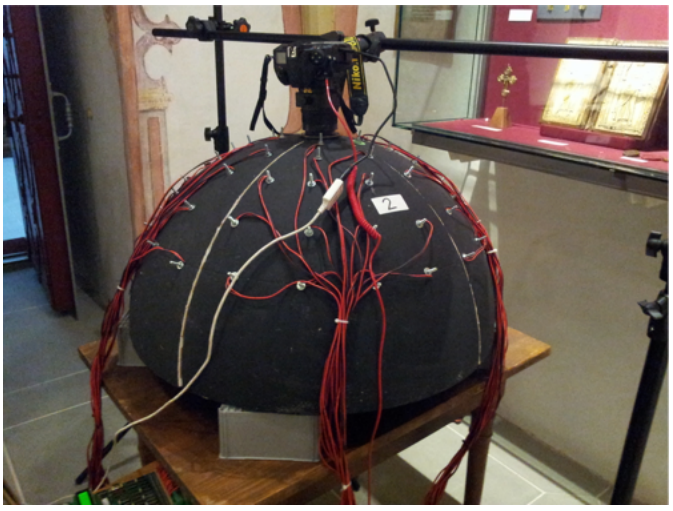

FIGURE 3.1: Photo of the First Polystirene Dome used during an acquisition in the Stiftskirche St. Michael

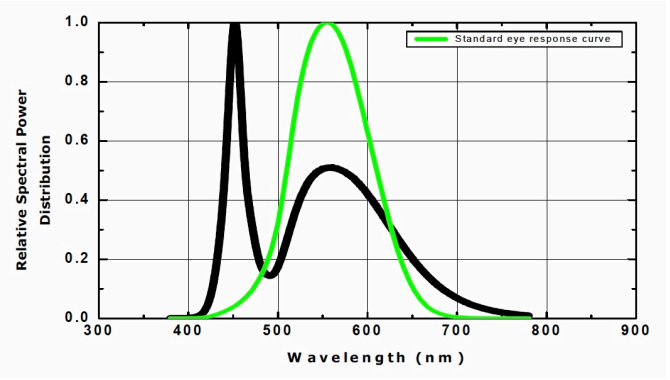

FIGURE 3.2: Declared SPD of a Seoul Z-Power LED P4 "col" white light leds(black), standard eye response curve(green) [121]

which light passes (aperture). In principle there is no absolute-correct combination. A compromise has to be found selecting the exposition time and the aperture that better fits the requirements regarding steadiness and depth of field. Figure 3.3 display a set of 4 measurement of the SPD of one led on the dome, at different exposition times: 1s, 1/10s, 1/30s and 1/250s. The Y-axis is in logarithmic scale. It can be noticed that the luminous exposure, which SI unit is lux times second, decreases quite significantly, when the exposition time is shorter. This is a typical characteristic of LEDs, that are commonly referred as a not-fast light source. Furthermore, the shape of the SPD apparently varies depending on the exposition time. When the exposition time is lowered significantly, some of the components are not significant anymore. This effect has to be taken into account, since when taking detailed photographs (commonly called macro photo or macro) a short exposition time allows to increase sharpness avoiding micro-movements of the camera. Furthermore a shorter exposition time allows to neglect ambient light contributions. To overcome this limitation an exposure time between 1/30s and 1/60s

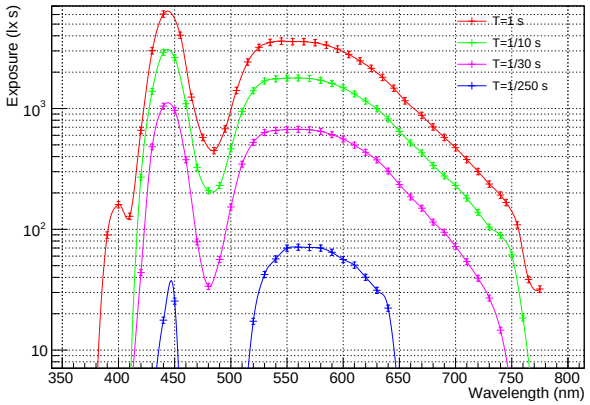

FIGURE 3.3: SPD of a LED in the small dome, each color represent a different exposure time

has to be selected when using the FSD. In certain scenarios, for example if the set-up is not still enough, an exposure time of 1/30s could be to slow.
Figure 3.4 shows the SPD (the Y axis is linear) for three different LEDs mounted on the dome. The difference in shape between the different SPDs has to be taken into account correcting the color balance when calibrating the photos, see Section 3.6. A

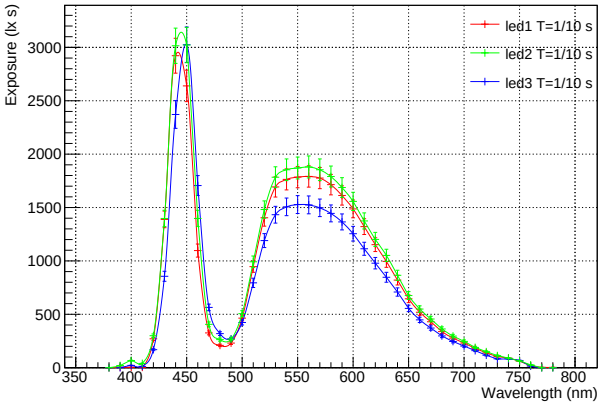

FIGURE 3.4: SPD of three different LEDs of the small dome, exposure time 1/30 s

further requirement for the acquisition device is to be easily movable. For example it can be important to be able to move the FSD to new location to acquire an object that cannot be moved. This poses important challenges on the engineering. The dome can be divided in 4 parts (slices) that can be re-assembled, making the FPD easily movable, but creating a problem with the calibration of the light sources. Indeed, de-assembling and re-assempling the dome causes the LEDs to move and change position. Figures 3.5a and 3.5b show the distribution of light sources in the l_u, l_v plane, defining a vector $\mathbf{V} = (l_u, l_v, \sqrt{1 - l_u^2 - l_v^2})$ pointing the light source and starting from the center of the sphere, as defined in section 2.5, calculated with the methods described in section 3.6.3.

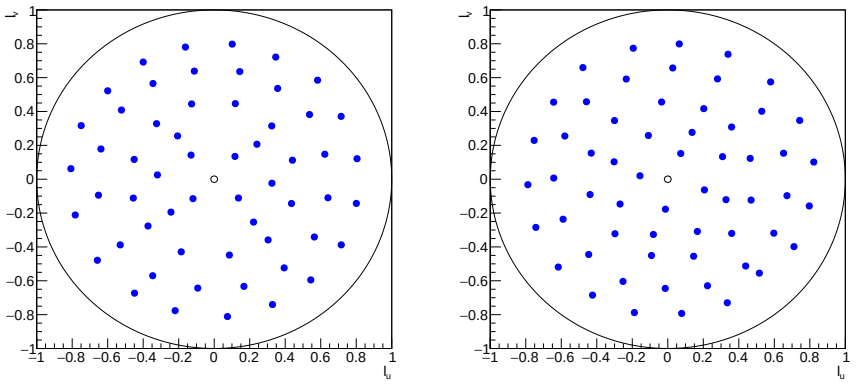

(A) (B)

FIGURE 3.5: Small dome light positions (blue dots), circumference of radius 1 and center position are also marked

Figure 3.5a represent the light distribution of the FPD before the de-assembling and figure 3.5b is the light distribution of the dome re-assembled for the acquisition. The differences are taken into account by the calibration, see 3.6.3, but this is a clear inconvenience: the calibration has to be repeated each time and it is a possible source of errors for further analysis.

3.3 Big dome

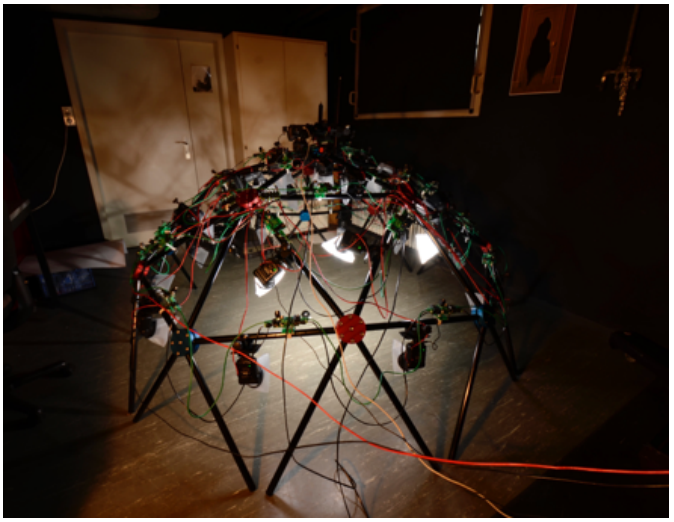

FIGURE 3.6: Photo of the Big Dome in the DHLab

The structure called Big Dome (BD), see Figure 3.6, has been developed to overcome some of the major drawbacks of the FPD. This structure has been build as a geodesic dome, a half hemispherical bucky-ball structure based on a network of elements that intersect to form triangular shapes, which have local rigidity, and so distribute stress

throughout the structure.
The BD is made of aluminum tubes of different length and aluminum connectors, red and blue, respectively made do accept five or six aluminum tubes ends. The BD can be equipped with approximately 30 to 50 commercial photo flashes powered by a external high current power supply for short recharge times. The structure is approximately 2010 cm in diameter and 1040 cm in height. It is a prototype that can be made out of various material and in different sizes. A high resolution digital SLR (Nikon D810 or D600) is mounted on the structure. The flashes are Metz MECABLITZ 36 C-2, with nominal color temperature of 5600 K. They are synchronized with the camera by a custom made bus-system with multiple decoders and a control unit. The bus-system to control the light allows to remotely address six different outputs per decoder that can control various types of light sources, e.g. VIS, UV or IR LEDs or lamps or flashes based on other technologies. The decoders wired by RJ45 compatible cables, they are

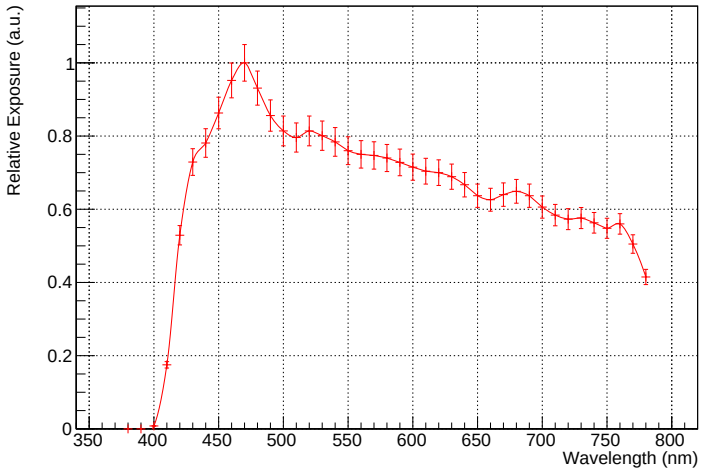

FIGURE 3.7: SPD of a flash in the Big Dome

fully addressable and each decoder can be configured to control the lamp at a specific duration and power of illumination.
Important characteristics of the flash lights are:

- the light distribution does not vary depending on the exposition time; this happens because flash lights are optimized to release all the luminous exposure in a time shorter then 1/250s;
- the SPD of a flash light is optimized to be as close as possible to a CIE standard illuminant, for example the D65, see Figure 3.8 that display the SPD of a flash used and Figure 3.7 that compare the D65 standard illuminant with the black body radiation curve for $T = 6504K$.

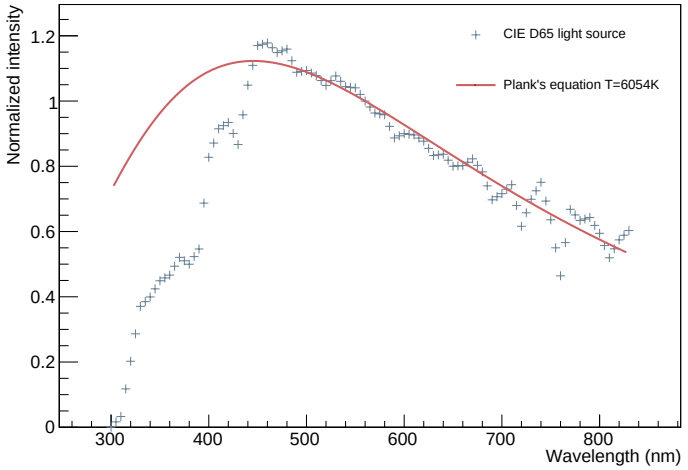

FIGURE 3.8: Comparison between black body radiation curve (6504K) and CIE Illuminant D65.

These advantages are counterbalanced by some disadvantages:

- Each flash had to be powered by 4 AA 1.5 V batteries, that lasted a limited amount of time. To avoid the inconvenience of changing batteries too frequently, a placeholder for the batteries has been 3d printed and substituted to the batteries. All the placeholders are connected together, so that the flashes can be powered by an power supply. Nevertheless they require much more electrical power than LEDs, consequently reducing the mobility of the dome.
- Each flash requires a time to reach full power after being fired, usually in the order of few seconds. Current of up to 50A are not special to this set-up This time limits the speed of the acquisition, introducing possible artifacts in sharpness due to micro-movements of the camera or of the target. To overcome this limitation the dome has to be set up on an surface that is not influenced by vibrations.

Figure 3.9a and figure 3.9b show distribution of 18 light sources in the l_u, l_v plane for two different light set-up that have been tested. It was not possible to increase significantly the number of light sources because of the intrinsic limitations posed by the volume occupied by flashes and electronics. Another inconvenice of the BD is the difficoulty of distributing uniformly the light sources, due to the volume occupied by the electronics components. While it is not a major limitation for the robustness of the fitting algorithm, it causes problems since the BRDF is not sampled uniformly. This leads to missing data in the gloss region for points that belong to surfaces which normals are not aligned with the optical axis of the camera.

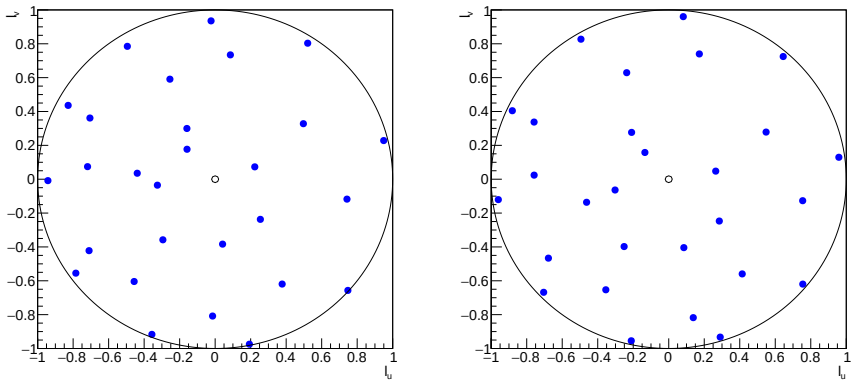

(A) (B)

FIGURE 3.9: Big dome light positions (blue dots), circumference of radius 1 and center position are also marked

3.4 BronColor dome

The experience made with the FPD and the BD made it possible to improve further on. The collaboration with Bron Elektronik AG, a company located Allschwil, lead to the development of the BronColor Dome (BCD). Its setup consists of a dome structure (see figure 3.10b and figure 3.10a) made of a composition of aluminum and acrylic plastic. The device is equipped with 48 white-light LEDs (Cree XLamp XHP50 [123]) powered by external custom-made electronics for automated control of the measurement process. The structure is approximately 425 mm in diameter and 220 mm in height and can be mounted on a tripod. A high resolution digital SLR (Nikon D810 or D600) is mounted on the structure. Figure 3.11 display a set of 4 measurement of the SPD of one led on the BCD, at different exposition times: 1s, 1/10s, 1/30s and 1/250s. The Y-axis is in logarithmic scale. It can be noticed that the luminous exposure decreases quite significantly, when the exposition time is shorter. Furthermore, the shape of the SPD varies depending on the exposition time but is more stable than the SPD of the FPD 3.3. The LEDs mounted on the BCD allows to select an exposure time between 1/60s and 1/125s, that results to be optimal for macro-photos taking.

Figure 3.12 shows the SPD (the Y axis is linear) for three different LEDs mounted on the dome. The difference in shape between the different SPDs has to be taken into account when calibrating the photos, see Section 3.6. It can be noticed that the luminous exposure varies depending on the LED. This factor has been taken into account when calibrating. It can also be noticed that the LEDs chosen for the BCD have a more flat distribution in the green and red region. This is an important improvement for what regards color reproduction, because it allows a more uniform color sampling.

Figure 3.13 shows the light sources distribution in the l_u, l_v plane for the BCD. Compared

(A) Structure of the BCD, image courtesy of Broncolor

(B) Photo of the BronColor Dome

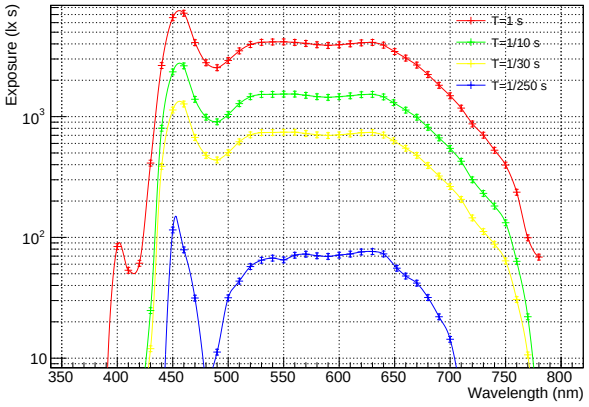

FIGURE 3.11: SPD of a LED in the BCD, each color represent a different exposure time

to the other two domes the symmetry of the disposition of the light sources has been improved. The stability of the light positions is greatly improved. At the same time the BCD is a device easy to carry and to move.

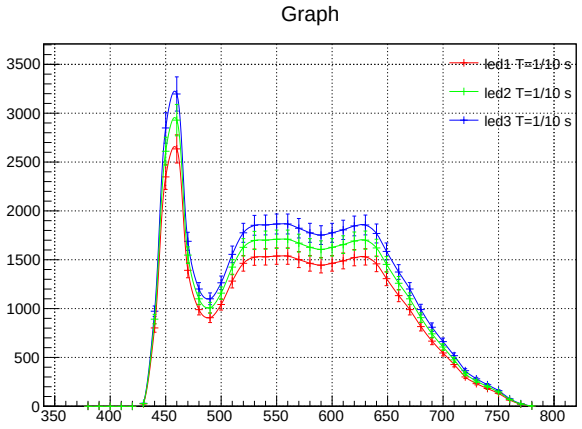

FIGURE 3.12: SPD of three different LEDs of the BCD, exposure time 1/30 s

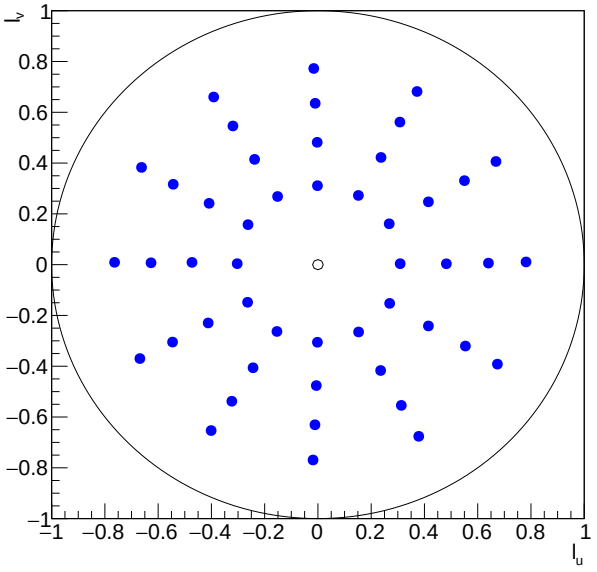

FIGURE 3.13: BCD light positions (blue dots), circumference of radius 1 and center position are also marked

3.4.1 UV and IR

The BCD has been produced in two exemplars. The first one is equipped with only white light leds, while the second has been equipped with a series of ultraviolet (UV) and infrared (IR) emitting leds.

The UV emitting leds are *led engin violet emitter 400nm*. These light sources have a SPD with a peak in the 400 nm region and a tail in the near UV (UVA region). UV illumination is a non-destructive examination technique that may reveal the structure of canvas and wall painting's surface layers [124]. Ultraviolet light causes fluoresce effects in the material, and this aids in identification of the compounds used. In forensic analysis is used to reveal samples of human fluids on hard surfaces or textiles [125].

The IR emitting leds are *led engin Dual Junction Infrared* with a SPD peak in the 940nm near-infrared region (NIR). Infrared photography records the variable absorption and reflectance of infrared light by an object. Infrared light penetrates deeper into canvas painting's structure than ultraviolet light [126]. Those techniques can be used together with RTI, to improve the understanding of the surface proprieties of the materials.

3.5 Free hand

(A) St. Georg Church (B) St. Parassede

FIGURE 3.14: The author of this thesis dealing with free hand RTI/PTM acquisitions in Reichenau and Rome

RTIs can be acquired also without the use of a dome or any fixed structure, using a light source and moving and directing it using one's hands [98]. The camera and the black sphere for calibrate the light source direction (see section 3.6) are mounted on two independent tripods. While doing so, it is important to move the light source on an hemisphere, so that the distance with the object is always the same. This technique can be useful when acquiring large objects, for example wall paintings or wall mosaic. This is extremely important to acquire ancient artwork that are installed in the walls and ceilings of churches, palaces, villas or museums. It would be problematic to operate in those places with complex equipment that requires too much volume, for example the BD or even a bigger set-up. The free hand technique is ideal for those delicate

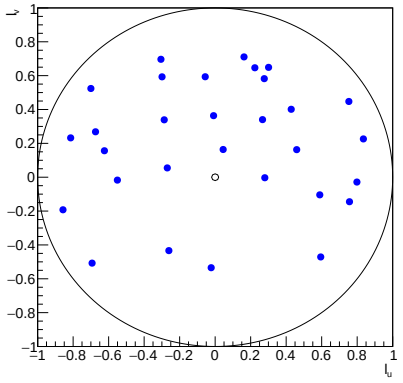

(A) Bode Museum in Berlin

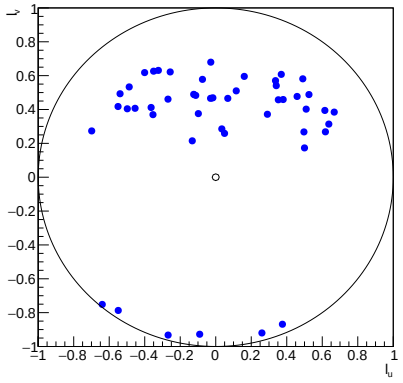

(B) St. Georg Church in Reichenau

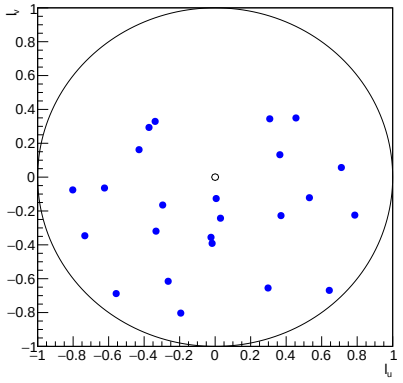

(C) Muenster in Basel

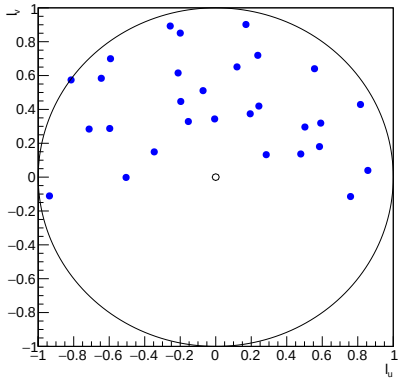

(D) Universitaet Bibliotek in Basel

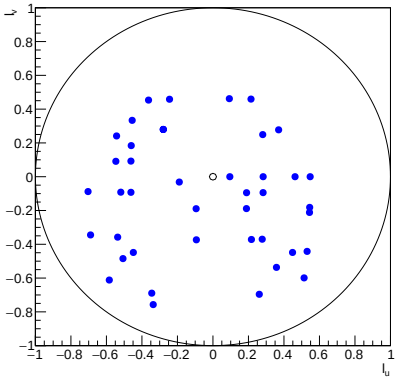

(E) Santa Parassede in Rome

FIGURE 3.15: Free hand light positions (blue dots), circumference of radius 1 and center position are also marked

settings. Figure 3.14a is a picture of a test of a wall paintings acquisition with the free hand technique. The light source is mounted on top of a 3 meters long aluminum rod. Figure 3.14b is a picture of a test of a mosaic acquisition with the free hand technique. The light source is mounted on top of a 2 meters long aluminum rod.

The major difficulty in this approach can be seen in the distribution of light sources

shown in figures 3.15a, 3.15b, 3.15c, 3.15d that shows the light sources distribution, in the l_u, l_v plane, for four different tests of the free hand (FH) technique. FH has been used in Bode Museum in Berlin 3.15a, St. Georg Church in Reichenau 3.15b, Muenster in Basel 3.15c and in the Library of the University of Basel 3.15d. Although some information extracted from the RTIs acquired with those light source distribution has been useful for art historians and restorers, it was not possible to extract more quantitative data for the first four trials. This could be explained by the not uniform and not symmetric arrangement of the lights caused by technical difficulties in moving the light. The last experiment, in Santa Parassede, was successful, see section 4.5, thanks to the favorable architecture and the experience acquired in the previous tries.

3.6 Calibration

Calibrating a data acquisition system is the only methodology that allows to assure the consistency of the results and the comparison between different acquisition or different systems. This important step is even more crucial when dealing with image processing algorithms.
The experimental set-ups presented this chapter have some characteristic in common: the image acquisition device is a photo-camera, usually a SLR camera, and a single acquisition is a set of images, each from a light source. The camera comes already calibrated from the manufacturer, but it has many free parameters that need to be adjusted manually. Camera exposure, the combination between exposure time and aperture (section 3.6.1) and color balance (section 3.6.2) need to be the consistent for each acquisition. The light sources in the each of the domes - also in the free hand technique - illuminate the subject from different light directions and may have slightly different color temperatures. These aspect are taken into account by the light direction calibration (section 3.6.3) and color balance (section 3.6.2). Finally, since different lenses can be used, to be consistent it is important to apply lens calibration (section 3.6.4).

3.6.1 Camera exposure

The term exposure in photography describes the total quantity of light energy incident on a sensitive material [127] and is given by:

$$H = Et \tag{3.1}$$

where H is the exposure, E is the image-plane illuminance (measured in lux) t is the exposure time (measured in seconds). H is inversely proportional to the area of the

aperture, usually expressed by the f-number $N = \frac{f}{D}$ where f is the focal length, and D is the diameter of the effective aperture. Therefore it is possible to write:

$$H \propto \frac{t}{N^2} \tag{3.2}$$

Several factors have to be taken into account when deciding what camera exposure is the best fitting for the purpose. It is generally complex to define a combination working for all situations. Figure 3.16 shows the same image under-exposed and over-exposed. To each example the histogram of the values of the pixels (from 0 to 255) is presented. In the case of an under exposed image the shadows lose details, and are said to be clipped. On the contrary, in the case of overexposed images, the bright points are losing details. Correctly exposing a photography means to balance the exposure so that both shadows and highlights have a consistent level of details. To have exposure tolerance it is important to select a camera with a high dynamic range. It is crucial to have a consistent exposure for all the images in a single RTI acquisition. That means that whatever adjustment has to be applied correspondingly to each image. This can happen before taking the photos or in the post-processing phase.

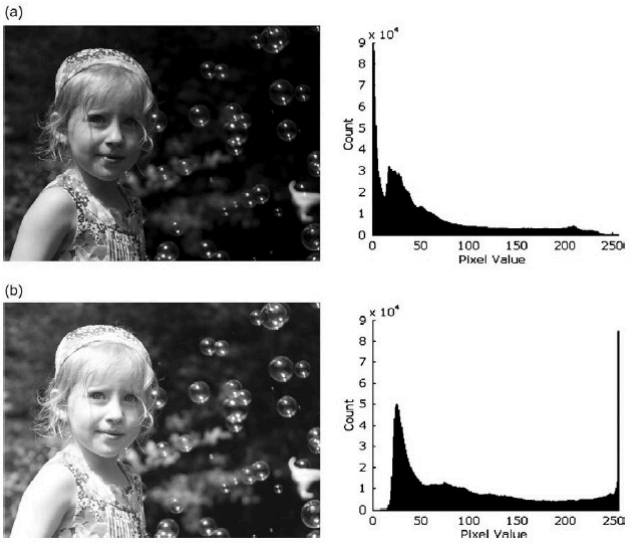

FIGURE 3.16: The effects of over-exposure (a) and under-exposure(b) on the same image. The histogram of pixel values is shown in both cases. Source in reference [127]

3.6.2 Color balance

As introduced in Section 2.2.2 color is perceived by the human visual system combining the eyes sensory response with interpretation of signals by the brain. As a result, white objects are interpreted as white under extensively varying conditions of illumination. White plays and important role: if white is perceived correctly, usually other colors

and hues are also [6]. In contrast, image sensors, whether traditional film or a modern digital camera, produce a response to illumination that depends on the parameters chosen. When shooting a digital photo it is possible to store the data collected by the sensor as raw-data, where only the physical parameters (focus, zoom and aperture) are fixed at the moment of exposure, and others (exposition, color temperature, saturation, etc...) can be decided in the post-processing phase.
The basic principle of color balance is based on the assumption to scale all relative luminance in an image so that objects which are believed to be neutral appear so [6]. To exemplify in the case of a 8 bits RGB linear space: if a surface with red channel $R = 251$ represents a white object, and if 255 is the count which corresponds to white, multiplying all red values by 255/240 leds to a color balance for red. The same procedure is then repeated with green and blue channels, each with its own value. This would result, at least in theory, in a color balanced image. In mathematical terms:

$$\begin{bmatrix} R_b \\ G_b \\ B_b \end{bmatrix} = \begin{bmatrix} 255/R_w & 0 & 0 \\ 0 & 255/G_w & 0 \\ 0 & 0 & 255/B_w \end{bmatrix} \begin{bmatrix} R \\ G \\ B \end{bmatrix} \tag{3.3}$$

where R_b, G_b, and B_b are the red, green, and blue components of a pixel in the color balanced image; R, G, and B are red, green, and blue components of the image before color balancing, and R_w, G_w, and B_w are the red, green, and blue components the reference white point pixel. This transformation matrix is the simplest possible approach in color balance, but it has been proved to be effective when used on the camera raw data [128]. Quite conveniently, cameras and software for camera image analysis offers the possibility to color balance acquired photo selecting the color temperature, thus assuming the SPD of the light source. Several categories of light sources (such as led, flash, neon or ambient) have similar SPD, that can be assumed do standard and defined by the color temperature, similarly to what happens with the black body radiation.

3.6.3 Light direction

The incoming lights direction are an important information to fit the PTM model explained in section 2.5.1. The calibration of the light sources positions can be performed in several ways:

- measuring the position of the light sources and consequently computing the normalized vector pointing to the light direction from the intersection point of the optical axis of the camera and the object. This is the most straight forward method

but it impractical considering the number of light sources involved and the different devices. Another consideration is that it should be recalculated every time the camera or the object are moved or changed.

- Placing a target object on the intersection point between the optical axis of the camera and the plane over which the dome is placed. The study of the shadows this object casts allow to reconstruct the source light directions. This technique and other coming from photometric imaging have been explored in the works in reference [129] and reference [130].
- Using a glass reflective plane and measuring the reflection of the light source. This technique has been explored in the works in reference [129] and reference [130].
- Placing a target black glossy sphere on the intersection point between the optical axis of the camera and the plane over which the dome is placed. The highlight caused by the specular refection of a specific light source is then detected and with some simple geometry consideration it is possible to reconstruct the light direction. This technique has been the first to be introduced, see reference [69].

In this work the last method has been used for several reason. Firstly it is the de-facto standard when considering RTI/PTM and it is widely accepted. Furthermore it has been shown [130] that the detection of light coordinates is affected by a numerous list of possible systematic errors. Those include:

- the not punctiform nature of the light source, in the case this is a flash light source, this effect has been reduced thanks to the introduction of LEDs light sources;
- the not perfectly hemispherical shape of the dome;
- the incorrect placement of the targed object or black glossy sphere;
- the not perfect planarity of the glass sheet.

The concluding argument regards the the nature of the RTI/PTM algorithm. Indeed it solves a over-determined system using a regression algorithm. Therefore any error in the positions of individual lamps are absorbed into the overall uncertainty [129]. This is particularly true in the case of a dome consisting of more than 30 light sources, since the free parameters of the model are only 6.

3.6.4 Lens calibration

The lenses used in this work are 60mm and 105mm Nikkor macro lenses. Despite being high quality lenses, they are affected by residual aberrations that can introduce errors

and distortion in the final images. Understanding these criticalities is useful to describe imaging limitations of camera lenses and to take them into account in the calibration procedure. An ideal lens does not introduce geometric errors in the image, but real world lenses do. This is caused, for example, since the refractive index of real materials - like glass - varies with wavelength, or by the fact that lens surfaces are usually spherical in shape and ultimately because of the intrinsically nature of light. To take into account possible lenses distortions, the constructor provides a lens profile that can be applied, using a dedicated software, to transform raw images into calibrated final files, for example TIFF. These distortions cause:

- Chromatic aberrations happens because shorter wavelengths are refracted more than longer wavelengths in the glass lenses are made of, causing spectral dispersion and dispersive power. As a result the focal length of different color lies in different points. This effect is usually taken into account by the lens profile provided by the constructor of the lens.

- Spherical aberrations are caused since refraction depends on the angles of incidence between the lens surface and the incoming light and the refractive index. Given the spherical profile of the lenses that form the objective, marginal rays come to a focus nearer to the lens than those through the central zone. The resultant lack of sharpness is called spherical aberration (SA). In a simple lens, SA is reduced by using a small aperture, In complex lenses SA is reduced by the lens profile provided by the constructor.

- Diffraction effects: closing the aperture down may seem the way to reduce residual aberrations, but this increases the effects of diffraction. At large apertures the effects of diffraction are small and negligible respect to other contributions, but as the aperture gets closer, they rise and the diffraction pattern becomes more visible. This reduces the information stored in each pixel. As a rule of thumb that resolution will be limited by diffraction if the size of a single pixel in the sensor less than twice the diameter of the Airy disk. for this reason, in a digital camera, making the pixels of the image sensor smaller than 4μm would not actually increase optical image resolution [127]. In camera settings this translate into: using a aperture smaller that 1/16 would decrease the optical image resolution [127].

Some other effects exist, but it would be too much in the context of RTI to point them out. The degrading effects usually increase with both aperture and angle of field [127]. These effects can be partially corrected by the use of modern software to convert between raw images and calibrated ones.

3.7 Software

The software needed to implement the calibration described above, to create a RTI/PTM and to display it does not exist as a single executable. Given the complexity of some steps, such as the raw data conversion that depends on parameter depending on the constructor of the camera, not freely available, it is unrealistic to develop all the needed tools in a short time. Therefore it is important assemble a work-flow using various existing software and rewriting only the critical parts.
The first step is the calibration and image elaboration. In this step already existing software is mainly used, a short list includes: CHI RTIBuilder [131] for the calibration of the lights direction based on the black sphere; camera specific proprietary software for remote capture and Adobe Raw Converter for raw image data calibration and transformation. Each image is converted from raw data to 16 bit TIF Images.
The second step is the RTI/PTM elaboration and the consequent gloss measure that is described in section 4. The prototype was developed with Matlab [132] for first experimental studies. For reasons of performance this code had to be dismissed and changed using a programming language that allowed a faster elaboration. All the computational work related to the analysis of the captured image data, consisting of the PTM fitting procedure and the gloss coefficient estimation, is based on a program written in C++ and Python, with the use of the Simplified Wrapper and Interface Generator (SWIG) library [133]. For reasons accessibility the code will be integrated in an image server compliant with the International Image Interoperability Framework (IIIF) [134]. This server, Simple Image Presentation Interface (SIPI), has been developed at the DHlab and implements a multi-threaded http(s) server written in C++ capable of converting on the fly images between various format, suc as TIF, JPEG2000, JPEG and PNG. The author of this thesis contributed to SIPI.
The third and last step consist in the visualization. Another limitation regards the virtual environment where the visualization takes place. Usually RTIs are displayed in a stand alone application, that profits from the computational power of several central processing units (CPUs) and graphics processing units (GPUs). This allows to display even complex models, so that the light direction can be changed in real time. Using a stand alone application imposes important limitations of accesibility of the content and the possibility to interact as a multi user platform. No one of the existing alternatives to RTI/PTMs, is easily integrated in a web-viewer. This obstacle limits the usability of these technologies. The most promising way to work with RTI renderings is certainly a web-environment, based on standard technology, without plug-ins or other add-ons. For all this reasons the most natural choice is to use the WebGL [4] library. WebGL (Web Graphics Library) is a JavaScript API for rendering 3D graphics within any compatible web browser. It is based on OpenGL [5] for Embedded Systems, a subset of OpenGL

computer graphics rendering application programming interface (API) for rendering 2D and 3D computer graphics. This choice allows to display the results in any browser without the need of external plug-ins. WebGl poses a limitation in the choice of the mathematical model. Since it relies on the limited resources of the browser, and given the need of having a real-time response to the light direction change, the mathematical model has to be computationally undemanding. The rendering of RTI data can either be done in any modern standard web-browser (Chrome, Safari or Firefox) with rti.js, a software written in collaboration with A.Kaiser [135]. The already existing CHI RTIViewer software [131] has also been modified to enable the display of the final result. The web version is to be preferred since it includes more features and controls, is natively multi platform and is generally faster than the old RTIViewer.

Chapter 4

eRTI and Gloss detection

4.1 Introduction

In section 2.5 the RTI technique has been introduced as a tool to reproduce material appearance, as realistically looking as possible into a virtual environment. Since this technology has been developed in 2001, its first experimentations and working examples have been in the field of artworks and archaeological objects. The material reflection proprieties of these tested items is mostly spatially homogeneous and approximable as lambertian. However, when it comes to special kinds of artworks like mosaics, the limitations of standard RTIs become evident.

The challenge concerning the digitization of mosaics lies in their complex surface properties and reflection behavior. Their specific materiality is a result of numerous tesserae that are composed in a setting bed to form the mosaic. All of these small parts reflect light in a particular way, causing an impressive sparkling effect that cannot be visualized appropriately using normal photographic images. Besides, ancient or medieval mosaics are usually placed on the walls of a church and therefore they are meant to interact with their individual surroundings by purpose. Examples are the shape of the walls as well as the lighting conditions inside such a building. Similar considerations apply for early prints, books, parchments and textiles. The visual impression that these objects convey can hardly be delivered by photographs. Metallic inclusions and the interplay of different materials give the object a dynamic appearance caused by the localized change of reflectance behavior.

The major drawback of RTI/PTM is the limitation of the applied mathematical model. A second order polynomial is able to reproduce reflection of lambertian surfaces, while the realistic reproduction of gloss is not possible. As discussed in section 2.3, lambertian surface scatters the incoming light in such a way that the apparent brightness does

not depend on the observer's point of view. A glossy surface, on the other hand, has a component of specular reflection. The limitation of the second order polynomial is crucial for the reproduction of many artworks that include glossy components like e.g. mosaics. A mosaic is constructed to interact with light and, in most cases, diffuse and glossy materials are placed on purpose to constitute the artwork in a specific manner.
In this study several objects have been captured: a leaf, a small mosaic with gold and stone tesserae, and a collection of coins among others. Figure 4.1 shows three standard photographs of those objects, that allow to have a wide set of test materials, showing a variety of glossy and matte surfaces. The small mosaic has been made by Laboratorio di Mosaico e Pintura, Domenico La Malta. The analysis performed shows that it is possible to construct a function that distinguishes the diverse grade of glossiness in a custom target. It is particularly effective when combined with conditions imposed on other variables.

(A) (B) (C)

FIGURE 4.1: The three test objects, a leaf in figure 4.1a, the mosaic in figure 4.1b and a collection of coins in figure 4.1c

4.2 Fitting methods

Each RTI acquisition consists in a set of photos, as described in section 2.5, whose number depends on the number of light sources used. As illustrated in section 3 this number, $N + 1$, can vary from the 28 flash light sources of the Big Dome (BD), to the 58 white led light sources of the FPD, to the 48 white led light sources of the BronColor Dome (BCD). Anyhow, processing the images does not depend on the device used.
After the calibration described in section 3.6 the 16bit TIF images are analyzed with a Python/C++ program (DMMaker). To better understand the mathematical terms it is convenient to introduce the $(u, v)_i^c$ notation, where i varies from 0 to N, indicating one of the images acquired by one of the domes, and c is one of the color channels, for example

R, G or B in sRGB, and (u, v) are the coordinates of a pixel. An important assumption is that each $\rho(u,v)_i^c$ pixel identifies the same area on the object. This assumption is reasonably true if there are no movements during the acquisition process and if the time of each image exposition is reasonably short, as discussed in section 3.6.
The algorithm iterates over all the pixel in the images, creating for each (u, v) an array $\mathbf{a}(u,v)^c = [\rho(u,v)_0^c, \rho(u,v)_1^c, ..., \rho(u,v)_N^c]$ of $N+1$ values between 0 and $2^{16} = 65535$. In the case of sRGB color space, this results in 3 arrays: $\mathbf{a}(u,v)^R, \mathbf{a}(u,v)^G, \mathbf{a}(u,v)^B$. Since the light illuminating the the object is white, no difference is expected in the luminance behavior for each channel. This implies that each channel can be chosen without strong preference. Anyhow, to minimize the statistical fluctuation, an average value can be calculated, resulting in a mean value channel defined as $\mathbf{m}(u,v) = \frac{\mathbf{a}(u,v)^R + \mathbf{a}(u,v)^G + \mathbf{a}(u,v)^B}{3}$.
The following step assumes that it is possible to separate the color and the luminance for each pixel, so that equation 2.33 holds. The maximum $\mathbf{a}(u,v)^R, \mathbf{a}(u,v)^G, \mathbf{a}(u,v)^B$ or $\mathbf{m}(u,v)$ value is found for all pixels under all lighting directions and the luminance for that pixel is set to 1 (65535 in 16 bits). That same scaling value is then used for the remaining pixels, so the luminance for other pixels will always be less than 1. This defines what are the light independent RGB values for each set (u, v) coordinates and what is called luminance value $L(u,v)_i$.
Equation 2.34 relates the luminance value with the coordinates (l_{ui}, l_{vi}) of the i light source thought a bivariate quadratic function, whose parameter p_j, where $j = 0, .., 5$, can be determined using the overdetermined linear system in equation 4.1:

$$\begin{cases} l_{u0}^2 p_0 + l_{v0}^2 p_1 + l_{u0} l_{v0} p_2 + l_{u0} p_3 + l_{v0} p_4 + p_5 = L_0 \\ l_{u1}^2 p_0 + l_{v1}^2 p_1 + l_{u1} l_{v1} p_2 + l_{u1} p_3 + l_{v1} p_4 + p_5 = L_1 \\ \vdots \\ l_{uN}^2 p_0 + l_{vN}^2 p_1 + l_{uN} l_{vN} p_2 + l_{uN} p_3 + l_{vN} p_4 + p_5 = L_N \end{cases} \tag{4.1}$$

The system of equations 4.1 can be written in matricial form as $Ax = b$, where A is a $(N+1) \times 6$ matrix, x and b are 6 components column vectors:

$$A = \begin{bmatrix} l_{u0}^2 & l_{v0}^2 & l_{u0} l_{v0} & l_{u0} & l_{v0} & 1 \\ l_{u1}^2 & l_{v1}^2 & l_{u1} l_{v1} & l_{u1} & l_{v1} & 1 \\ \vdots & \vdots & \vdots & \vdots & \vdots & \vdots \\ l_{uN}^2 & l_{vN}^2 & l_{uN} l_{vN} & l_{uN} & l_{vN} & 1 \end{bmatrix} \quad x = \begin{bmatrix} p_0 \\ p_1 \\ \vdots \\ p_5 \end{bmatrix} \quad b = \begin{bmatrix} L_0 \\ L_1 \\ \vdots \\ L_N \end{bmatrix} \tag{4.2}$$

An overdetermined system of equations has no unique solution. In this case, it is possible to search for the vector x which is closest to being a solution, in the sense that the difference $Ax - b$ is as small as possible. If the the Euclidean norm, $\|\mathbf{Ax} - \mathbf{b}\|^2$, is chosen, its minimum is the Least Squares Solution [136].

Different algorithms for solving a Least Squares Problem exist, the focus in this work has been to use numerically stable and computationally efficient methods. A clear advantage of using the least squares approach is that there is always a solution [136]. Another advantage is that it can be solved using a Linear least squares technique, since the problem is expressed linearly in terms of the unknown parameters of the model. The algorithms used are: normal equation method using Cholesky Factorization (NECF), singular value decomposition using the Jacobi algorithm (JacobiSVD), QR Factorization (QR) and a robust method, the Least Trimmed Squares regression (LTS).

- The JacobiSVD algorithm is implemented in the Eigen::JacobiSVD [137] class. It uses the results of the singular value decomposition theorem, which ensures that the matrix A can be written as

$$A = USV^* \tag{4.3}$$

  where U is a $n \times n$ unitary, V is a $p \times p$ unitary, and S is a n-by-p real positive matrix which is zero outside of its main diagonal; the diagonal entries of S are known as the singular values of A and the columns of U and V are known as the left and right singular vectors of A respectively. It can be shown that the solution to the least square problem is the right-singular vector of A corresponding to the smallest singular value. To compute the SVD the Jacobi algorithm [138] is used.

- The NECF algorithm is implemented by the class TLinearFitter of ROOT [81]. It can be proved that $\hat{x}$ is a solution of the system $A\hat{x} = b$ if and only if it is a solution of the associated normal system $A^T A\hat{x} = A^T b$. The normal equation method computes the solution to the Leas Squares Problem by transforming the rectangular matrix A into triangular form, applying the Cholensky Factorization [136] on the square matrix $A^T A$

- The QR algorithm is implemented in the Eigen::FullPivHouseholderQR Guennebaud et al. [137] class. It is based on the QR decomposition of the matrix A into a product $A = QR$ of an orthogonal matrix Q and an upper triangular matrix R. It can be proved that a least square solution of the problem $Ax = b$ can be obtained solving the problem $Rx = Q^t b$ [136].

- The LTS algorithm is implemented by the method TLinearFitter::EvalRobust() of ROOT [81]. This algorithm is the only one, among those tested, that explicitly takes into account the possible presence of outliers. An outlier is a point that does not follow the linear pattern of the majority of the data [139]. Several methods for linear regression in presence of outliers have been proposed; they are also defined as robust regressions algorithms. Arguably the most known are Least Median

of Squares [80] and its improvement LTS [140]. The LTS method attempts to minimize the sum of squared residuals over a subset of the total set of points. This method is specifically designed to be efficient on large data sets (number of points greater than 500) but it is also effective on smaller sets.

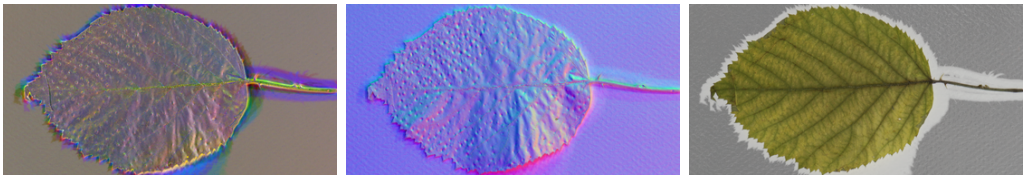

(A) p_0, p_1, p_2 (B) p_3, p_4, p_5 (C) r, g, b

FIGURE 4.2: Result of NECF algorithm applied on the leaf in figure 4.1a. The p_i^{raw} and the RGB coefficients are calculated and stored as 16-BIT, opportunely rescaled to the range $[0, 65535]$

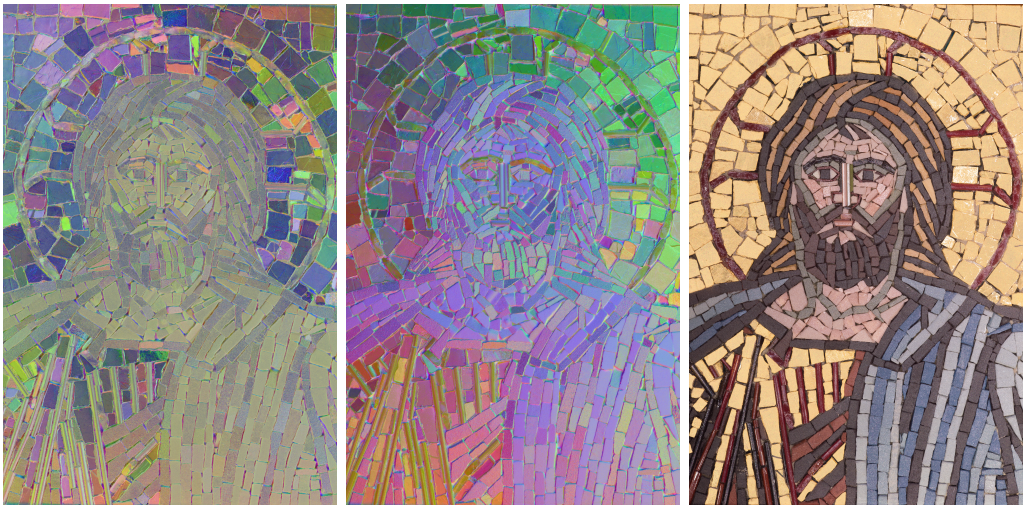

(A) p_0, p_1, p_2 (B) p_3, p_4, p_5 (C) r, g, b

FIGURE 4.3: Result of NECF algorithm applied on the mosaic in figure 4.1b. The p_i^{raw} and the RGB coefficients are calculated and stored as 16-BIT, opportunely rescaled to the range $[0, 65535]$

(A) p_0, p_1, p_2 (B) p_3, p_4, p_5 (C) r, g, b

FIGURE 4.4: Result of NECF algorithm applied on the collection of coins in figure 4.1c. The p_i^{raw} and the RGB coefficients are calculated and stored as 16-BIT values, opportunely rescaled to the range $[0, 65535]$

Figures 4.2, 4.3 and 4.4 show the result of the NECF algorithm applied on the test objects. The p_i^{raw} coefficients calculated are stored as 16-BIT values, opportunely rescaled

to the range $[0, 65535]$ using two additional parameters for each p_i, a scale and a bias. The rescaled coefficient are $p_i = (p_i^{\text{raw}} - b) \cdot s$. Therefore it is possible to re-convert the six p_i^{raw} coefficients storing 12 parameters: 6 for the scale and 6 for the bias.
The 16-bit p_i parameters can be conveniently stored and displayed in a 16-bit TIF file, each as a color channel of the sRGB color space. Figure 4.2a shows the parameter p_0 stored in the R channel, p_1 in the G channel and p_2 in the B channel for the leaf in figure 4.1a. Figure 4.2b shows the parameters p_3, p_4 and p_5 stored as RGB. Lastly, figure 4.2c shows the RGB colors independent of the light direction.
Figure 4.3 and 4.4 show the same informations for the other two test objects.

4.3 Variables to represent gloss

As discussed in section 2.5 the standard RTI method gives satisfactory results when the object displays a uniform lambertian behavior. To extend RTI to diverse types of surfaces a new approach, presented in reference [141], has been followed, avoiding to find a new complex mathematical model to reproduce matte and glossy surface. Before entering the detailed discussion, it is convenient to understand how the PTM fit works on different level of "glossiness". Figure 4.5a shows the RTI-fit of a pixel on a lambertiant material tessera from the mosaic in figure 4.1b. The black dots represent the 48 L_i

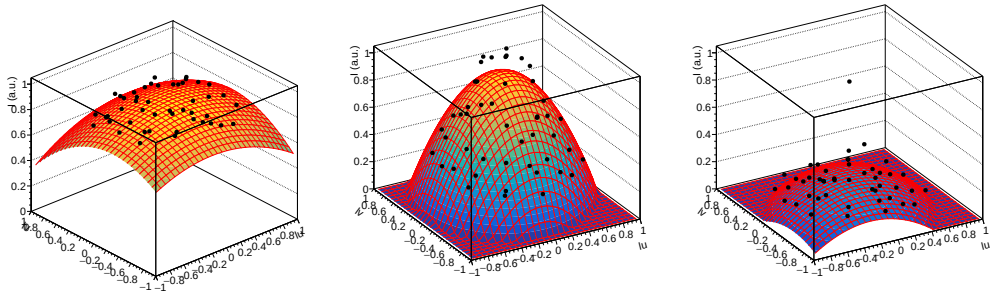

(A) Matte material (B) Glossy material, gold tessera (C) Highly glossy material, eybrows

FIGURE 4.5: Example of three different RTI/PTM fitting for three different areas of the mosaic in figure 4.1b

values, one for each light source, disposed according to their position in the l_u, l_v plane, the z-axis is in arbitrary units for convenience. The surface displayed is the result of the NECF algorithm applied on the standard RTI/PTM function. Figure 4.5b shows the same point distribution for a glossy pixel on one of the gold tessere. It can be noticed the group of points that does not belong to the lambertiant component. Those point deviate accordingly to the amount of "glossiness", as can be seen by looking at figure 4.5c that represent the point distribution and the RTI-fit for a pixel of highly

glossy materials in the eyebrows of the figure in the mosaic. Therefore it is important to find a variable that can express this amount of "glossiness" in mathematical term. To perform this function, a new type of RTI has been introduced: the enhanced RTI (eRTI). This new technique allows to visualize various types of materials, with different reflection proprieties. To achieve this result a layering approach - illustrated in figure 4.6 has been used (patent pending). Each layer represent a different information about the surface: for each (u, v) coordinates, the RGB layer is determined by the color detected, the PTM - Lambertian value is determined by the 6 $p_i(u, v)$ coefficient ant the glossy coefficient is calculated using the procedure described following in the text. The layering

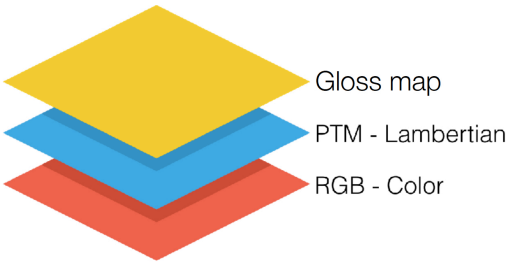

FIGURE 4.6: The layering model

approach is particularly useful when using computer graphics for displaying the results. As discussed in section 2.4 the visual appearance of a realistic surface is composed in a several stages process. The eRTI algorithm consists of the following steps:

- the diffuse component is calculated by a mathematical function (second order polynomial) and the coefficients found to describe the diffuse reflection,
- the RGB values are calculated and stored using sRGB values extracted from the image with the maximum value of $L(u, v)$,
- the glossy component is generated synthetically by overlay of a reflection model derived from computer graphics. If the gloss coefficient $G(x, y)$ is > 0, such virtual specularity is added based on e.g. the Phong reflection model [40], described in section 2.4. The parameters of this model can be changed, within a range, by the user and based on the physics of the material of the original.

To calculate the glossy coefficient,the distance between the matte function value and the intensity of each (u, v) coordinate is computed for all lighting directions. For this purpose two different functions $G_2(u, v)$ and $G_3(u, v)$ have been defined:

$$G_2(x, y) = \frac{1}{N} \sum_{(l_u, l_v)} \left(f_{matte}(l_u, l_v, u, v) - L((l_u, l_v), u, v) \right)^2 , \tag{4.4}$$

and

$$G_3(u,v) = \frac{1}{M} \sum_{(l_u,l_v)} \left| f_{matte}(l_u, l_v, u, v) - L((l_u, l_v), u, v) \right|^3, \tag{4.5}$$

where N and M are normalization factors and $L((l_u, l_v), x, y)$ is the luminance value for the light source identified with the coordinates l_u, l_v and f_{matte} is the standard PTM equation 2.34

It has to be noticed that a criticality is present in the second step of the eRTI approach, the extraction of the RGB values. As discussed in section 2.3 the color obtained in this way is consistent only for lambertian surfaces. For glossy or specular surfaces, the maximum value of $L(u, v)$ is caused by the specular reflection, which color is the same of the light source, in most cases, white. To overcome this problem, if glossy is detected in position (u, v), the RGB values are calculated using sRGB values coming from the image with value of $L(u, v) = \gamma \max_{(l_u,l_v)} (L(u, v))$, where γ has a value between 0 and 1, typically 0.7.

As the p_i parameters, also the glossy coefficients are efficiently stored using a bias and a scale coefficient and converted to 16-bit. Figure 4.7a shows the distribution of $G_2(x, y)$

(A) $G_2(x, y)$ (B) $G_3(x, y)$

FIGURE 4.7: $G_2(x, y)$ and $G_3(x, y)$ distribution for the collection of coins. Black values correspond to 0 and white correspond to the maximum value that the glossy coefficient assumes. The coefficients are stored as 16-BIT values, opportunely rescaled to the range $[0, 65535]$

for the coins test in figure 4.1c, and figure 4.7b shows the distribution of the coefficient $G_3(x, y)$ for the same test objects. In those images 0 correspond to 0 and 1 correspond to the maximum value that the glossy coefficient assumes. In figure 4.8a and figure 4.8b shows the same distributions for the mosaic test. It can be seen that different levels of gloss are identified, that belong to different materials. To obtain these images the cuts described in section 4.4 have been already applied.

(A) $G_2(x, y)$ (B) $G_3(x, y)$

FIGURE 4.8: $G_2(x, y)$ and $G_3(x, y)$ distribution for the mosaic. Black values correspond to 0 and white correspond to the maximum value that the glossy coefficient assumes. The coefficients are stored as 16-BIT values, opportunely rescaled to the range $[0, 65535]$

4.4 Cuts

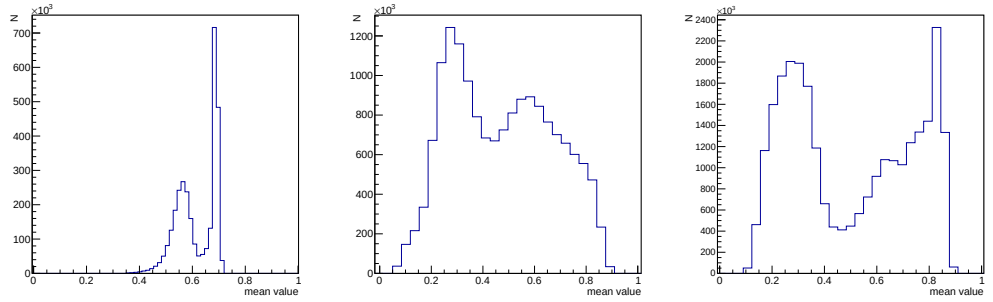

(A) leaf (B) mosaic (C) coins

FIGURE 4.9: Histogram of the mean value of the luminance for the three test objects in figure 4.1

Several important information about the nature of the materiality of specific pixels can be extracted from the mean value of the intensity. This quantity represent the mean value (MV) of the luminance averaged over the different light directions and it has been defined as:

$$\mathrm{MV}(x, y) = \frac{1}{N_p} \sum_{(l_u, l_v)} I((l_u, l_v), x, y) \tag{4.6}$$

where N_p is a normalization factor. Figure 4.9 shows the distribution of the MV for the three test objects. It is immediate to recognize that a component structure exists. Each histogram shows several different peaks that are associated to different classes of materials. To understand the nature of these peaks a threshold analysis has been performed.

4.4.1 Thresholds on mean value

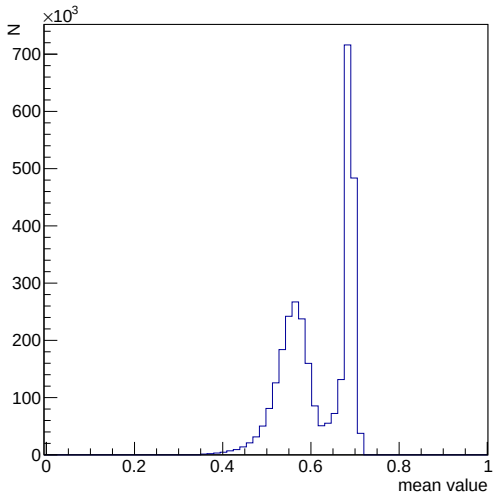

FIGURE 4.10: Histogram of the mean value of the luminance for the leaf in figure in figure 4.1a

Figure 4.1a shows a more detailed version of histogram in figure 4.9a. It is convenient to divide the histogram in two regions defined by a range in mean value and assign the value 1 (white) to every pixel that has mean value in the range, and 0 if not. This results in:

- all the pixels with $0 < \text{MV} < 0.63$ are white in figure 4.11a;
- all the pixels with $0.63 < \text{MV} < 1$ are white in figure 4.11b.

Comparing this result with one of the starting pictures, see figure 4.1a, give a clear evidence of the possibility to differentiate between different classes of reflectance behavior. It is maybe even more evident if the same technique is applied to the mosaic in figure 4.1b. The histogram in figure 4.12 shows the distribution of the mean value. It is possible to distinguish at least three different ranges:

- all the pixels with $0 < \text{MV} < 0.15$ are white in figure 4.13a;
- all the pixels with $0.15 < \text{MV} < 0.44$ are white in figure 4.13b;

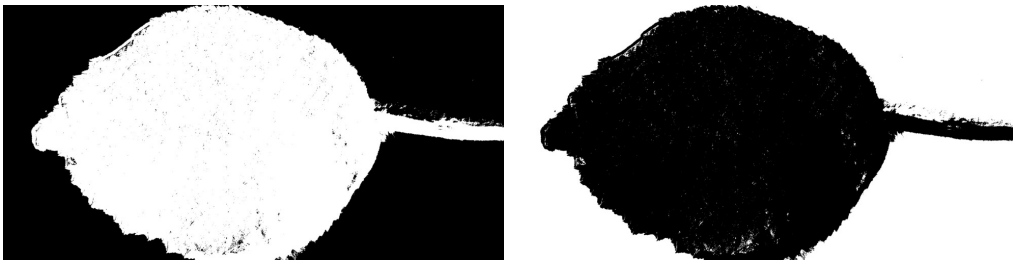

(A) $0 < MV < 0.63$ (B) $0.63 < MV < 1$

FIGURE 4.11: MV threshold analysis for the leaf: the value 1 (white) has been assigned to every pixel that has mean value in the range, and 0 (black) if not.

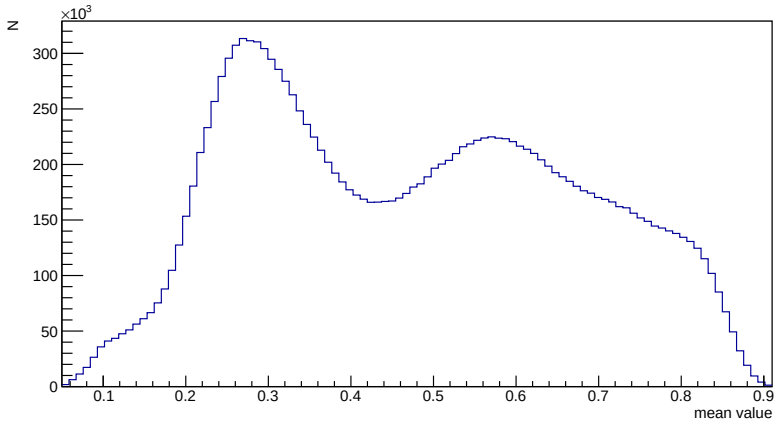

FIGURE 4.12: histogram of the mean value of the luminance for the mosaic in figure in figure 4.1b

- all the pixels with $0.44 < MV < 1$ are white in figure 4.13c.

In the case of the mosaic it is possible to distinguish three different materiality behaviors:

- Highly glossy tessere: they mainly compose the aureola of Christ and the eyebrows, plus some extra features on the dress;
- Golden tessere: they compose all the background and part of the dress;
- Matte tessere: they compose the skin of the figure and the blue and black parts of the dress.

Figure 4.14 shows the histogram of the mean value for the collection of coins in figure 4.1c. It is possible to distinguish at least four different ranges:

- all the pixels with $0 < MV < 0.45$ are white in figure 4.15a;
- all the pixels with $0.45 < MV < 0.69$ are white in figure 4.15b;

(A) $0 < MV < 0.44$ (B) $0.15 < MV < 0.44$ (C) $0.45 < MV < 1$

FIGURE 4.13: MV threshold analysis for the mosaic: the value 1 (white) has been assigned to every pixel that has mean value in the range, and 0 (black) if not.

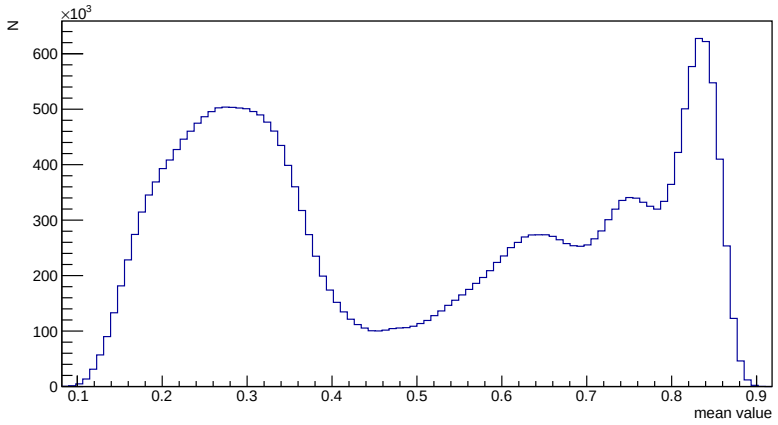

FIGURE 4.14: histogram of the mean value of the luminance for the coins in figure in figure 4.1c

- all the pixels with $0.69 < MV < 0.78$ are white in figure 4.15c;
- all the pixels with $0.78 < MV < 1$ are white in figure 4.15c;

in this case it is possible to distinguish two macro-areas:

- the coins, made of metal, are highlighted in figure 4.15a;
- the background, made of white paper, is divided in the three other ranges.

It is important to notice that those results are independent of the dome or the light sources distribution used. The possibility to distinguish between materials using the mean value of the intensity has an important application: it allows to apply the gloss coefficient only to certain areas improving the effectiveness of the visual result.

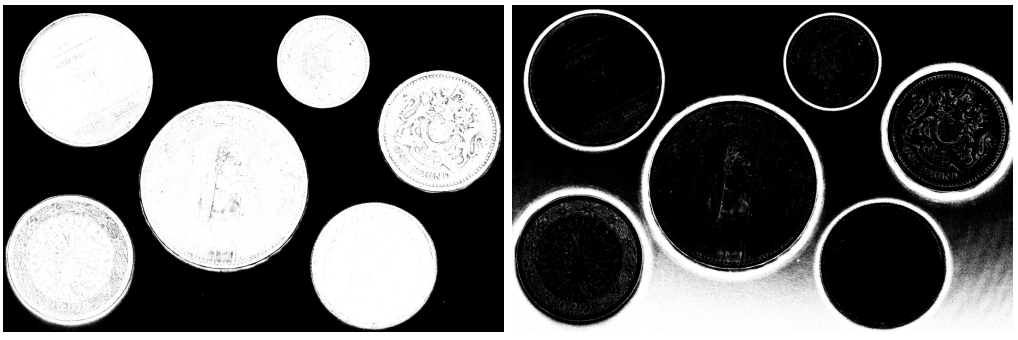

(A) $0 < \text{MV} < 0.45$ (B) $0.45 < \text{MV} < 0.69$

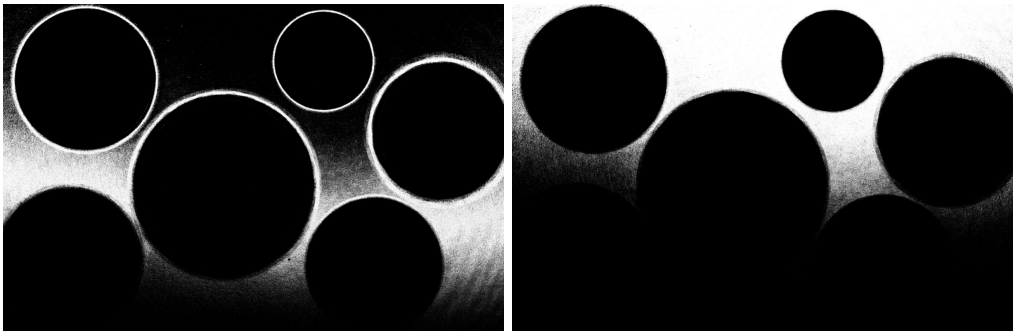

(C) $0.69 < \text{MV} < 0.78$ (D) $0.78 < \text{MV} < 1$

FIGURE 4.15: MV threshold analysis for the collection of coins: the value 1 (white) has been assigned to every pixel that has mean value in the range, and 0 (black) if not.

4.4.2 Luminance variance

Other statistics of the images have been tested, for example the variance of the intensity:

$$\text{variance}(x,y) = \frac{1}{N_p} \sum_{(l_u,l_v)} \left(I((l_u,l_v),x,y) - \text{meanvalue}(x,y)\right)^2 \tag{4.7}$$

where N_p is a normalization factor. Since the variance does not provide additional information at the MV, the histogram of the distribution of the variance is presented only for the collection of coins, see Figure 4.16a. It is possible to distinguish two components

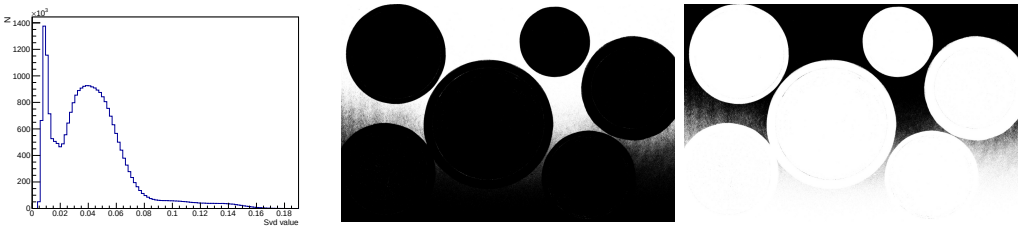

(A) histogram (B) $0 < \text{variance} < 0.02$ (C) $0.02 < \text{meanvalue} < 1$

FIGURE 4.16: histogram and threshold analysis for the variance of the collection of coins: the value 1 (white) has been assigned to every pixel that has mean value in the range, and 0 (black) if not.

also in this graph, although it is not clear what kind of information is provided by the variance. The same methodology has been applied, as in the case of the MV :

- all the pixels with $0 <$ variance < 0.02 are white in figure 4.16b;
- all the pixels with $0.02 <$ variance < 1 are white in figure 4.16c.

This can be expected since the variance is not, by definition, independent from the mean value.

4.5 Santa Parassede results

It is worth to spend a specific section of this thesis to present the results obtained in the Basilica di Santa Parassede in Rome. In June 2017 Several acquisition of the mosaic in the San Zeno chapel were made. The free hand technique for positioning the light sources has been used, as described in section 3.5. Another difference is that the mosaic on the San Zeno ceiling is 6 meters above the ground and measures approximately 3.5 meters x 3.5 meters.
The results confirm what has been presented for the small mosaic, also on a big wall mosaic. figure 4.17a a standard photography of a detail of the ceiling is presented, where the figure of Christ is surrounded by four angels In figure 4.17b a cut on the mean value of the luminance has been applied: all the pixels with $0.0 <$ MV < 0.45 are black and all the pixels with MV > 0.45 are white. It can be noticed that the figure of Christ -

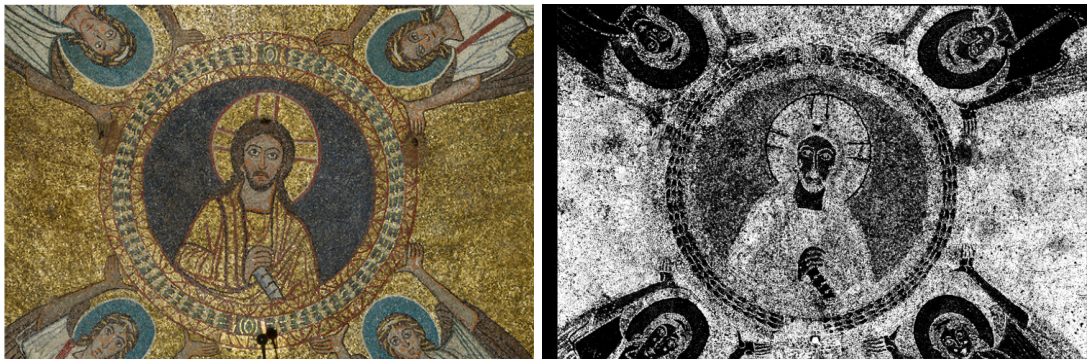

(A) Normal photo (B) $0.0 <$ meanvalue < 0.45

FIGURE 4.17: comparison between a photo from a single light direction and MV threshold analysis for the mosaic in Santa Parassede: the value 1 (white) has been assigned to every pixel that has mean value in the range, and 0 (black) if not. The reproduced mosaic belongs to the patrimony of the *Fondo Edifici di Culto*, administrated by the *Direzione Centrale per lAmministrazione* of the *Fondo Edifici di Culto del Ministero dellInterno*

the most important in this ensemble - has much more gloss (white) than the four angles

at the edges of the picture.
In figure 4.18a the $G_2(x, y)$ gloss variable is presented, while in figure 4.18b is presented the gloss variable $G_3(x, y)$. Both variables show another characteristic of the mosaic that is easily noticed by the human eye: the difference in gloss intensity between the blue stones - made of glass - and the golden tesserea.

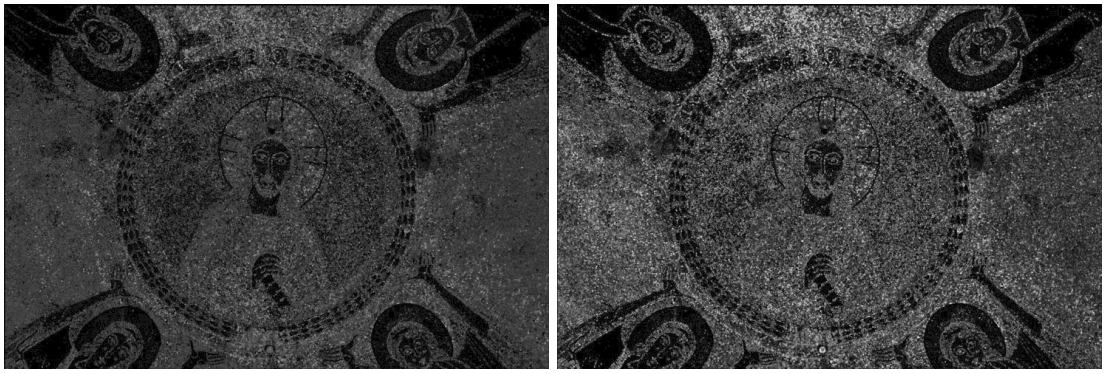

(A) $G_2(x, y)$ (B) $G_3(x, y)$

FIGURE 4.18: $G_2(x, y)$ and $G_3(x, y)$ distribution for the mosaic in Santa Parassede. Black values correspond to 0 and white correspond to the maximum value that the glossy coefficient assumes. The coefficients are stored as 16-BIT values, opportunely rescaled to the range $[0, 65535]$

4.6 Rendering

Once all 6+3+1 coefficients - $p_i(u, v)$, $\mathrm{RGB}(u, v)$, $G_{2\,\mathrm{or}\,3}(u, v)$ - are computed, it is possible to render each pixel (u, v) rewriting equation 2.30 into:

$$\begin{bmatrix} \mathrm{R} \\ \mathrm{G} \\ \mathrm{B} \end{bmatrix} (u, v) = \{k_\mathrm{a} L_\mathrm{a}(u, v) + f_\mathrm{matte} \left[k_\mathrm{d}(\mathbf{N} \cdot \mathbf{S}) + G_{2\,\mathrm{or}\,3}(u, v) k_\mathrm{s} F_s(\mathbf{S}, \mathbf{V})\right]\} \begin{bmatrix} \mathrm{R} \\ \mathrm{G} \\ \mathrm{B} \end{bmatrix} (u, v) \tag{4.8}$$

where $F_s(\mathbf{S}, \mathbf{V})$ is the specular shading function and is generally regulated by a α shininess constant, which is larger for surfaces that are smoother and more mirror-like since, when this constant is large the specular highlight is small; k_d which is a diffuse reflection constant, and k_s which is a specular reflection constant; $\mathbf{N}$ is the normal to the surface, that can be calculated from RTI/PTM coefficients, as illustrated in section 2.5.1; $\mathbf{S}$ and $\mathbf{V}$ are the source light direction and the viewing direction vectors; k_a is the ambient light color constant; $G_{2\,\mathrm{or}\,3}(u, v)$ is the gloss coefficient defined in section 4.3.

The strength of RTI is the possibility, for the user, to interactively change the light direction. This interaction is important in order to perceive the quality of a glossy surface. Therefore a set of tools for rendering and interacting with RTI/PTM data in a web

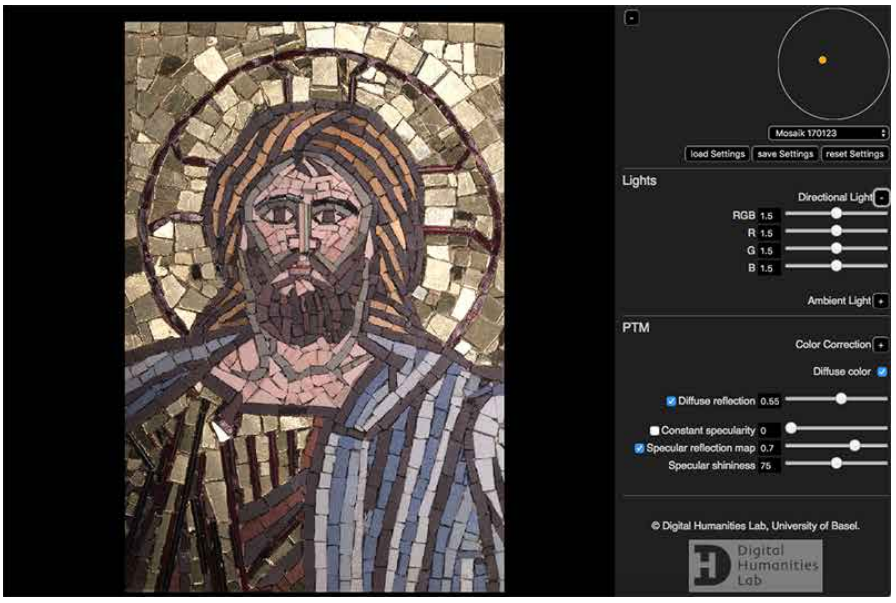

FIGURE 4.19: rti.js Viewer. A Javascript libraray that allows to visualize eRTI and to change the rendering parameters and the light direction. In this screenshot the mosaic is presented. Github repository in reference [135].

browser[135] has been developed and it is shown in figure 4.19. The javascript library and the viewers are IIIF compliant, three.js-based and supporting multi-resolution. Three.js is a JavaScript computer graphics library for web platforms. It uses WebGL [4] (Web Graphics Library) for real time rendering. WebGL is a 3D computer graphics and 2D graphics JavaScript API (application program interface), compatible with a variety of web browsers without the use of plug-ins. WebGL allows GPU (graphics processing unit) accelerated image processing and 3D effects as part of the web page canvas. Therefore, it is possible to interact with other HTML elements or other parts of the page. Inspiration has been taken from the existing RTI Viewer [70], a C++/QT software released in General Public License version 3, and the existing WebRTI Viewer, a web application written mainly in JavaScript.
The viewer implements controls that allow the user to change the magnitude of the specular and diffuse part of the digital representation. These are updated in our viewer and allow the user to modify the typical parameters

4.7 Applications

Images play a vital part in terms of communication and documentation in several different fields of human activity. A list of fields includes, but it is not limited to: art historical research, restoration, cultural heritage presentation, and many other. Reproductions of objects enables the users to show specific qualities, describe the object under different view points, develop theories, discuss them with other users, and also to document the

current state of an object. This is particularly useful, if the object is not easily accessible, for example because it is kept in a museum or archive in a far away country and also if collaborating researchers work in different places. In this case the solution is to work with photographs. They document the visual impression of objects and they are a precise tool to capture the state of an original for example before and after a restoration. This has become even simpler with digital photography, because digital images can be easily shared, disseminated and given access to. Due to all of these advantages digital images are an important part not only of art historical research, but of our cultural heritage in general, and they account for a constitutive part of our contemporary multimedia output in social, scientific and economic fields.
RTIs and eRTI represent an improvement from digital images, since it gives the users the possibility, to interactively change the light direction. This interaction is important to perceive the material qualities of a surface.

4.7.1 Cultural heritage presentation and restoration

An important area of application for eRTI technology is the presentation of delicate or hard to access artworks and historic goods in public institutions like museums or archives. This would allow the exhibition of pieces which cannot be shown directly to the public for fear of damage or degradation, while still allowing a much more hands-on experience to the audience compared to exhibiting a simple place-holder photograph.
It would also allow the institutions to expand their exhibition space from their actual rooms into the world wide web, thereby also expanding their potential audience.
Several institution around the world are already starting this process of digitalization using standard RTIs. For example the National Gallery in London [94], the Coin Collection of Palazzo Blu in Pisa [142], the collection of manuscripts of Lichfield Cathedra at St Chad Gospels [143] and many other more. Related to the presentation of artworks and historic goods to a public audience, eRTI technology can be used for research work in fields like history of art, archeology or cultural heritage preservation.
It enables remote and collaborative work on the same resources, which are often hard to access, while still providing a level of detail and inspection which can not be matched by a simple photograph. With the capabilities of eRTI it is also possible to document the state of an artwork for example before and after a restoration. Due to the fact, that the measurement process is highly reproducible, eRTI can be use as a tool for documentation of any process of work on an object. eRTI can be easily integrated with other existing techologies, like UV and IR photography or 3d scanning.

4.7.2 Research

A web-based approach opens many new possibilities, for example the dissemination of digital reproductions and the collaborative work between researchers. A specific binary executable stand-alone application is limiting any scientific discussion to a workstation. The required software infrastructure to support such collaborative work goes beyond a standard web-server solution. Besides Regions of Interest (ROIs) and linked comments and annotations the full set of viewing parameters must be stored as technical metadata within the system. Furthermore any time dependent changes of those viewing parameters must be tracked for reproducibility and traceability as a reference for any future discussion. Such traceability is also necessary to be able to cite a specific situation a scholar wanted to highlight. Therefore, WebGL is the key to integrate RTI in a fully featured web-based Virtual Research Environment.
In this regard the DHLab has been developing KNORA (Knowledge Organization, Representation and Annotation) [144] and SALSAH (System for Annotation and Linkage of Sources in Arts and Humanities) [145]. Knora is a software framework for storing, sharing, and working with primary sources and data in the humanities. SALSAH is the graphical user interface, currently the version 2 is under active development.

Chapter 5

Results and discussion

5.1 Introduction

This chapter presents and discusses the results obtained during the course of the project. As discussed in chapter 2 the quantitative validation of proprieties that are perceived by the human eye is a complex task. While it is, in principle, possible to measure the difference in color - given a well-suited color space - no standard technique exists to measure the difference in other perceived qualities. For example, there exists no standard distance to measure difference in gloss between rendered surfaces [50]. This is further complicated by the need of eRTI to be a useful tool for art historian - and more generally humanity scholars.
To overcome these intrinsic difficulties a two-way approach has been developed and a workflow diagram has been implemented to narrow the gap between the scientific and the humanities approaches. This chapter is divided in two parts: section 5.2 describes how the interaction with art-historian has been conducted, and section 5.3 presents the results obtained using a more traditional numerical approach.

5.2 Art historian validation

It is important to restate that the RTI/PTM technique was originally developed as a tool for humanities scholars and cultural heritage experts. Its main goal was to provide an easily usable system for acquisition and display of cultural heritage objects. For art historians who study mosaics or any other object of complex surface composition it has always been difficult to capture and use photographic material that is capable to reproduce the actual visual impression these works of art convey when we look at them. There are two main reasons for this: on the one hand the specific materiality

of, for example, the mosaics themselves, and on the other hand the fact that they are usually placed on the walls of a church and therefore interact with those individual surroundings, for example, the shape of the walls as well as the lighting conditions inside the building. In addition, static, two-dimensional photographs cannot visualize appropriately the sparkling effect, which is caused by the surface properties of the countless light reflecting tesserae.
Similar considerations apply for early printed images, books and manuscripts. The visual impression that these objects convey is hardly delivered by a photograph. Metallic inclusions give the artwork a dynamic appearance caused by the change of reflectance behavior of glossy material compared to matte material.
As in most multidisciplinary studies, the first difficulty to be overcome was the linguistic barriers of communication. The problem was not the language, since all participants involved were proficient English speakers, but the different methodologies and practices that art-historians and scientists use. From a natural scientific perspective it is important to consider that in the humanities the principle of falsification is not the only way to solve conflicts between different hypotheses. Among the community of art-historians a central role is played by discussions between experts, that can lead to a consensus on a specific matter.

Figure 5.1 shows a diagrammatic representation of the process used to discuss the results with art-historians. Starting from a specific object or material, the first step is the data acquisition under controlled conditions. Verifying the consistency and stability of the system (the dome and the object) has a positive side effect: it allows to introduce at each iteration new improvements on the system. The progress in the domes has been described in chapter 3. Using the data acquired an eRTI is generated and its quality is tested using a qualitative comparison method. The art historian can change all the free parameters using a GUI (graphical user interface) in the DMViewer described in section 4.6. This affects the gloss appearance and triggers a discussion on the specific object. The user can select the gloss model, $G_{2\,\mathrm{or}\,3}$, and the value of the constants $k_\mathrm{s}, k_\mathrm{d}, k_\mathrm{a}$ and α within a range. With the help of a circular control, the user can select the lighting direction, or, if the viewer is used on a device that supports it, tilting the device changes the light direction. This is possible using the signals generated by the accelerometers embedded in the device. The data acquired are also processed using Matlab to perform the numerical analysis described in 5.3.
The results of the two branches of analysis are kept as independent as possible and are used to trigger a discussion. The outcome of the debate can go in the direction of improving the mathematical model of gloss, or the fitting procedure. In the latter case the data are not acquired again, but a new eRTI is generated with the new requirements and the loop can restart. The other possible outcome of the process is to keep the mathematical model but to restart the acquisition procedure, changing the initial condition

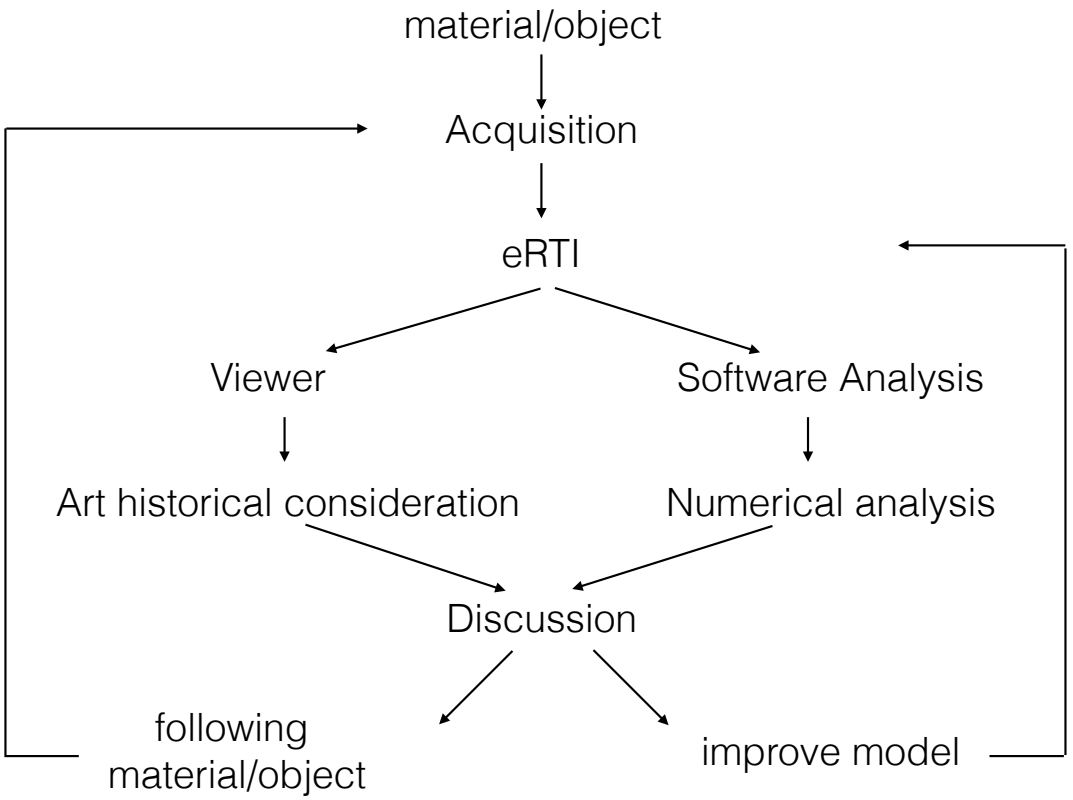

FIGURE 5.1: Schematic representation of the workflow developed to help the interaction with art-historian.

or the material or object.

In table 5.2 a summary of art-historians consideration regarding the preferred set of parameters to visualize eRTI for the mosaic, the coin collection and the leaf.

Object	k_d	k_s	$G_{2\,\mathrm{or}\,3}$	α	Comments
Leafs	min 0.8 max 1.5	0	none	none	no gloss
Mosaic	min 0.8 max 1.5	min 0.65 max 0.9	G_2	min 75 max 100	best fitting method ROOT or QR
Coins	min 0.8 max 1.5	min 0.7 max 0.9	G_2	min 75 max 100	best fitting method ROOT or QR

Looking at table 5.2 it can be seen that there was not a consensus on a singular value of the constants k_s, k_d, α. The preferences of the users are better described by a range for the value of those parameters. A similar consideration can be done on the preferred fitting method, since the users couldn't say if the NECF algorithm (ROOT) or the QR algorithm (QR) were giving better results. Instead, it was immediately evident that the G_2 function better describes the degree of glossiness of the surface.
A further consideration regarding the gloss model: art historical interest is more oriented towards the possibility of distinguishing between different appearances of materials, than an exact measurement of the reflectance proprieties. To exemplify this concept it is useful to think about the mosaic. The gold tesserae have a different reflection behavior than the matte tesserae, because they have a stronger specular component. To visualize the appearance of a whole mosaic it is important to assign different gloss components to each tessera. From the perspective of an art historian this is more important than the fidelity of the reflectance model

5.3 Measure the quality

One of the major issues encountered during this research project is surely how to measure the quality of an eRTI. Comparing RTI/PTM with eRTI is straightforward for the human eye and brain. Indeed, when the same glossy object is visualized with RTI/PTM it appears less realistic and with less dynamics than with eRTI. This difference is evident when the light direction is moved from one direction to another. It seems that our brain recognizes gloss more easily when the light direction is changing. Several attempts to assign a metric in perceived gloss has been done, see for example reference [54] and [146] but there is no standard way to measure the difference of gloss of two rendered objects. The approach followed to overcome this problem is to take and adapt the very well known Mean Squared Error (MSE). MSE is widely used [147] in the image processing community as a quantitative performance metric. The MSE of two images, $I(u,v)^c$ and $J(u,v)^c$ where c are the color channels, for example R, G or B in sRGB, and (u,v) are the pixel coordinates is calculated as:

$$\mathrm{MSE}(I,J) = \frac{1}{N_c * N_p} \sum_c \sum_{(u,v)} (I(u,v)^c - J(u,v)^c)^2 \tag{5.1}$$

where N_c is the number of color channel (usually 3) and N_p is the number of pixels. Starting from equation 5.1 it is possible to define the $\mathrm{MSE}_{\mathrm{eRTI}}$ as

$$\mathrm{MSE}_{\mathrm{eRTI}}(O,R) = \frac{1}{N_c * N_p * N_i} \sum_i \sum_c \sum_{(u,v)} (O(u,v)_i^c - R(u,v)_i^c)^2 \tag{5.2}$$

where i varies from 0 to N_i, indicating one of the images acquired by one of the domes, $O(u,v)_i^c$ is the acquired image from the light direction i and $R(u,v)_i^c$ is the rendered image from the same light direction.
MSE_{eRTI} from equation 5.2 depends from the parameters used to render $R(u,v)_i^c$, that are k_d, k_s, α and the glossiness model $G_{2\,\text{or}\,3}$.
To find the minimum for MSE_{eRTI} as a function of the parameters, the methodology followed is:

- select a fitting method: JacobiSVD algorithm (SVD), NECF algorithm (ROOT), QR algorithm (QR), LTS algorithm (ROBUST);
- fix a value for α and a gloss model $G_{2\,\text{or}\,3}$;
- find the minimum for k_d: k_d^m;
- fix the minimum k_d^m and find the minimum for k_s;

The value of MSE_{eRTI} as a function of k_d for the mosaic is presented in figure 5.2a and for the coin collection in figure 5.2b.
It can be noticed that the minimum for coins is at $k_d(\textbf{coins}) = 1.05$ and for the mosaic is at $k_d(\textbf{mosaic}) = 1.25$. At this level there is no preferred fitting model, since the difference between ROOT, QR and SVD is not significant, but it is already evident that the ROBUST fitting technique is the less well performing. The ROBUST fit will be in all the following cases the worst performing, but it is reported here as a reference.
Given the two values for k_d, $k_d(\textbf{coins})$ and $k_d(\textbf{mosaic})$, it is possible to find the minimum for MSE_{eRTI} as a function of k_s. The results are presented for the mosaic in figure 5.3a and for the coin collection in figure 5.3b using a value of $\alpha = 75$ and the gloss model G_2.
The minimum for the mosaic is at $k_s(\textbf{mosaic}) = 0.65$ for all fitting algorithms, and for the mosaic is at $k_s(\textbf{coins}) = 0.6$ for the ROOT fitting and $k_s(\textbf{coins}) = 0.4$ for QR and SVD fitting algorithms.
Using the minimum for $k_s(\textbf{mosaic})$ it is possible to study how the eRTI performs in respect to RTI/PTM and which glossiness model performs better in term of MSE_{eRTI}. In figure 5.4a the value of MSE as a function of k_d for the eRTI and for the RTI/PTM is compared for the QR fitting algorithm and for the ROBUST. The remaining fitting algorithms are not presented because they are completely overlapping with the QR in this range. The eRTI algorithm performs better in the range of k_d between 0 and 1.7 after that limit the intensity of the diffuse component is strong enough to overexpose the image, and adding the gloss component increases the difference respect the original image. In figure 5.4a the value of MSE as a function of k_d for the gloss models $G_{2\,\text{or}\,3}$ is compared for the QR fitting algorithm. Both eRTI and RTI/PTM MSE are shown for

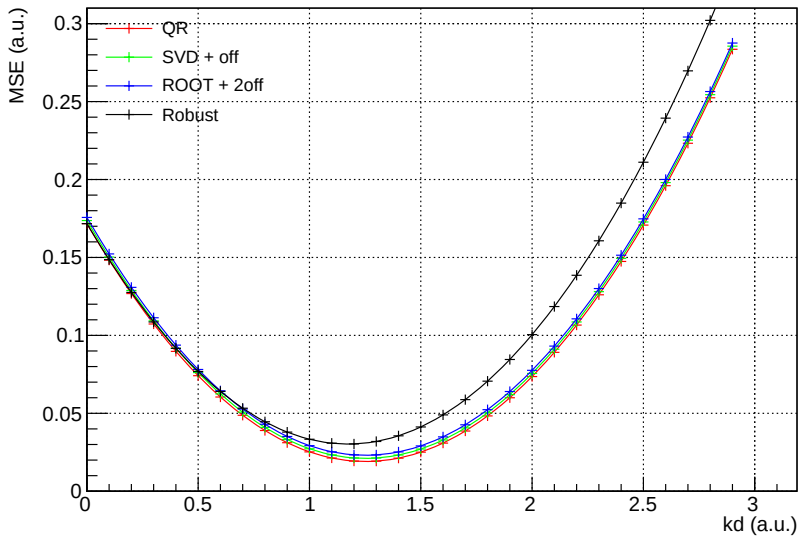

(A) mosaic 4.1b

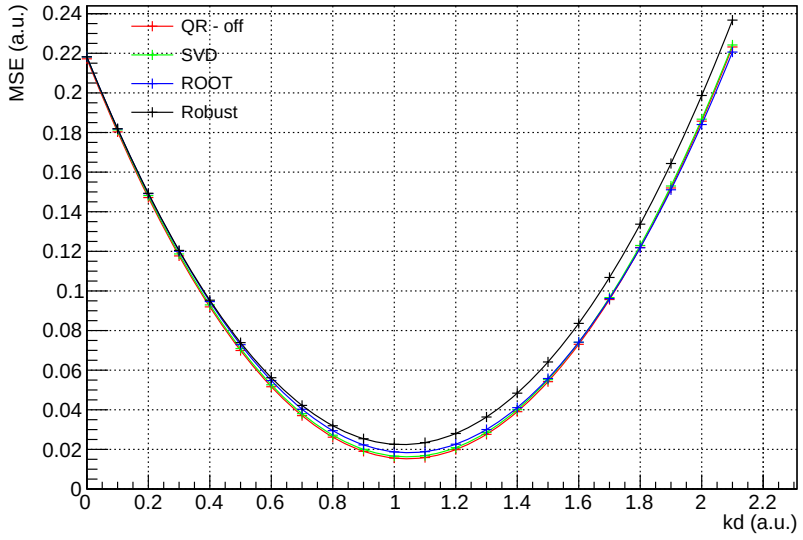

(B) coins 4.1c

FIGURE 5.2: MSE_{eRTI} as a function of k_d, fixed $k_s = 0$, for all the fitting algorithms. For data sets that are coincident a small offset (off) has been added or subtracted.

reference, even if RTI/PTM does not have a gloss component. The eRTI with the G_2 model performs better than any other in the range of k_d between 0 and 1.7. This result is a confirmation of the comments made by the art-historians, that preferred the gloss model G_2 over the G_3.

Similar results are obtained when comparing the value of MSE as a function of k_d for the eRTI and for the RTI/PTM in the case of the coin collections. The values presented in figure 5.5a refers to the fitting models QR and ROOT. Independently of the fitting model, also in the coins case, the eRTI performs better than the standard RTI/PTM in

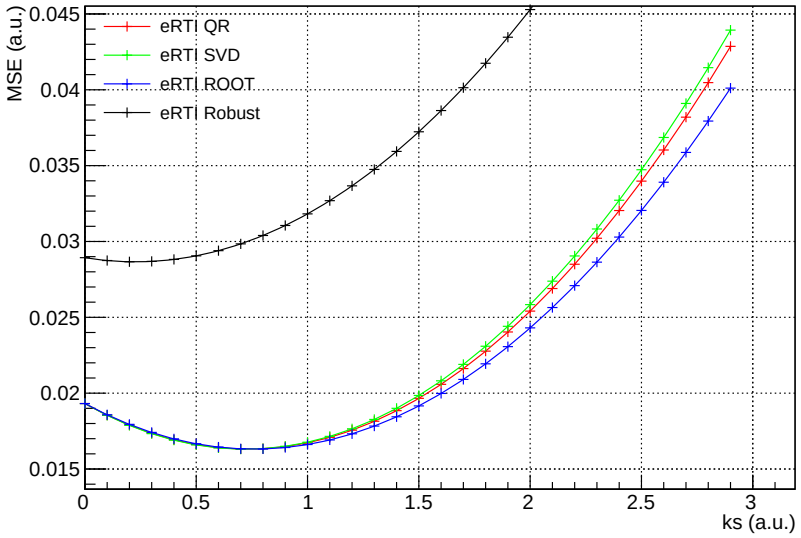

(A) mosaic 4.1b

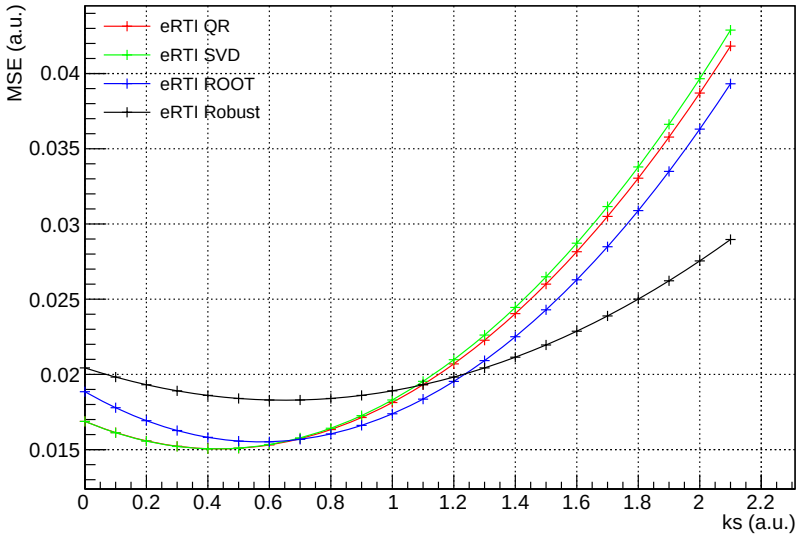

(B) coins 4.1c

FIGURE 5.3: MSE_{eRTI} as a function of k_s, fixed k_d and $\alpha = 75$ and gloss model G_2 , for all the fitting algorithms.

the range of $0 < k_d < 2$. Values of $k_d > 2$ cause the image to be overexposed, causing the colors and the structure of the mosaic to fade under a strong white light.

The value of MSE as a function of k_d for the gloss models $G_{2\,\text{or}\,3}$ is presented in figure 5.5b for the coin collection. Also for the coins the G_2 gloss variable gives a smaller value of MSE than G_3. Anyway, both are performing better than RTI/PTM. Also in this case, the agreement between the results obtained with this quantitative approach and the discussion with art-historians is good.

In figure 5.6 is presented a study of the role of the variable α. The behavior of MSE_{eRTI}

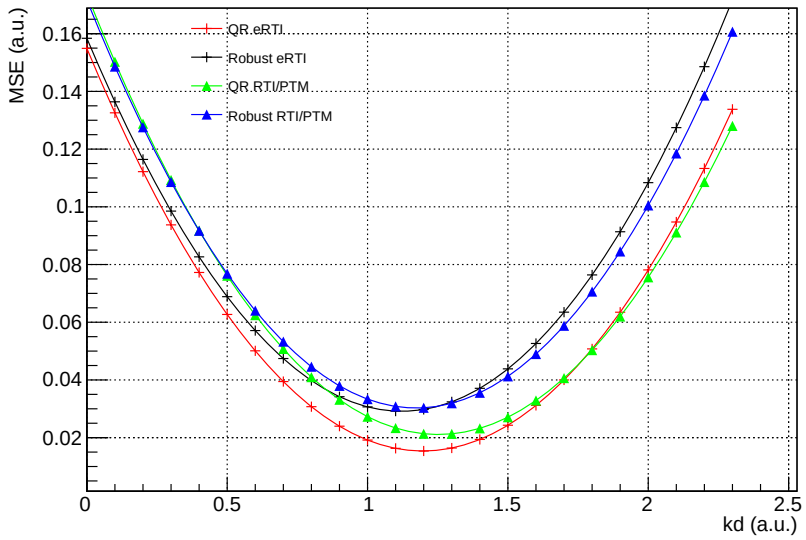

(A) eRTI vs RTI/TPM

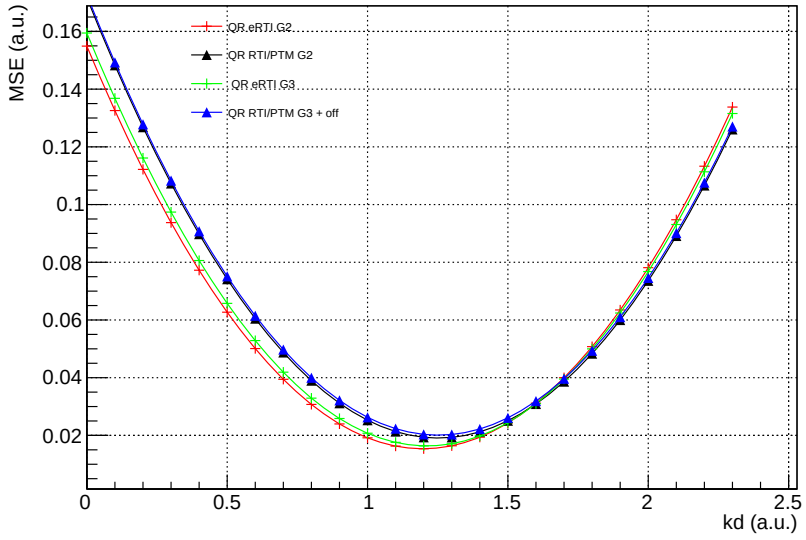

(B) $G_{2\,\mathrm{or}\,3}$

FIGURE 5.4: MSE as a function of k_d for the mosaic

as a function of k_s for various fitting methods is presented only for the mosaic, since with the coins the results are identical.
Three different values of α have been selected, $50, 75, 100$. Those are all values that have been used during the discussion with art-historians.

- Figure 5.6a presents the case where $\alpha = 50$,
- Figure 5.6b where $\alpha = 75$,
- Figure 5.6c where $\alpha = 100$.

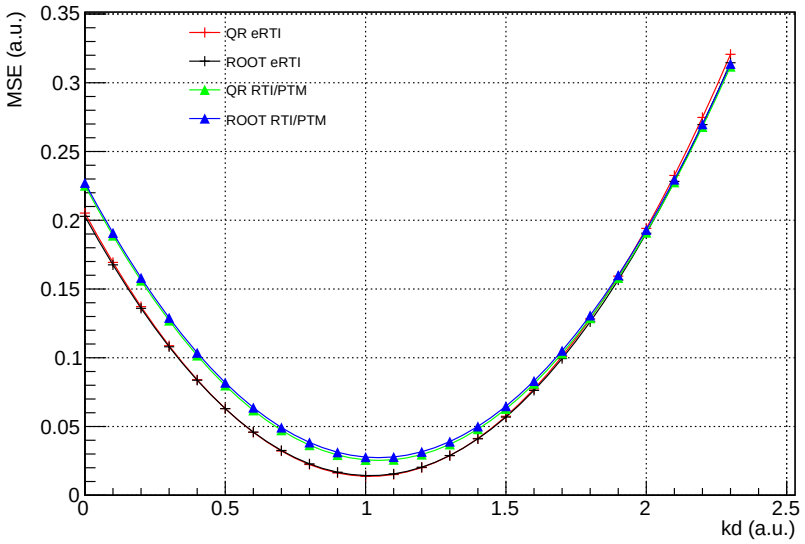

(A) eRTI vs RTI/TPM

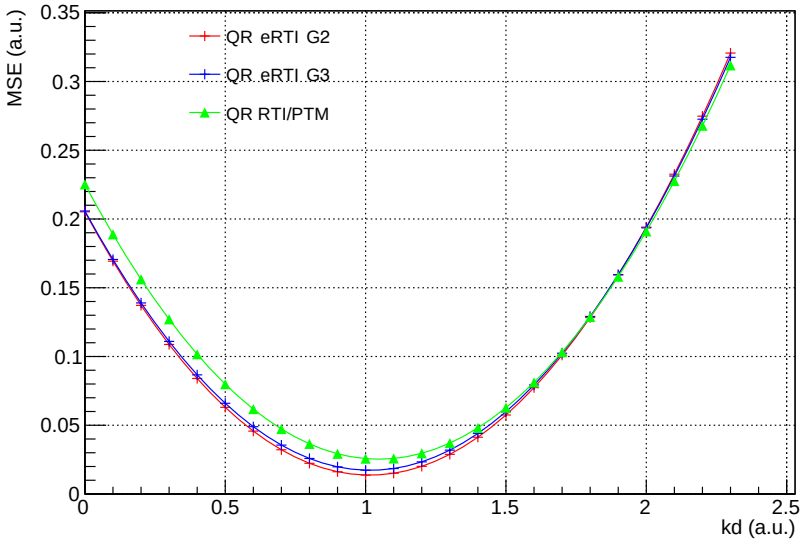

(B) $G_{2\,\mathrm{or}\,3}$

FIGURE 5.5: MSE as a function of k_d for the coin collection

The values selected do represent the most commonly used of the possible values of α, not the extreme scenarios. Comparing the three graphs, it can be noticed that there is almost no dependence between the minimum for k_s and the α chosen. Also the fitting algorithm seems not to play any role in this case. This is, as commented above, not valid for the ROBUST fitting technique. Those results confirm the outcomes of the discussion with art-historians. The absolute minimum value for $\mathrm{MSE}_{\mathrm{eRTI}}$ is obtained in the case where $\alpha = 75$.

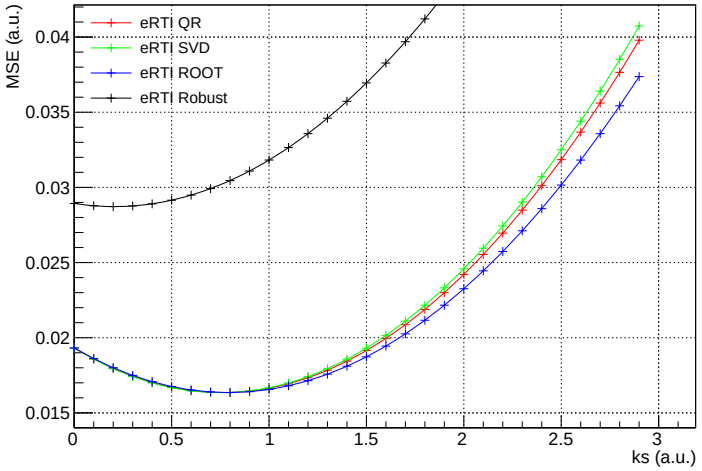

(A) $\alpha = 50$

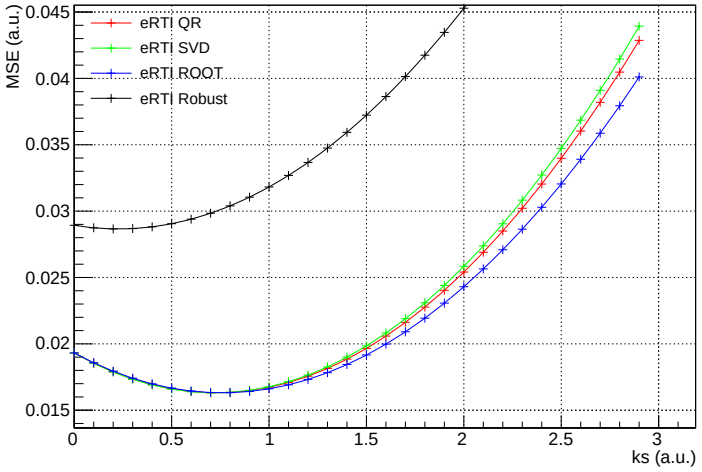

(B) $\alpha = 75$

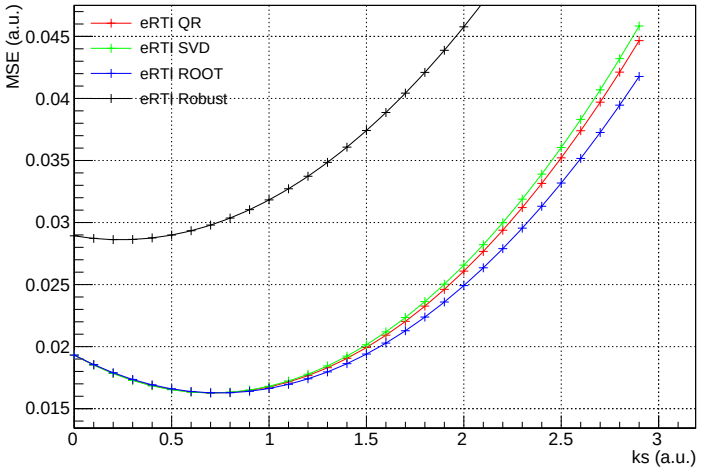

(C) $\alpha = 100$

FIGURE 5.6: MSE_{eRTI} as a function of k_s for different values of the parameter α

Chapter 6

Conclusion and outlook

The results presented in this thesis concern several aspects of the acquisition and visualization of surfaces. Several techniques have been developed since the first days of computer graphics, for example: photometric stereo [148] [149], three dimensional scanning [150] using structured or modulated light just to mention some of them. Cultural heritage artifacts have become immediately the test objects and benchmark tool for those techniques. A more recent approach has been explored and improved in this thesis: Reflection Transformation Imaging (RTI)[1] was initially developed in 2001 by a group of researchers at HP [2]. The choice of RTI has been motivated by three main reasons:

- it provides high-quality images relightable from many direction;
- it can be embedded in any web browser using WebGL, that is supported without the need of any external plug-in;
- the hardware needed to acquire RTIs is easy to operate with little training.

Those advantages over the other possible techniques are furthermore enriched by its robustness and consistency in the visual results that can be obtained. The main disadvantage of RTI is its intrinsic inability to properly represent glossy surfaces, due to the limitation of the simple polynomial texture mapping (PTM)[2] mathematical model. On the other side, a complex function, that is able to describe specular and diffuse reflection may easily lead to instabilities in the fitting process or may complicate the rendering process, requiring more time for each rendering, with the consequence of limiting the possible usage. For example in web-environment performance is crucial for a realistic real time experience. To overcome these weakness an enhanced version of RTI has been proposed in this work and it has been called enhanced RTI (eRTI).

Using eRTI it is possible to capture and visualize surfaces that are composed of multiple types of materials, with different reflection proprieties, such as different intensity of gloss. In addition, such an approach can be applied with most technologies known from computer graphics. Web technology is the key to environments that allow an evaluation of the digital representations of artwork, like Virtual Research Environments. A VRE that has been developed at the DHLab is Salsah [145]. With Salsah, RTI images can be annotated, enriched with comments and they can be interlinked with other objects. Furthermore the researchers may want to integrate information coming from other types of scientific photographs, such as infrared or ultraviolet illuminated or induced fluorescence photography to enrich the visual impression of renderings of artwork by usually non-visual aspects. Especially the combination of such scientific photographs with eRTI images is advantageous because multiple visual impressions can be combined in a way that would not be possible in reality.
The qualities of eRTI have been tested using a novel approach that includes a quantitative and a qualitative method. The two approaches can be summarized as:

- Qualitative method: the art historian user could change the free parameters using a GUI (graphical user interface) in the web viewer. This affected the gloss appearance and triggered discussions on the specific object. The results from collected from this discussion have been summarized in table 5.2.
- Quantitative method: a function to calculate the distance of each photo acquired by the experimental set-up with an image elaborated using the viewer has been defined, see section 5.3. Therefore an index measures the adherence of the model to the data. This index has been calculated for the same test objects that where presented to the art-historian.

This allows the comparison of the two methodologies. The results show agreement between the art-historian discussion and the quantitative measure. This outcome underline once more the importance and usefulness of the dialog between humanities researchers, scientists and developers in an interdisciplinary project.
Another crucial aspect is simplicity for operating a RTI acquisition and creation. A workflow that is composed of three parts has been proposed in this thesis: acquisition of the images, processing through custom made software and visualizing in a web environment.
Regarding the first part, the acquisition of images, multiple advances has been done and they are described in Chapter 3. The introduction of leds, for example, as calibrated light sources greatly improves the portability of the system. Pre-calibrated hardware allows fast capturing of complete image sequences. The software for creating eRTIs has

been greatly improved and new features have been introduced. The algorithm developed to process eRTI resulted in an application for a patent, "Computer System and Method for Improved Gloss Representation in Digital Images" (PCT/EP2016/067045). The software to visualize eRTI on any web-browser has been released on github [135]. Support of web-browsers means that no specific application has to be installed. It supports International Image Interoperability Framework (IIIF) [134]. The concept of IIIF is simplifying image access thanks to programming interfaces that support interoperability between image repositories, for this reason a high-performance media server developed at the DHLab (SIPI) [151].

Future work will focus on the visualization of eRTI textures on 3D surfaces. This will be possible combining the information stored in the eRTIs with the information coming from a 3d scan. Using the normals of the surface it should be possible to match the two measurements, creating an improved and data-based texture.

Further improvements regard the fidelity of color reproduction, that can be obtained by implementing ICC-compliant RTI color-management. Moreover an interesting addition to the viewer would be the possibility to choose the reflection model. In this thesis the reflection model used was the Phong reflection model[40], but other could be easily adapted to the rti.js viewer. An example could be the Ward reflection model[41], that delivers a more realistic impression of gloss.

In the context of research an interesting new feature of the rti.js viewer would be the integration of UV and IR images. The user could benefit from the possibility of comparing eRTIs with the UV/IR images, exploring different layers of the object. This, once integrated into a VRE would allow the user to annotate different regions of interest and correlate the multispectral images with the eRTIs.

Acknowledgments

This dissertation would not have been possible without the help and support of several people that I want to thank in this last chapter.

I would like to express my sincere gratitude to my advisor Dr. Peter Fornaro for allowing me to start this PhD project and for guiding me through it. We had numerous discussion that always ended up with new ideas. He always encouraged and stimulated my intellectual freedom, guiding the discussion with positive attitude. A sincere thanks goes to Prof. Lukas Rosenthaler for the several interesting discussion and the uncountable hours spent programming SIPI together. I would like to thank Lothar Schmitt, Aeneas Kaiser and Heidrun Feldmann without whom the project would not been a success, it has been a pleasure working and talking with you. Thanks to all the DHLab people, Benjamin Geer, Tobias Schweizer, Sofia Georgakopoulou, Ivan Subotic, Sepideh Alassi, for all the cheerful moments and happy memories that I will always bring with me. I could not have asked for more, the DHLab has been an amazing place to work for those 3 years. Special thanks also to Prof. Barbara Schellewald from the art-history department for the interesting and motivating talks and discussions. A particular thanks goes to Prof. Ernst Meyer, Prof. Martino Poggio, Prof. Christoph Bruder and Prof. Sabine Süsstrunck for the useful discussions and for taking part in the thesis committee. Different kind of thanks go to my family and friends. Serena and Milo for making me happy every day more than the previous. Without your help, support and love, Serena, I would not be where I am now. Thanks, I love you. Thanks to my parents for being the best parents in the world, supporting me and guiding me through difficult times. Thanks to Alice for being a fantastic sister and friend. To all my friends, spread around the world: in Switzerland, Italy, Belgium, Netherlands, France, Spain, USA, Germany and who knows where else. Thanks for making me feel at home whenever we meet.

Bibliography

[1] Mark Mudge, Tom Malzbender, Alan Chalmers, Roberto Scopigno, James Davis, Oliver Wang, Prabath Gunawardane, Michael Ashley, Martin Doerr, Alberto Proenca, and Joo Barbosa. Image-Based Empirical Information Acquisition , Scientific Reliability , and Long-Term Digital Preservation for the Natural Sciences and Cultural Heritage. In *EUROGRAPHICS*, 2008. URL `http://culturalheritageimaging.org/What_We_Do/Publications/eurographics2008/`.

[2] Tom Malzbender, Dan Gelb, and Hans Wolters. Polynomial texture maps. *Proceedings of SIGGRAPH '01*, 2001. ISSN 00218855. doi: http://doi.acm.org/10.1145/383259.383320.

[3] Three.js javascript 3d library. URL `https://github.com/mrdoob/three.js/`. accessed: 4-2017.

[4] The Khronos Group. Webgl, . URL `https://www.khronos.org/webgl/`. accessed: 2-2017.

[5] The Khronos Group. Opengl, . URL `https://www.opengl.org/`. accessed: 2-2017.

[6] Gnther Wyszecki and W. S. Stiles. *Color Science: Concepts and Methods, Quantitative Data and Formulae, 2nd Edition*. John Wiley and Sons, 2000. ISBN 978-0-471-39918-6.

[7] Janos Schanda. *Colorimetry: Understanding the CIE System*. John Wiley & Sons, Ltd, 2007. ISBN 978-0-470-04904-4.

[8] Roy S. Berns. *Billmeyer and Saltzman's principles of color technology*. John Wiley & Sons, Ltd, 2000.

[9] Yue Dong, Stephen Lin, and Baining Guo. *Material Appearance Modeling: A Data-Coherent Approach*. 2013. ISBN 978-3-642-35776-3. doi: 10.1007/978-3-642-35777-0. URL `http://link.springer.com/10.1007/978-3-642-35777-0`.

[10] Julie Dorsey, Holly Rushmeier, and Franois Sillion. *Digital modeling of material appearance*. Boston, Boston, 2008. ISBN 9780122211812.

[11] I. Newton. New Theory about Light and Colors. *Philosophical Transactions of the Royal Society of London*, 6(69-80):3075–3087, 1 1671. ISSN 0261-0523. doi: 10.1098/rstl.1671.0072. URL `http://rstl.royalsocietypublishing.org/cgi/doi/10.1098/rstl.1671.0072`.

[12] Johann Wolfgang von Goethe. *Theory of Colours*. John Murray, 1810.

[13] T. Young. The Bakerian Lecture: On the Theory of Light and Colours. *Philosophical Transactions of the Royal Society of London*, 92:12–48, 1 1802. ISSN 0261-0523. doi: 10.1098/rstl.1802.0004. URL `http://rstl.royalsocietypublishing.org/cgi/doi/10.1098/rstl.1802.0004`.

[14] Hermann von Helmholtz. *Handbuch der physiologischen Optik*. Voss, 1867.

[15] G Svaetichin. *Spectral Response Curves from Single Cones*. Acta Physiologica Scandinavica. Vol.39, Supplement 134:2. acta physiologica, 1956. URL `https://books.google.nl/books?id=7bYgGwAACAAJ`.

[16] Roy S. Berns. *Billmeyer and Saltzman's principles of color technology, 3rd edition*. 4 2000. ISBN 978-0-471-19459-0.

[17] CIE Central Bureau. eilv online. URL `http://eilv.cie.co.at/`. version: 017/E:2011.

[18] Kurt Nassau. The fifteen causes of color: The physics and chemistry of color. *Color Research & Application*, 12(1):4–26, 2 1987. ISSN 03612317. doi: 10.1002/col.5080120105. URL `http://doi.wiley.com/10.1002/col.5080120105`.

[19] Rod Nave. hyperphysics. URL `http://hyperphysics.phy-astr.gsu.edu/`. accessed: 2-2017.

[20] A. R. Robertson. Computation of Correlated Color Temperature and Distribution Temperature. *Journal of the Optical Society of America*, 58(11):1528, 11 1968. ISSN 0030-3941. doi: 10.1364/JOSA.58.001528. URL `https://www.osapublishing.org/abstract.cfm?URI=josa-58-11-1528`.

[21] C. S. McCamy. Correlated color temperature as an explicit function of chromaticity coordinates. *Color Research & Application*, 17(2):142–144, 1992. ISSN 15206378. doi: 10.1002/col.5080170211.

[22] J L Gardner. Correlated colour temperature - uncertainty and estimation. *Metrologia*, 37(5):381–384, 2000. ISSN 0026-1394. doi: 10.1088/0026-1394/

37/5/8. URL http://stacks.iop.org/0026-1394/37/i=5/a=8?key=crossref.718245c52e01767f973217240371d26a.

[23] Richard Feynman, Robert B. Leighton, and Matthew Sands. *The Feynmann Lectures on Physics*. Pearson Addison Wesley, 2006.

[24] David K. Lynch and William Charles Livingston. *Color and Light in Nature*. Cambridge University Press, 2001.

[25] David H. Sliney, Robert T. Wangemann, James K. Franks, and Myron L. Wolbarsht. Visual sensitivity of the eye to infrared laser radiation. *Journal of the Optical Society of America*, 66(4):339, 4 1976. ISSN 0030-3941. doi: 10.1364/JOSA.66.000339. URL https://www.osapublishing.org/abstract.cfm?URI=josa-66-4-339.

[26] Rice University OpenStax College. Anatomy and physiology. URL http://cnx.org/contents/14fb4ad7-39a1-4eee-ab6e-3ef2482e3e22. accessed: 2-2017.

[27] Eugene Ackerman. *Biophysical Science*. Prentice-Hall, 1962.

[28] Andrew Stockman and Lindsay T. Sharpe. The spectral sensitivities of the middle- and long-wavelength-sensitive cones derived from measurements in observers of known genotype. *Vision Research*, 40(13):1711–1737, 2000. ISSN 00426989. doi: 10.1016/S0042-6989(00)00021-3.

[29] H. Grassmann. Zur Theorie der Farbenmischung. *Annalen der Physik und Chemie*, 165(5):69–84, 1853. ISSN 00033804. doi: 10.1002/andp.18531650505. URL http://doi.wiley.com/10.1002/andp.18531650505.

[30] J. Guild. The Colorimetric Properties of the Spectrum. *Philosophical Transactions of the Royal Society A: Mathematical, Physical and Engineering Sciences*, 230(681-693):149–187, 1 1932. ISSN 1364-503X. doi: 10.1098/rsta.1932.0005. URL http://rsta.royalsocietypublishing.org/cgi/doi/10.1098/rsta.1932.0005.

[31] W D Wright. A re-determination of the trichromatic coefficients of the spectral colours. *Transactions of the Optical Society*, 30(4):141–164, 3 1929. ISSN 1475-4878. doi: 10.1088/1475-4878/30/4/301. URL http://stacks.iop.org/1475-4878/30/i=4/a=301?key=crossref.bca596fafe3b9f0d818d38efdaabf6ee.

[32] D. B Judd. NoReport of U.S. Secretariat Committee on Colorimetry and Artificial Daylight. *Proceedings of the Twelfth Session of the CIE, Stockholm*, 1951.

[33] David L MacAdam. Visual Sensitivities to Color Differences in Daylight. *J. Opt. Soc. Am.*, 32(5):247–274, 5 1942. doi: 10.1364/JOSA.32.000247. URL `http://www.osapublishing.org/abstract.cfm?URI=josa-32-5-247`.

[34] IEC. Colour management - default rgb colour space - srgb. URL `https://webstore.iec.ch/publication/6169`. accessed: 2-2017.

[35] adobe. Adobergb. URL `http://www.adobe.com/digitalimag/adobergb.html`. accessed: 2-2017.

[36] ISO. Iso 9288:1989, . URL `https://www.iso.org/standard/16943.html`. accessed: 2-2017.

[37] Philip Dutré. Global Illumination Compendium, 2003. URL `http://www.cs.kuleuven.ac.be/~phil/GI/https://academic.oup.com/jid/article-lookup/doi/10.1093/infdis/jiu169`.

[38] F E Nicodemus. Directional Reflectance and Emissivity of an Opaque Surface. *Applied optics*, 4(7):767–773, 1965. ISSN 0003-6935. doi: 10.1364/AO.9.001474.

[39] F E Nicodemus, J J Hsia, J C Richmond, I W Ginsber, and T Limperis. *Geometrical considerations and nomenclature for reflectance*. Number October. U.S. Department of Commerce. National Bureau of Standards, Washington, DC 20234, nbs monogr edition, 1977. URL `http://graphics.stanford.edu/courses/cs448-05-winter/papers/nicodemus-brdf-nist.pdf`.

[40] Bui Tuong Phong. Illumination for computer generated pictures. *Communications of the ACM*, 18(6):311–317, 1975. ISSN 00010782. doi: 10.1145/360825.360839.

[41] Gregory J. Ward. Measuring and modeling anisotropic reflection. *ACM SIGGRAPH Computer Graphics*, 26(2):265–272, 1992. ISSN 00978930. doi: 10.1145/142920.134078.

[42] James F. Blinn. Light reflection functions for simulation of clouds and dusty surfaces. *ACM SIGGRAPH Computer Graphics*, 16(3):21–29, 1982. ISSN 00978930. doi: 10.1145/965145.801255.

[43] R.L. Cook and K.E. Torrance. A Reflectance Model for Computer Graphics. *ACM SIGGRAPH Computer Graphics*, 15(3):307–316, 1981. ISSN 00978930. doi: 10.1145/965161.806819.

[44] Eric P. F. Lafortune, Sing-Choong Foo, Kenneth E. Torrance, and Donald P. Greenberg. Non-linear approximation of reflectance functions. *Proceedings of the 24th annual conference on Computer graphics and interactive techniques -*

SIGGRAPH '97, 31(3):117–126, 1997. ISSN 0097-8930. doi: 10.1145/258734.258801. URL http://portal.acm.org/citation.cfm?doid=258734.258801.

[45] Katsushi Ikeuchi, editor. *Computer Vision L*. Springer US, Boston, MA, 2014. ISBN 978-0-387-30771-8. doi: 10.1007/978-0-387-31439-6. URL http://link.springer.com/10.1007/978-0-387-31439-6.

[46] Robert R Lewis. Making Shaders More Physically Plausible. *Computer Graphics Forum*, 13(2):109120, 1994. ISSN 14678659. doi: 10.1111/1467-8659.1320109. URL http://www3.interscience.wiley.com/journal/120705787/abstract.

[47] W C Snyder, Z Wan, and X Li. Thermodynamic Constraints on Reflectance Reciprocity and Kirchhoff's Law. *Applied optics*, 37(16):3464–3470, 1998. ISSN 0003-6935. doi: 10.1364/AO.37.003464.

[48] William C. Snyder. Definition and invariance properties of structured surface BRDF. *IEEE Transactions on Geoscience and Remote Sensing*, 40(5):1032–1037, 2002. ISSN 01962892. doi: 10.1109/TGRS.2002.1010890.

[49] ISO. Iso 2813:2014, . URL https://www.iso.org/standard/56807.html. accessed: 2-2017.

[50] A.C. Chadwick and R.W. Kentridge. The perception of gloss: A review. *Vision Research*, 109:221–235, 2015. ISSN 00426989. doi: 10.1016/j.visres.2014.10.026. URL http://linkinghub.elsevier.com/retrieve/pii/S0042698914002594.

[51] Christiane B. Wiebel, Matteo Toscani, and Karl R. Gegenfurtner. Statistical correlates of perceived gloss in natural images. *Vision Research*, 115 (doi:10.1016/j.visres.2015.04.010):175–187, 2015. ISSN 00426989. doi: 10.1016/j.visres.2015.04.010. URL http://linkinghub.elsevier.com/retrieve/pii/S0042698915001595.

[52] Juno Kim and Barton L Anderson. Image statistics and the perception of surface gloss and lightness. *Journal of vision*, 10(9):3, 2010. ISSN 1534-7362. doi: 10.1167/10.9.3.

[53] Hidehiko Komatsu, Akiko Nishio, Gouki Okazawa, and Naokazu Goda. Yellow or Gold?: Neural Processing of Gloss Information. pages 1–12. 2013. doi: 10.1007/978-3-642-36700-7{_}1. URL http://link.springer.com/10.1007/978-3-642-36700-7_1.

[54] F Pellacini, J Ferwerda, and D Greenberg. Toward a Psychophysically-based Light Reflection Model for Image Synthesis. *Computer Graphics*, 34(Annual Conference Series):55–64, 2000.

[55] Ferdinand Braun. Ueber ein Verfahren zur Demonstration und zum Studium des zeitlichen Verlaufes variabler Ströme. *Annalen der Physik und Chemie*, 296(3): 552–559, 1897. ISSN 00033804. doi: 10.1002/andp.18972960313. URL `http://doi.wiley.com/10.1002/andp.18972960313`.

[56] Siggraph. URL `http://www.siggraph.org/`. accessed: 2-2017.

[57] Ann Torrence. Martin Newell's original teapot. In *ACM SIGGRAPH 2006 Teapot on - SIGGRAPH '06*, page 29, New York, New York, USA, 2006. ACM Press. ISBN 1595933646. doi: 10.1145/1180098.1180128. URL `http://portal.acm.org/citation.cfm?doid=1180098.1180128`.

[58] F Ganovelli, M Corsini, S Pattanaik, and Marco Di Benedetto. *Introduction to Computer Graphics: A Practical Learning Approach*. Eds. CRC Press, chapman & edition, 2014. ISBN 978-1439852798.

[59] Phong shading model. URL `https://commons.wikimedia.org/wiki/File:Phong_components_version_4.png`. accessed: 2-2017.

[60] E. Lafortune and Y. Willems. Using the Modified Phong brdf for Physically Based Rendering. Technical report, K.U.Leuven, 1994. URL `http://www.graphics.cornell.edu/~eric/Phong.htmlhttp://www.mendeley.com/research/using-modified-phong-brdf-physically-based-rendering/`.

[61] Phong components. URL `https://commons.wikimedia.org/wiki/File:Phong_components_version_4.png`. accessed: 2-2017.

[62] Maria E Nadal and E Ambler Thompson. NIST Reference Goniophotometer for Specular Gloss Measurements. *Journal of Coatings Technology*, 73(917):73–80, 2001. ISSN 03618773. doi: 10.1007/BF02698400.

[63] blender. URL `https://www.blender.org/`. accessed: 2-2017.

[64] Greg Ward. The RADIANCE 4.2 Synthetic Imaging System. *University of California*, (September):1–7, 1994. URL `http://radsite.lbl.gov/radiance/refer/ray.html#Materials`.

[65] Dan B. Goldman, Brian Curless, Aaron Hertzmann, and Steven M. Seitz. Shape and spatially-varying BRDFs from photometric stereo. *IEEE Transactions on Pattern Analysis and Machine Intelligence*, 32(6):1060–1071, 2010. ISSN 01628828. doi: 10.1109/TPAMI.2009.102.

[66] O. Wang, P. Gunawardane, S. Scher, and J. Davis. Material classification using BRDF slices. *IEEE Conference on Computer Vision and Pattern Recognition*, pages 2805–2811, 6 2009. doi: 10.1109/CVPR.2009.5206558. URL http://ieeexplore.ieee.org/lpdocs/epic03/wrapper.htm?arnumber=5206558.

[67] Jonathan Dupuy. Photorealistic Surface Rendering with Microfacet Theory. 2016. URL https://hal.archives-ouvertes.fr/tel-01291974.

[68] Robert Efron. Conservation of temporal information by perceptual systems. *Perception & Psychophysics*, 14(3):518–530, 1973. ISSN 0031-5117. doi: 10.3758/BF03211193. URL http://www.springerlink.com/index/10.3758/BF03211193.

[69] Mark Mudge, Tom Malzbender, Carla Schroer, and Marlin Lum. New Reflection Transformation Imaging Methods for Rock Art and Multiple-Viewpoint Display. In *The 7th International Symposium on Virtual Reality, Archaeology and Cultural Heritage (VAST2006)*, pages 195–200. Eurographics Association, 2006. URL http://www.c-h-i.org/events/VAST2006_final.pdf.

[70] Chi. URL http://culturalheritageimaging.org/Technologies/RTI/. accessed: 2-2017.

[71] Gene H. Golub and Charles F. Van Loan. *Matrix Computations (3rd Ed.)*. Johns Hopkins University Press, 1996. ISBN 0-8018-5414-8.

[72] L MacDonald and Stuart Robson. Polynomial Texture Mapping and 3D Representations. *International Archives of Photogrammetry*, XXXVIII(8):422–427, 2010. ISSN 15740846. URL http://www.isprs.org/proceedings/XXXVIII/part5/papers/152.pdf.

[73] Gregory Bearman, Eric Doehne, Dale Kronkright, and Marcello Manfredi. RTI Surface Normal Calibration with a 3D Printed Spatial Target : Turning Images into Data. page 8, 2014.

[74] Lw MacDonald. Colour and Directionality in Surface Reflectance. *Proceedings of the 50th Anniversary Convention of the AISB*, (1):1–7, 2014. URL http://doc.gold.ac.uk/aisb50/AISB50-S20/aisb50-S20-macdonald-paper.pdf%5Cnhttp://aisb50.org/.

[75] Mingjing Zhang, Mark S Drew, and Mark S Drew. Efficient robust image interpolation and surface properties using polynomial texture mapping. *EURASIP Journal on Image and Video Processing*, 2014(1):25, 2014. ISSN 1687-5281. doi: 10.1186/1687-5281-2014-25. URL http://jivp.eurasipjournals.com/content/2014/1/25.

[76] Tom Malzbender and Bennett Wilburn. Surface enhancement using real-time photometric stereo and reflectance transformation. *Proceedings of the Eurographics Symposium on Rendering Techniques*, pages 245–150, 2006. doi: 10.2312/EGWR/EGSR06/245-250. URL `http://citeseerx.ist.psu.edu/viewdoc/download?doi=10.1.1.72.1703&rep=rep1&type=pdf`.

[77] Mark S. Drew, Nasim Hajari, Yacov Hel-Or, and Tom Malzbender. Specularity and Shadow Interpolation via Robust Polynomial Texture Maps. *Procedings of the British Machine Vision Conference 2009*, pages 1–114, 2009. doi: 10.5244/C.23.114. URL `http://www.bmva.org/bmvc/2009/Papers/Paper142/Paper142.html`.

[78] Mark S. Drew, Yacov Hel-Or, Tom Malzbender, and Nasim Hajari. Robust estimation of surface properties and interpolation of shadow/specularity components. *Image and Vision Computing*, 30(4-5):317–331, 2012. ISSN 02628856. doi: 10.1016/j.imavis.2012.02.012.

[79] Mingjing Zhang and Mark S. Drew. Robust Luminance and Chromaticity for Matte Regression in Polynomial Texture Mapping. In *Lecture Notes in Computer Science (including subseries Lecture Notes in Artificial Intelligence and Lecture Notes in Bioinformatics)*, volume 7584 LNCS, pages 360–369. 2012. ISBN 9783642338670. doi: 10.1007/978-3-642-33868-7{_}36. URL `http://link.springer.com/10.1007/978-3-642-33868-7_36`.

[80] Peter Rousseeuw. Least Median of Squares Regression. *Journal of the American Statistical Association*, 79(388):871–880, 1984. ISSN 0162-1459. doi: 10.1080/01621459.1984.10477105. URL `http://www.tandfonline.com/doi/abs/10.1080/01621459.1984.10477105`.

[81] Rene Brun and Fons Rademakers. ROOT - An Object Oriented Data Analysis Framework. In *Proceedings AIHENP'96 Workshop, Lausanne, Sep. 1996*, pages 81–86. Nucl. Inst. & Meth. in Phys. Res. A 389, 1997.

[82] Gianpaolo Palma, Massimiliano Corsini, Paolo Cignoni, Roberto Scopigno, and Mark Mudge. Dynamic shading enhancement for reflectance transformation imaging. *Journal on Computing and Cultural Heritage*, 3(2):1–20, 2010. ISSN 15564673. doi: 10.1145/1841317.1841321.

[83] G PALMA. *Surface Appearance Estimation from Video Sequences*. PhD thesis, Università degli Studi di Pisa, 2013. URL `http://etd.adm.unipi.it/t/etd-05212013-172635/`.

[84] Qt. URL `https://www.qt.io/`. accessed: 2-2017.

[85] Marco Di Benedetto and Federico Ponchio. SpiderGL: a JavaScript 3D graphics library for next-generation WWW. *... Conference on Web 3D ...*, 1(212):165–174, 2010. URL `http://dl.acm.org/citation.cfm?id=1836075`.

[86] M Di Benedetto. Spidergl: A graphics library for 3d web applications. *... Archives of the ...*, XXXVIII(March):2–4, 2011. URL `http://www.int-arch-photogramm-remote-sens-spatial-inf-sci.net/XXXVIII-5-W16/467/2011/isprsarchives-XXXVIII-5-W16-467-2011.pdf`.

[87] Spidergl. URL `http://vcg.isti.cnr.it/spidergl/`. accessed: 2-2017.

[88] Lindsay MacDonald, John Hindmarch, Stuart Robson, and Melissa Terras. Modelling the appearance of heritage metallic surfaces. *ISPRS - International Archives of the Photogrammetry, Remote Sensing and Spatial Information Sciences*, XL-5(5):371–377, 6 2014. ISSN 2194-9034. doi: 10.5194/isprsarchives-XL-5-371-2014. URL `http://www.int-arch-photogramm-remote-sens-spatial-inf-sci.net/XL-5/371/2014/`.

[89] Gilles Pitard, Gatan LeGoïc, Alamin Mansouri, Hugues Favrelière, Simon-Frederic Desage, Serge Samper, and Maurice Pillet. Discrete Modal Decomposition: a new approach for the reflectance modeling and rendering of real surfaces. *Machine Vision and Applications*, 2017. ISSN 0932-8092. doi: 10.1007/s00138-017-0856-0. URL `http://link.springer.com/10.1007/s00138-017-0856-0`.

[90] X. Huang, M. Walton, G. Bearman, and O. Cossairt. Near Light Correction for Image Relighting and 3D Shape Recovery. *Digital Heritage*, (SEPTEMBER), 2015.

[91] Yong Hwi Kim, Junho Choi, Yong Yi Lee, Bilal Ahmed, and Kwan H. Lee. Reflectance Transformation Imaging Method for Large-Scale Objects. *2016 13th International Conference on Computer Graphics, Imaging and Visualization (CGiV)*, pages 84–87, 2016. doi: 10.1109/CGiV.2016.25. URL `http://ieeexplore.ieee.org/lpdocs/epic03/wrapper.htm?arnumber=7467687`.

[92] Lindsay Macdonald, Ben Altshuler, Jane Masséglia, Sarah Norodom, James Grasby, Charles Crowther, and Andrew Cuffley. Imaging the Egyptian Obelisk at Kingston Lacy. *EVA 2015*, (November):252–260, 2015.

[93] R Pintus, I Ciortan, A Giachetti, and E Gobbetti. Practical Free-form RTI Acquisition with Local Spot Lights. In *STAG: Smart Tools and Apps in computer Graphics*, page We present an automated light calibration pipeline, 2016.

[94] Xavier Aure, Paul O'Dowd, and Joseph Padfield. Generating 3D Models of Paintings Through the Combination of 2D , 3D and RTI Data. In *Electronic Visualisation and the Arts (EVA 2017)*, 2017. doi: 10.14236/ewic/EVA2017.4.

[95] T. Freeth, Y. Bitsakis, X. Moussas, J. H. Seiradakis, A. Tselikas, H. Mangou, M. Zafeiropoulou, R. Hadland, D. Bate, A. Ramsey, M. Allen, A. Crawley, P. Hockley, T. Malzbender, D. Gelb, W. Ambrisco, and M. G. Edmunds. Decoding the ancient Greek astronomical calculator known as the Antikythera Mechanism. *Nature*, 444(7119):587–591, 11 2006. ISSN 0028-0836. doi: 10.1038/nature05357. URL `http://www.nature.com/doifinder/10.1038/nature05357`.

[96] Angelakis, D.G., Christandl, M., Ekert, A., Kay, A., and S. Kulik. *Quantum Information Processing*. IOS Press, 2006.

[97] Graeme Earl, Kirk Martinez, and Tom Malzbender. Archaeological applications of polynomial texture mapping: analysis, conservation and representation. *Journal of Archaeological Science*, 37(8):2040–2050, 8 2010. ISSN 03054403. doi: 10.1016/j.jas.2010.03.009. URL `http://linkinghub.elsevier.com/retrieve/pii/S0305440310001093`.

[98] M. Mudge, C. Schroer, G. Earl, K Martinez, H. Pagi, C. Toler-Franklin, S. Rusinkiewicz, G. Palma, M. Wachowiak, M. Ashey, N Mathews, T. Noble, and M. Dellepian. Principles and practices of robust, photography-based digital imaging techniques for museums. *1th VAST International Symposium on Virtual Reality, Archaeology and Cultural Heritage*, 2010. doi: 10.2312/PE/VAST/VAST10S/111-137. URL `http://eprints.soton.ac.uk/271658/`.

[99] Paula Artal-Isbrand, Philip Klausmeyer, and Winifred Murray. An Evaluation of Decorative Techniques on a Red-Figure Attic Vase from the Worcester Art Museum using Reflectance Transformation Imaging (RTI) and Confocal Microscopy with a Special Focus on the Relief Line. *MRS Proceedings*, 1319:10–1319, 1 2011. ISSN 1946-4274. doi: 10.1557/opl.2011.793. URL `http://journals.cambridge.org/abstract_S1946427411007937`.

[100] Kathryn Piquette. Reflectance Transformation Imaging (RTI) and Ancient Egyptian Material Culture. *The CEHAO newsletter El boletín de noticias del CEHAO 7*, 7, 2011. URL `http://bibliotecadigital.uca.edu.ar/repositorio/revistas/ancient-egyptian-material-culture-piquette.pdf`.

[101] Michael Caine, Moshe; Magen. Pixels and Parchment : The Application of RTI and Infrared Imaging to the Dead Sea Scrolls. *EVA London 2011. Electronic Visualisation and the Arts*, pages 140–146, 2011. URL `http://ewic.bcs.org/upload/pdf/ewic_ev11_s8paper2.pdf`.

[102] Sarah E. Newman. Applications of Reflectance Transformation Imaging (RTI) to the study of bone surface modifications. *Journal of Archaeological Science*, 53: 536–549, 1 2015. ISSN 03054403. doi: 10.1016/j.jas.2014.11.019. URL `http://linkinghub.elsevier.com/retrieve/pii/S0305440314004269`.

[103] Omar Abdel-Kareem, Awad Al-Zahrani, and Mounir Arbach. Authentication and conservation of corroded archaeological Qatabanian and Himyarite silver coins. *Journal of Archaeological Science: Reports*, 9:565–576, 10 2016. ISSN 2352409X. doi: 10.1016/j.jasrep.2016.08.025. URL `http://linkinghub.elsevier.com/retrieve/pii/S2352409X16304916`.

[104] Lindsay MacDonald, Vera Moitinho de Almeida, and Mona Hess. Three-dimensional reconstruction of Roman coins from photometric image sets. *Journal of Electronic Imaging*, 26(1):011017, 2017. ISSN 1017-9909. doi: 10.1117/1.JEI.26.1.011017. URL `http://electronicimaging.spiedigitallibrary.org/article.aspx?doi=10.1117/1.JEI.26.1.011017`.

[105] Rebecca R Benefiel, Jacqueline Dibiasie, Holly Sypniewski, Zimmermann Damer, Kyle Helms, Matthew Loar, Karin Lundqvist, and Fanny Opdenhoff. The Herculaneum Graffiti Project : Initial Field Season , 2014. *The journal of Fasti Online*, 2016.

[106] David Selmo, David Selmo, Fraser Sturt, James Miles, Philip Basford, Tom Malzbender, Kirk Martinez, Charlie Thompson, Graeme Earl, and George Bevan. Underwater reflectance transformation imaging : a technology for in situ underwater cultural heritage object-level recording. 26(1), 2017. doi: 10.1117/1.JEI.26.1.011029.Journal.

[107] James S Hamiel and John S Yoshida. Evaluation and Application of Polynomial Texture Mapping (PTM) in the area of Shoe/Tire Impression Evidence. pages 1–32, 2012.

[108] Weiqi Shi, Eleni Kotoula, Kiraz Akoglu, Ying Yang, and Holly Rushmeier. CHER-Ob : A Tool for Shared Analysis in Cultural Heritage. In *EUROGRAPHICS Workshop on Graphics and Cultural Heritage*, pages 3–6, 2016. URL `http://graphics.cs.yale.edu/site/sites/files/paper1026_CRC.pdf`.

[109] Robin Williams and Gigi Williams. Ultraviolet , Infrared & Fluorescence Photography. *J.Media Med.*, 26 (2):54–9, 2009.

[110] Andrew Davidhazy. *Overview of Infrared and Ultraviolet Photography.* Rochester Institute of Technology. URL `https://people.rit.edu/andpph/text-ir-uv-book.pdf`.

[111] Bernd Jähne. *Practical Handbook on Image Processing for Scientific and Technical Applications, Second Edition*. CRC Press, 3 2004. ISBN 978-0-8493-1900-6. doi: 10.1201/9780849390302. URL http://scholar.google.com/scholar?hl=en&btnG=Search&q=intitle:Practical+handbook+on+image+processing+for+scientific+and+technical+applications#0http://www.crcnetbase.com/doi/book/10.1201/9780849390302.

[112] Pierre Magnan. Detection of visible photons in CCD and CMOS: A comparative view. *Nuclear Instruments and Methods in Physics Research, Section A: Accelerators, Spectrometers, Detectors and Associated Equipment*, 504(1-3):199–212, 2003. ISSN 01689002. doi: 10.1016/S0168-9002(03)00792-7.

[113] Tarek Lulé, Stephan Benthien, Holger Keller, Frank Muetze, Peter Rieve, Konstantin Seibel, Michael Sommer, and Markus Bo??hm. Sensitivity of CMOS based imagers and scaling perspectives. *IEEE Transactions on Electron Devices*, 47(11): 2110–2122, 2000. ISSN 00189383. doi: 10.1109/16.877173.

[114] M. Bigas, E. Cabruja, J. Forest, and J. Salvi. Review of CMOS image sensors. *Microelectronics Journal*, 37(5):433–451, 2006. ISSN 00262692. doi: 10.1016/j.mejo.2005.07.002.

[115] Robert H. Nixon, Sabrina E. Kemeny, Craig O. Staller, and Eric R. Fossum. 128 x 128 CMOS photodiode-type active pixel sensor with on-chip timing, control, and signal chain electronics. In Morley M. Blouke, editor, *SPIE*, volume 2415, page 117, 4 1995. doi: 10.1117/12.206529. URL http://proceedings.spiedigitallibrary.org/proceeding.aspx?doi=10.1117/12.206529.

[116] Bryce E. Bayer. Color imaging array, 1976.

[117] Joseph R. Lakowicz. *Principles of Fluorescence Spectroscopy*. Springer US, Boston, MA, 2006. ISBN 978-0-387-31278-1. doi: 10.1007/978-0-387-46312-4. URL http://link.springer.com/10.1007/978-0-387-46312-4.

[118] Antonino Cosentino. Macro Photography for Reflectance Transformation Imaging: A Practical Guide to the Highlights Method. *e-conservation Journal*, pages 71–85, 10 2013. ISSN 21831335. doi: 10.18236/econs1.201310. URL http://www.e-conservation.org/issue-1/20-macro-photography-for-reflectance-transformation-imaging.

[119] Costas Balas, Vassilis Papadakis, Nicolas Papadakis, Antonis Papadakis, Eleftheria Vazgiouraki, and George Themelis. A novel hyper-spectral imaging apparatus for the non-destructive analysis of objects of artistic and historic value. *Journal of Cultural Heritage*, 4:330–337, 1 2003. ISSN 12962074. doi: 10.1016/

S1296-2074(02)01216-5. URL http://linkinghub.elsevier.com/retrieve/pii/S1296207402012165.

[120] Haida Liang. Advances in multispectral and hyperspectral imaging for archaeology and art conservation. *Applied Physics A*, 106(2):309–323, 11 2012. ISSN 0947-8396. doi: 10.1007/s00339-011-6689-1. URL http://link.springer.com/10.1007/s00339-011-6689-1.

[121] Seoul Semiconductor. Technical Data Sheet X42180, 2009.

[122] C-Series Spectromaster. Guida software per Utility C-700 / C-7000 Series .

[123] Cree. XLamp XHP50 LEDs Technical data sheet, 2016.

[124] AA. VV. *Scientific Examination of Art: Modern Techniques in Conservation and Analysis*. National Academies Press, Washington, D.C., 8 2005. ISBN 978-0-309-09625-6. doi: 10.17226/11413. URL http://www.nap.edu/catalog/11413.

[125] E. Springer, J. Almog, A. Frank, Z. Ziv, P. Bergman, and W. Gui Qiang. Detection of dry body fluids by inherent short wavelength UV luminescence: preliminary results. *Forensic Science International*, 66(2):89–94, 1994. ISSN 03790738. doi: 10.1016/0379-0738(94)90332-8.

[126] F S Frey, J Warda, American Institute for Conservation of Historic, and Artistic Works. Digital Photographic Documentation Task Force. *The AIC Guide to Digital Photography and Conservation Documentation*. American Institute for Conservation of Historic and Artistic Works, 2011. ISBN 9780976050131. URL https://books.google.ch/books?id=iro6uQAACAAJ.

[127] Elizabeth Allen and Sophie Triantaphillidou. The Manual of Photography (Tenth Edition). In *The Manual of Photography*. Elsevier, 2011. ISBN 9780240520377. doi: 10.1016/B978-0-240-52037-7.10030-4. URL http://linkinghub.elsevier.com/retrieve/pii/B9780240520377100304.

[128] J a Stephen Viggiano. Comparison of the accuracy of different white-balancing options as quantified by their color constancy. *Proceedings of the SPIE*, 5301:323–333, 2004. ISSN 0277786X. doi: 10.1117/12.524922. URL http://proceedings.spiedigitallibrary.org/proceeding.aspx?articleid=1321301.

[129] Lindsay W. MacDonald, Ali Hosseininaveh Ahmadabadian, and Stuart Robson. Determining the coordinates of lamps in an illumination dome. In Fabio Remondino and Mark R. Shortis, editors, *Proceedings of SPIE - The International Society for Optical Engineering*, volume 9528, page 95280I, 6 2015.

doi: 10.1117/12.2185006. URL http://proceedings.spiedigitallibrary.org/proceeding.aspx?doi=10.1117/12.2185006.

[130] Lindsay William Macdonald. *Realistic Visualisation of Cultural Heritage Objects*. PhD thesis, University College London, 2015.

[131] CHI. Rti builder. URL http://culturalheritageimaging.org/WhatWeOffer/Downloads/Process/. accessed: 4-2017.

[132] Massachusetts: The MathWorks Inc Natick. Matlab version 8.5.1.

[133] Swig. URL http://www.swig.org/. accessed: 4-2017.

[134] International Image Interoperability Framework. Api specifications - international image interoperability framework. URL http://iiif.io/api/.

[135] A Bianco, A; Kaiser. rti.js. URL https://github.com/dhlab-basel/rti.js. accessed: 4-2017.

[136] Charles L. Lawson and Richard J. Hanson. *Solving Least Squares Problems*. Society for Industrial and Applied Mathematics, 1 1995. ISBN 978-0-89871-356-5. doi: 10.1137/1.9781611971217. URL http://epubs.siam.org/doi/book/10.1137/1.9781611971217.

[137] Gaël Guennebaud, Benoît Jacob, et al. Eigen v3. http://eigen.tuxfamily.org, 2010.

[138] Alan Kaylor Cline and Inderjit S. Dhillon. Computation of the Singular Value Decomposition. *Handbook of Linear Algebra*, pages 1–14, 2006. ISSN 0010-485X. doi: 10.1007/BF02251248.

[139] Peter J. Rousseeuw and Bert C. van Zomeren. Unmasking Multivariate Outliers and Leverage Points. *Journal of the American Statistical Association*, 85(411): 633, 9 1990. ISSN 01621459. doi: 10.2307/2289995. URL http://www.jstor.org/stable/2289995?origin=crossref.

[140] Peter J. Rousseeuw and Katrien Van Driessen. Computing LTS regression for large data sets. *Data Mining and Knowledge Discovery*, 12(1):29–45, 2006. ISSN 13845810. doi: 10.1007/s10618-005-0024-4.

[141] Peter Fornaro, Andrea Bianco, Aeneas Kaiser, and Lukas Rosenthaler. Enhanced RTI for gloss reproduction. *Electronic Imaging*, 2017(8):66–72, 2017.

[142] Gianpaolo Palma, Monica Baldassarri, Maria Chiara Favilla, and Roberto Scopigno. Storytelling of a Coin Collection by Means of RTI Images: the Case of the Simoneschi Collection in Palazzo Blu. In N Proctor Cherry and R, editors,

Museums and the Web 2014. Silver Spring, 2014. URL http://vcg.isti.cnr.it/Publications/2014/PBFS14.

[143] Manuscripts of lichfield cathedra - the st chad gospels. URL https://lichfield.as.uky.edu/st-chad-gospels/rti.

[144] DHLab. Knowledge organization, representation, and annotation, . URL http://www.knora.org/.

[145] DHLab. System for annotation and linkage of sources in arts and humanities, . URL http://www.salsah.org/.

[146] Phillip Marlow, Juno Kim, and Barton L Anderson. The role of brightness and orientation congruence in the perception of surface gloss. *Journal of vision*, 11(9): 1–12, 2011. ISSN 1534-7362. doi: 10.1167/11.9.16.

[147] Zhou Wang and Alan C Bovik. Mean Squared Error : Love It or Leave It ? *IEEE Signal Processing Magazine*, 26(January):98–117, 2009. ISSN 1053-5888. doi: 10.1109/MSP.2008.930649. URL http://ieeexplore.ieee.org/lpdocs/epic03/wrapper.htm?arnumber=4775883.

[148] Robert J. Woodham. Analysing images of curved surfaces. *Artificial Intelligence*, 17(1-3):117–140, 1981. ISSN 00043702. doi: 10.1016/0004-3702(81)90022-9.

[149] Robert J. Woodham. Gradient and curvature from the photometric-stereo method, including local confidence estimation. *Journal of the Optical Society of America A*, 11(11):3050, 1994. ISSN 1084-7529. doi: 10.1364/JOSAA.11.003050.

[150] K Ikeuchi. Determining surface orientations of specular surfaces by using the photometric stereo method. *IEEE transactions on pattern analysis and machine intelligence*, 3(6):661–669, 1981. ISSN 0162-8828. doi: 10.1109/TPAMI.1981.4767167.

[151] DHLab. Simple image presentation interface, . URL https://github.com/dhlab-basel/Sipi.

ANDREA BIANCO

PERSONAL INFORMATION

Email biancoand@gmail.com

Nationality Italian

Year of birth 1986

EDUCATION

Sep 2014-Oct 2017 Experimental physics

PhD
Digital Humanities Lab, Universität Basel, Basel.
Thesis (English): Characterization and visualization of reflective proprieties of surfaces.
Supervisors: Dr. P. Fornaro & Prof. E. Meyer; Co-referee: Prof. M. Poggio

Sep 2009-Mar 2012 Experimental nuclear and subnuclear physics

Master
110 cum laude · Università degli studi di Trieste, Trieste.
Thesis (English): The energy spectrum of galactic cosmic-ray positrons with the PAMELA experiment
Supervisors: Dr. E. Mocchiutti & Dr. M. Boezio & Prof. A. Gregorio; Co-referee: Prof. G. Della Ricca

Sep 2005-May 2009 Physics

Bachelor
Università degli studi di Trieste, Trieste.
Thesis (Italian): Coulomb potential calculation methods in periodic systems. Supervisor: Prof. G. Pastore

WORK EXPERIENCE

Sep 2017– Current R&D Software Engineer, Truvis, Basel

Truvis
Algorithms development, data acquisition and control, back-end

Sep 2012–Aug 2014 R&D Engineer, Ergolines Lab S.R.L, Trieste

Ergolines Lab R&D
Software developer and tester - Measuring instruments for iron and steel industries.
Algorithms development, data acquisition and control, simulations

Aug 2011–June 2012 Msc student and associate, INFN, Trieste

INFN
Data analysis in the WIZARD/PAMELA group.

Languages
Italian · English · German

Druring the PhD studies I attended the following conferences (contributions between brackets)

- Science and Engineering in Arts, Heritage and Archeology (SEAHA): 2015 (poster), 2016 (presentation);
- IS&T Archiving Conference 2016, (presentation);
- IS&T International Symposium on Electronic Imaging 2017, Material appearance (presentation);
- Digital Humanities 2016, (2 presentations);
- IS&T 23rd Color and Imaging Conference 2015 (CIC23);

Patent application:

[1] Andrea Bianco, Peter Fornaro; Computer System and Method for Improved Gloss Representation in Digital Images; PCT/EP2016/067045; 18. Juli 2017;

Publications in journals and conference proceedings

[1] Peter Fornaro, Andrea Bianco, Aeneas Kaiser, and Lukas Rosenthaler. Enhanced rti for gloss reproduction. *Electronic Imaging*, 2017(8):66–72, 2017.

[2] Lukas Rosenthaler, Peter Fornaro, Andrea Bianco, and Benjamin Geer. Simple image presentation interface (sipi)–an iiif-based image-server. In *Archiving Conference*, volume 2017, pages 28–33. Society for Imaging Science and Technology, 2017.

[3] Peter Fornaro, Andrea Bianco, Heidrun Feldmann, Barbara Schellewald, and Lothar Schmitt. Neue computerbasierte verfahren zur wiedergabe von kunstwerken. *Rundbrief fotografie*, 23(1):14–23, 2016.

[4] Peter Fornaro, Andrea Bianco, and Lukas Rosenthaler. Digital materiality with enhanced reflectance transformation imaging. In *Proceedings of IS&T Archiving Conference (ARCHIVING 2016)*. Society for Imaging Science and Technology, 2016.

[5] Peter Fornaro, Lothar Schmitt, Andrea Bianco, and Heidrun Feldmann. Die digitale modellierung experimenteller druckgrafiken des 15. jahrhunderts. anforderungen und chancen computerbasierter dokumentationsverfahren. In *Digital Humanities 2016: Conference Abstracts*, pages 192–193. Jagiellonian University & Pedagogical University, Kraków, 2016.

[6] A Geissler, Peter Fornaro, and Andrea Bianco. Visual design of pv-modules – a crucial factor for façade application acceptance. In *32nd European Photovoltaic Solar Energy Conference and Exhibition*, pages 2465–2470, 2016.

[7] Federica Mantovani, Stefano Spagnul, Mitja Padovan, and Andrea Bianco. Latest enhancements in mold powder thickness control as a result of a new propulsion system implemented in flux feeding. In *2014 AISTech Conference Proceedings*, number PR-366-167, 2014.

[8] Federica Mantovani, Stefano Spagnul, Mitja Padovan, and Andrea Bianco. Latest enhancements in mold powder thickness control as a result of a new propulsion system implemented in flux feeding. In *8th European Continuous Casting Conference*, 2014.

[9] O Adriani, GC Barbarino, GA Bazilevskaya, R Bellotti, A Bianco, M Boezio, EA Bogomolov, M Bongi, V Bonvicini, S Bottai, et al. Cosmic-ray positron energy spectrum measured by pamela. *Physical review letters*, 111(8):081102, 2013.

[10] O Adriani, GC Barbarino, GA Bazilevskaya, R Bellotti, A Bianco, M Boezio, EA Bogomolov, M Bongi, V Bonvicini, S Bottai, et al. Cosmic-ray positron identification with the pamela experiment. *arXiv preprint arXiv:1306.2198*, 2013.

[11] D Campana, U Giaccari, O Adriani, GC Barbarino, GA Bazilevskaya, R Bellotti, A Bianco, M Boezio, EA Bogomolov, L Bonechi, et al. Search for cosmic ray electron-positron anisotropies with the pamela data. In *Journal of Physics: Conference Series*, volume 409, page 012055. IOP Publishing, 2013.

[12] R Carbone, O Adriani, GC Barbarino, GA Bazilevskaya, R Bellotti, A Bianco, M Boezio, EA Bogomolov, L Bonechi, M Bongi, et al. The pamela experiment: light-nuclei selection with stand-alone detectors. In *Journal of Physics: Conference Series*, volume 409, page 012038. IOP Publishing, 2013.

[13] U Giaccari, O Adriani, GC Barbarino, GA Bazilevskaya, R Bellotti, A Bianco, M Boezio, EA Bogomolov, L Bonechi, M Bongi, et al. Anisotropy studies in the cosmic ray proton flux with the pamela experiment. *Nuclear Physics B-Proceedings Supplements*, 239:123–128, 2013.

[14] E Mocchiutti, O Adriani, GC Barbarino, GA Bazilevskaya, R Bellotti, A Bianco, M Boezio, EA Bogomolov, M Bongi, V Bonvicini, et al. Cosmic–ray positron energy spectrum measured by pamela. In *33RD INTERNATIONAL COSMIC RAY CONFERENCE, RIO DE JANEIRO 2013 THE ASTROPARTICLE PHYSICS CONFERENCE*, 2013.

[15] Roberto Bellotti, Emiliano Mocchiutti, Andrea Bianco, Laura Rossetto, and Alfonso Monaco. The cosmic-ray positron and electron spectra measured by pamela. In *39th COSPAR Scientific Assembly*, volume 39, page 134, 2012.